Adaptive Identification and Control for Underwater Vehicles: Theory and Comparative Experimental Evaluations

by

Christopher J. McFarland

A dissertation submitted to The Johns Hopkins University in conformity with the requirements for the degree of Doctor of Philosophy.

Baltimore, Maryland

November, 2013

Abstract

This Thesis reports several novel algorithms for state observation, parameter identification, and control of second-order plants. A stability proof for each novel result is included. The primary contributions are adaptive algorithms for underwater vehicle (UV) plant parameter identification and model-based control. Where possible, comparative experimental evaluations of the novel UV algorithms were conducted using the Johns Hopkins University Hydrodynamic Test Facility.

The UV adaptive identification (AID) algorithms reported herein estimate the plant parameters (hydrodynamic mass, quadratic drag, gravitational force, and buoyancy parameters) of second-order rigid-body UV plants under the influence of actuator forces and torques. Previous adaptive parameter identification methods have focused on model-based adaptive tracking controllers; however, these approaches are not applicable when the plant is either uncontrolled, under open-loop control, or using any control law other than a specific adaptive tracking controller. The UV AID algorithms reported herein do not require simultaneous reference trajectory-tracking control, nor do they require instrumentation of linear acceleration or angular acceleration. Thus, these results are applicable in the com-

monly occurring cases of uncontrolled vehicles, vehicles under open-loop control, vehicles using control methods prescribed to meet other application-specific considerations, and vehicles not instrumented to measure angular acceleration. In comparative experimental evaluations, adaptively identified plant models (AIDPMs) were shown to accurately model experimentally measured UV performance.

The UV model-based control (MBC) and adaptive model-based control (AMBC) algorithms reported herein provide asymptotically exact trajectory-tracking for fully coupled second-order rigid-body UV plants. In addition, the AMBC algorithm estimates the plant parameters (hydrodynamic mass, quadratic drag, gravitational force, and buoyancy parameters) for this class of plants. A two-step AMBC algorithm is also reported which first identifies gravitational plant parameters to be used in a separate AMBC algorithm for trajectory-tracking. We report a comparative experimental analysis of proportional derivative control (PDC) and AMBC during simultaneous motion in all degrees-of-freedom. This analysis shows:

- AMBC (i.e. simultaneous adaptation of all plant parameter estimates) can be unstable in the presence of unmodeled thruster dynamics
- two-step AMBC is robust to the presence of unmodeled thruster dynamics, and
- two-step AMBC provides 30% better position tracking performance and 8% worse velocity tracking performance over PDC.

To the best of our knowledge, the reported comparative experimental evaluation of AMBC

and PDC is the first to consider trajectory-tracking performance during simultaneous motion in all degrees-of-freedom.

Thesis Adviser: Dr. Louis L. Whitcomb, Professor, Johns Hopkins University

Thesis Committee:

Dr. Noah J. Cowan, Associate Professor, Johns Hopkins University

Dr. Dana Yoerger, Senior Scientist, Woods Hole Oceanographic Institution

Dr. Marin Kobilarov, Assistant Professor, Johns Hopkins University

Dr. Louis L. Whitcomb, Professor, Johns Hopkins University

Acknowledgements

It is a simple truth that I could not have made it this far without others investing in me. My education was supported by the University of Puget Sound through several scholarships; Washington University in St. Louis through a Browns Fellowship for dual degree engineering students; and the Johns Hopkins University Mechanical Engineering Department through a Departmental Fellowship. My education and research were supported by the Department of Defense, Air Force Office of Scientific Research through a National Defense Science and Engineering Graduate Fellowship (32 CFR 168a); the National Science Foundation through awards 812138 and 1319667; the Link Foundation through a Link Doctoral Research Fellowship in Ocean Engineering and Instrumentation; and the ARCS Foundation through their fellowship for science and technology scholars.

This Thesis is dedicated to my teachers, i.e. those who have invested effort in helping me become a better scientist, engineer, and person. Teachers can be professors, friends, family members, colleagues, in addition to the "teachers" who guided my childhood education. I am proud of the contributions contained herein; however, when I look back on all the effort others have invested in me, this work seems inadequate.

ACKNOWLEDGEMENTS

I came to Johns Hopkins University for one reason. I thought Dr. Whitcomb was exactly the type of engineer I wanted to be. Dr. Whitcomb, I was correct in that belief and am grateful you have devoted so much of yourself to helping me become an engineer like you. Over the past decade I have had several mentors who were always ready to discuss new research directions over the phone or in-person. Dr. Yoerger, Dr. Cowan, Dr. Kobilarov, Dr. Sarma, Dr. Smart, Mr. Few, and Mr. Cain, I have enjoyed moments of friendship and scholarship with each of you. Thank you for taking these opportunities to teach me the difficult art of picking what problems are worth attempting to solve (and the many, many letters of recommendation). I am especially grateful for Dr. Yoerger, Dr. Cowan, Dr. Kobilarov, and Dr. Whitcomb taking the time to serve on my Thesis committee and improve the work contained herein.

So many educators have been instrumental in getting me here by immersing me in physics, engineering, and the arts. Dr. Thorndike, Dr. Elliott, Dr. Weber, Dr. Beezer, Dr. Stockdale, Dr. Tarraf, Dr. Fishkind, Dr. Genin, Mr. Calkins, Dr. Jones, Mr. Dyer, Mr. Shen, Mrs. Holmes, Mr. Sweeney, Mr. Palma, Mr. Johnson, Mrs. Johnson, Mrs. Barnett, Mrs. Brown, and those I have forgotten to mention, words can not express how grateful I am for the countless hours spent helping me better understand the world.

Over the past 6 years I have been surrounded by so many fantastic colleagues. Steve, Kevin, Mike, Tricia, John, Axel, Tom, Carol, Netta, David, Tiffany, Hunter, Tomo, Kirk, Claire, Adrien, Manu, Kel, Xingchi, Yixin, and Zak, thanks for always being willing to teach me something new, just talk about research, or have a fun night out. During these

years an amazing group of close friends have poured themselves into helping me become who I am today. Drew, Grant, Karrie, Pat, Marisa, Lauren, Giancarlo, Amy, Sarah, Marcin, Eatai, Maya, Jon, Chad, Jowita, and Yan Yan each of you deserve a paragraph inserted here. In its stead, let me offer a heartfelt (if inadequate) thank you for your love and support.

In closing, I would like to acknowledge my parents, the most important teachers I have ever had. I am so grateful for your enduring education in how to lead a happy, successful life. Thank you.

Dedication

to my teachers

Contents

List of Tables

List of Figures

List of Acronyms

AID adaptive identification

AIDP adaptively identified parameter set

AIDPM adaptively identified plant model

AMBC adaptive model-based control

AUV autonomus underwater vehicle

COG center-of-gravity

COB center-of-buoyancy

CROSS experiment for cross-validation

DOF degree-of-freedom

DVL Doppler velocity log

IDDAT experiment for parameter identification

INITP initialization parameter set

INITPM initialization parameter set plant model

INS inertial navigation system

JHU ROV Johns Hopkins University Remotely Controlled Vehicle

LS least squares identification

LSP least squares identified parameter set

LSPM least squares identified plant model

List of Acronyms

MAE mean absolute error

MBC model-based control

MNE mean normal of error vectors

OKC open kinematic chain

PDC proportional derivative control

PDS positive definite symmetric

PROV Polar Remotely Operated Vehicle

ROV remotely operated vehicle

SMS simple mechanical system

UV underwater vehicle

Chapter 1

Introduction

1.1 Motivation

Salt water covers over 70 % of the surface of the earth. The world's oceans and seas to exert a huge influence on global weather patterns, cover the longest mountain range in the world, span 98% of the earth's inhabitable volume, and contain several millennia of ship wrecks. Recent advances in underwater vehicle (UV) capabilities have enabled climatologists, geologists, biologists, and archaeologists to consider addressing research topics previously thought impractical or impossible (see Figure 1.1 for examples). The goal of this Thesis is to enable better utilization of these capabilities through the development of novel algorithms for state estimation, parameter identification, and control. To this end, each type of algorithm presented herein has its own motivating applications:

- **State Estimation:** New state estimation algorithms have the potential to improve

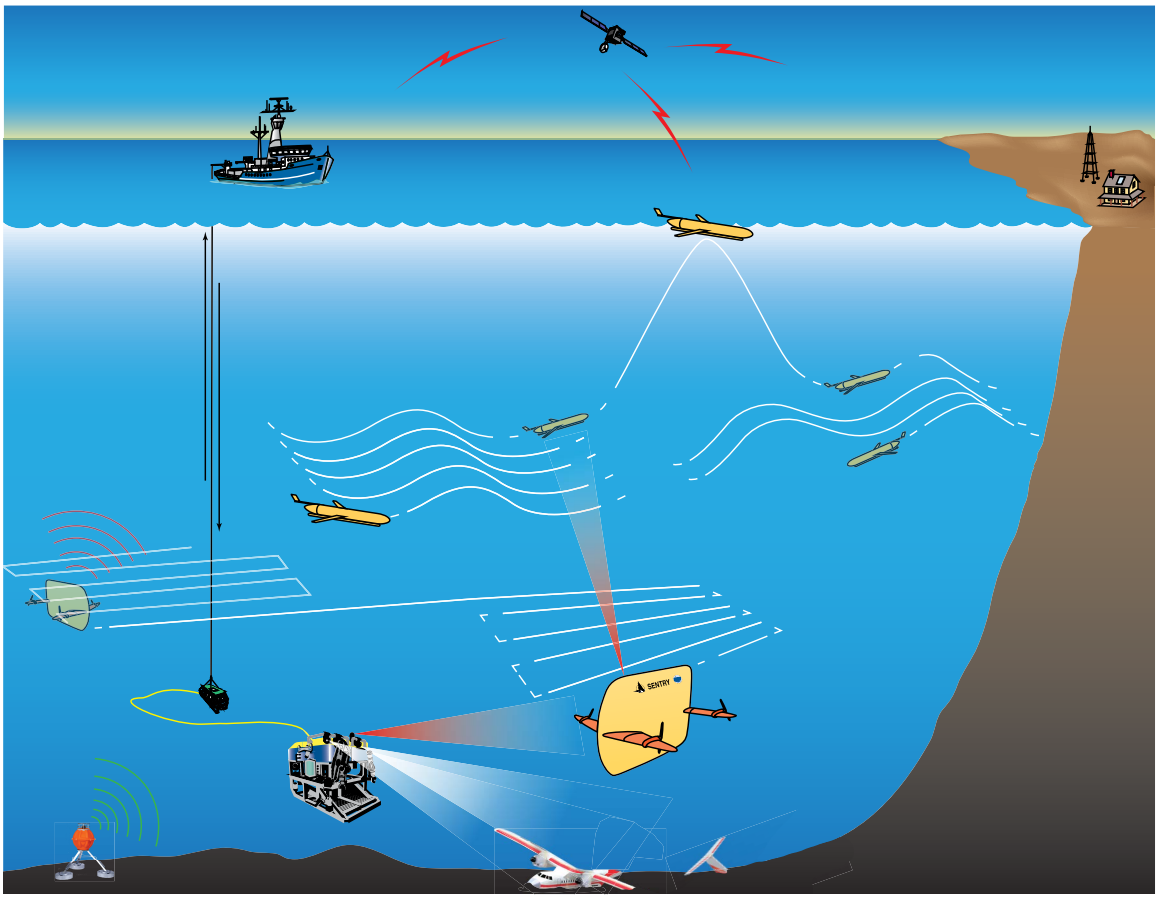

Figure 1.1: Recent advances in underwater vehicle (UV) systems have enabled scientists and engineers to consider complex, multifaceted UV missions previously thought impractical or impossible. These new missions include UV teams for environmental monitoring, such as the team of 5 gliders shown; ship-based or on-shore operator monitoring and re-tasking of UVs, such as the re-tasking of the AUV Sentry shown; and deployment of UVs in delicate or dynamic environments, such as the ROV Jason operating near the plane wreck shown. *Improved state estimation* algorithms can increase navigation accuracy and lower the cost of UV teams. *Improved parameter identification* algorithms enable remote operators to remotely diagnose failures and use forward simulation for in-situ mission replanning for UVs similar to Sentry. *Improved control* algorithms enable increased precision of delicate or dynamic 6-DOF operation for ROVs such as Jason. Image credit: Paul Oberlander, WHOI.

UV navigation for a wide range of applications. UVs operate in an environment with available sensing modalities different from terrestrial, aerial, and on-orbit systems. One consequence of these UV specific conditions is a reliance on dead-reckoning algorithms for translational position estimates during 6-dimensional maneuvers. It is plausible that state estimation algorithms which leverage the group structure rigid-body motion can increase navigation accuracy during UV operation. Such state estimation algorithms have the potential to enable UV navigation with different sensor suites than currently required.

- **Parameter Identification:** Knowledge of UV plant parameters enable utilization of forward simulation and other model-based algorithms for a wide range of oceanographic research deployments. The most commonly employed plant models for underwater vehicles are finite dimensional lumped-parameter approximate models with vehicle-specific plant parameter terms including mass and added mass parameters; quadratic drag parameters; and gravity and buoyancy parameters. For real-world vehicles it is impossible to compute these plant parameters analytically, thus the plant parameters must be identified experimentally. Most previous studies of non-adaptive plant parameter identification employ off-line conventional least-square methods requiring instrumentation of the vehicle attitude; linear and angular velocity; linear and angular acceleration; and applied force and moment. Since UVs are often not instrumented to measure angular acceleration, adaptive methods may provide model parameter estimates that could not be obtained by other standard methods, such as

conventional least squares. Previous adaptive parameter identification methods have focused on model-based adaptive tracking controllers; however these approaches are not applicable when the plant is either uncontrolled, under open-loop control, or using any control law other than a specific adaptive tracking controller. Such conditions frequently occur on oceanographic research UV. With commercially available vehicles, often the user can not replace the controller provided by the vehicle's manufacturer with an adaptive tracking control algorithm. Vehicle designers frequently utilize UV passive stability of pitch and roll in the design of under-actuated vehicles. Adaptive tracking controllers assume actuation in all degrees-of-freedom, making adaptive tracking control inapplicable for either control or model identification of under-actuated vehicles. Adaptive identification algorithms do not require simultaneous reference trajectory-tracking control, nor do they require instrumentation of linear acceleration or angular acceleration.

- **Trajectory-Tracking:** Many of the missions recently enabled by advances in UV technology, such as seafloor surveying and environmental monitoring, depend on tracking a specified trajectory as closely as possible. To facilitate these missions, novel UV control algorithms are required to provide improved trajectory-tracking precision. Previous studies have shown experimentally that model-based control can provide significant performance gains over proportional derivative control [45, 65]. For most UVs the drag parameters and mass parameters (which include both the characteristics of the vehicle's mass and those of the ambient fluid surrounding the

vehicle) can not be computed analytically. Adaptive model-based control removes the need for *a-priori* parameter estimates and could enable accurate long duration trajectory tracking through continuous model retuning.

1.2 Thesis Outline

The main contributions of this Thesis are presented in Chapters 3, 4, and 5. A stability analysis for each novel result is included.

Chapter 2 - Modeling Second-Order Mechanical Systems: This Chapter defines the notation, functions, state representations, and second-order plant models used in this Thesis.

Chapter 3 - State Estimation and Parameter Identification for Simple Mechanical Systems (SMS): The standard models for UV dynamic operation evolve on the set of rigid-body transformations, SE(3). Thus, the first third of this Thesis is focused on utilizing the group structure of SO(3) and SE(3) in the development of one state observer and two adaptive identification (AID) algorithms for simple mechanical system (SMS). These results are the theoretical antecedents of the UV results reported in Chapters 4 and 5. The plant of the angular velocity observer is a 3-degree-of-freedom (DOF) second-order rigid-body rotating under the influence of an externally applied torque. Numerical simulations of the novel angular velocity observer and two previously reported observers are included. The simulation results show similar performance of all three observers for most angular position trajectories and inertia tensors. A novel AID algorithm is reported for a 3-DOF

second-order rigid body rotating under the influence of an externally applied torque, along with a simulation study. An AID algorithm for open kinematic chains (OKCs) is also reported.

Chapter 4 - Adaptive Identification (AID) for Underwater Vehicles (UV): The UV AID algorithms reported herein estimate the plant parameters for hydrodynamic mass, quadratic drag, gravitational force, and buoyancy for a second-order rigid-body plant under the influence of actuator forces and torques. An experimental comparison of AID and conventional least squares identification (LS) is reported. The experimental results corroborate the analytic stability analysis, showing that the adaptively estimated plant parameters are stable and converge to values that provide plant-model input-output behavior closely approximating the input-output behavior of the actual experimental UV. The adaptively identified plant models (AIDPMs) are shown to be similar to the least squares identified plant models (LSPMs) in their ability to match the actual vehicle's input-output characteristics.

Chapter 5 - Adaptive Model-Based Control For Underwater Vehicles : This Chapter reports two tracking controllers: a UV model-based control (MBC) algorithm which provides asymptotically exact trajectory-tracking, and a novel UV adaptive model-based control (AMBC) algorithm which provides asymptotically exact trajectory-tracking while estimating the parameters for hydrodynamic mass, quadratic drag, gravitational force, and buoyancy parameters for a fully-coupled second-order rigid-body UV plant model.

A comparative experimental evaluation of proportional derivative control (PDC) and AMBC for UVs is reported. To the best of the author's knowledge, this is the first such

evaluation of model-based adaptive tracking control for underwater vehicles during simultaneous dynamic motion in all 6-DOF. This experimental evaluation revealed the presence of unmodeled thruster dynamics arising during reversals of the vehicle's thrusters, and that the unmodeled thruster dynamics can destabilize parameter adaptation. The three major contributions of this experimental evaluation are: an experimental analysis of how unmodeled thruster dynamics can destabilize parameter adaptation, a two-step adaptive model-based control algorithm which is robust to the thruster modeling errors present, and a comparative experimental evaluation of AMBC and PDC for fully-actuated underwater vehicles preforming simultaneous 6-DOF trajectory-tracking.

Chapter 6 - Conclusion: Thesis results summarized and directions for future work presented.

Appendix A - Johns Hopkins University Hydrodynamic Test Facility: The details of the Johns Hopkins University Hydrodynamic Test Facility and our experimental testing methodologies are presented. This facility includes the Johns Hopkins University Remotely Controlled Vehicle (JHU ROV), a fully actuated UV used for the experimental trials reported in Chapters 4 and 5.

Appendix B - Special Euclidean Group Velocity Jacobian: Details of the SE(3) Velocity Jacobian are reported. These results are required for the UV MBC stability proof (Theorem 5.2.1).

Chapter 2

Modeling Second-Order Rigid-Body Mechanical Systems

This Chapter summarizes the notation, kinematic conventions, and plant models used in this Thesis. With the exception of Section 2.3, the models, functions, state spaces, and facts stated herein are commonly employed in the fields of geometric control, adaptive control, and underwater robotics. Section 2.2 states the functions, norms, and positive definite symmetric (PDS) matrix eigenvalue conventions used herein. Section 2.3 reports a proof of Theorem 2.3.2, which allows general 3-by-3 matrices to be factored through the skew symmetric operator. Sections 2.4.1 and 2.4.2 detail the position and velocity state representations used herein for a rotating rigid-body and general rigid-body motion. The analytic relationships between these state representations are also stated. This Chapter presents second-order models for:

- 3-degree-of-freedom (DOF) rotating rigid-body dynamics (Section 2.5.1),
- 3-DOF rotating underwater vehicle (UV) dynamics (Section 2.5.2),
- 6-DOF UV dynamics (Section 2.6), and
- *n*-link open kinematic chain (OKC) dynamics (Section 2.7).

For each of the four models, plant parameter properties and the model's regressor matrix factored form are also presented. Readers seeking a presentation of this material in greater detail are referred to the texts cited in Section 2.1.

As noted in the summery above, we believe Theorem 2.3.2 is a novel result. This Theorem states that $A^T((Ax) \times (Ay)) = \det(A)(x \times y)$ for all $A \in \mathbb{R}^{3\times 3}$ and $x, y \in \mathbb{R}^3$, where $\times$ is the usual cross product operator for $\mathbb{R}^3$ and $\det(\,\cdot\,)$ is the matrix determinate. This result is a generalization of the well known fact $(Rx) \times y = R(x \times (Ry))$ for all $x, y \in \mathbb{R}^3$ and $R \in \mathrm{SO}(3)$, where SO(3) is the special orthogonal group for $\mathbb{R}^(3)$. To the best of our knowledge, this relation has not been proposed or proven previously.

2.1 Background Literature

The foundation of this Thesis is a set of good ideas and facts cherry picked from the long history of research into modeling rigid-body dynamics. Those ideas and facts are summarized in this Chapter. Readers requiring more information are referred to the following texts for the reasons listed. Taylor's *Classical Mechanics* [67] provides an excellent intro-

duction to modeling rigid-body motion using non-inertial reference frames. In [12], Bullo and Lewis provide both a rigorous development of and a compelling case for utilizing differential geometry techniques in nonlinear control theory. Chapters 5, 6, and 7 from [16], by Chirikjian and Kyatkin, and [50], by Murray, Li and Sastry, elucidate the representation of rigid-body motion in the groups SO(3) and SE(3). *A Short Introduction to Applications of Quaternions*, by A. G. Rawlings [56], presents different coordinate systems used to represent rigid-body rotations. Rawlings's text also presents the intuition behind the individual coordinate systems and the interconnections between those representations. *Guidance and Control of Ocean Vehicles* by Fossen [18] and *Advances in Six-Degree-of-Freedom Dynamics and Control of Underwater Vehicles* by Martin [44] present the details of modeling underwater vehicle (UV) dynamics.

2.2 Notation Conventions

We assume the readers are familiar with SO(3), the special orthogonal group for $\mathbb{R}^3$, and SE(3), the special euclidean group for $\mathbb{R}^3$. We also assume readers are familiar with their tangent spaces so(3) and se(3) respectively. Readers not familiar with these concepts are referred to [50].

2.2.1 Function Definitions

Functions used throughout this text are defined as follows:

- $\mathcal{J} : \mathbb{R}^3 \to \mathbb{R}^{3\times 3}$ is the mapping from $\mathbb{R}^3$ to so(3), the tangent space of SO(3), and is defined by

$$\mathcal{J}\left(\begin{bmatrix} \omega_1 \\ \omega_2 \\ \omega_3 \end{bmatrix}\right) = \begin{bmatrix} 0 & -\omega_3 & \omega_2 \\ \omega_3 & 0 & -\omega_1 \\ -\omega_2 & \omega_1 & 0 \end{bmatrix}. \tag{2.1}$$

- $\widehat{\cdot} : \mathbb{R}^6 \to \mathbb{R}^{4\times 4}$ is the mapping from $\mathbb{R}^6$ to se(3), the tangent space of SE(3), and (for $\nu, \omega \in \mathbb{R}^3$) is defined by

$$\widehat{\begin{bmatrix} \nu \\ \omega \end{bmatrix}} = \begin{bmatrix} \mathcal{J}(\omega) & \nu \\ 0_{1\times 3} & 0 \end{bmatrix}. \tag{2.2}$$

- $\mathrm{ad} : \mathbb{R}^6 \to \mathbb{R}^{6\times 6}$ is the se(3) adjoint operator. For the vector

$$v = \begin{bmatrix} \nu \\ \omega \end{bmatrix} \tag{2.3}$$

the se(3) adjoint operator is defined as

$$\mathrm{ad}_v = \begin{bmatrix} \mathcal{J}(\omega) & \mathcal{J}(\nu) \\ 0_{3\times 3} & \mathcal{J}(\omega) \end{bmatrix}. \tag{2.4}$$

- $\mathrm{Ad} : \mathrm{SE}(3) \to \mathbb{R}^{6\times 6}$ is the se(3) adjoint map, defined as

$$\mathrm{Ad}\left(\begin{bmatrix} R & p \\ 0_{1\times 3} & 1 \end{bmatrix}\right) = \begin{bmatrix} R & \mathcal{J}(p)R \\ 0_{3\times 3} & R \end{bmatrix}. \tag{2.5}$$

- $\otimes : \mathbb{R}^{m\times n} \times \mathbb{R}^{p\times q} \to \mathbb{R}^{(m*p)\times(n*q)}$ is the Kronecker product operator [21]. For

matrices

$$A = \begin{bmatrix} a_{11} & a_{12} & \dots & a_{1n} \\ a_{21} & a_{22} & & a_{2n} \\ \vdots & & \ddots & \vdots \\ a_{m1} & a_{m2} & \dots & a_{mn} \end{bmatrix} \text{ and } B = \begin{bmatrix} b_{11} & b_{12} & \dots & b_{1q} \\ b_{21} & b_{22} & & b_{2q} \\ \vdots & & \ddots & \vdots \\ b_{p1} & b_{p2} & \dots & b_{pq} \end{bmatrix} \tag{2.6}$$

the Kronecker product is defined as

$$A \otimes B = \begin{bmatrix} a_{11}B & a_{12}B & \dots & a_{1n}B \\ a_{21}B & a_{22}B & & a_{2n}B \\ \vdots & & \ddots & \vdots \\ a_{m1}B & a_{m2}B & \dots & a_{mn}B \end{bmatrix}. \tag{2.7}$$

- $\cdot^S : \mathbb{R}^{m \times n} \to \mathbb{R}^{(m*n)}$ is the stack operator. Using the definition of A above, the stack operator is defined by stacking the columns of A such that

$$A^S = \begin{bmatrix} a_{11} & a_{21} & \cdots & a_{m1} & a_{12} & a_{22} & \cdots & a_{m2} & \cdots & a_{1n} & a_{2n} & \cdots & a_{mn} \end{bmatrix}^T. \tag{2.8}$$

This Thesis will also make use of

- the SO(3) exponential map, $\mathrm{e}_{\mathrm{SO(3)}} : \mathrm{so}(3) \to \mathrm{SO}(3)$
- the SO(3) logarithmic map, $\log_{SO3} : \mathrm{SO}(3) \to \mathrm{so}(3)$
- the SE(3) exponential map, $\mathrm{e}_{\mathrm{SE(3)}} : \mathrm{se}(3) \to \mathrm{SE}(3)$
- the SE(3) logarithmic map, $\log_{SE3} : \mathrm{SE}(3) \to \mathrm{se}(3)$

See [50] for additional information, including closed form functions, for these maps.

2.2.2 Vector Norm, Matrix Norm, and Eigenvalue Conventions

Let $M \in \mathbb{R}^{n\times n}$ represent a PDS inertia tensor or hydrodynamic mass matrix. Note that the eigenvalues of symmetric matrices are always real. This Thesis employs the following conventions for the eigenvalues of such matrices: m_n is the smallest and m_1 is the largest eigenvalues of the mass matrix, the other eigenvalues are labeled such that $m_{i-1} \leq m_i \leq m_{i+1}$ $\forall i$ such that $2 \leq i \leq n-1$. This convention will also be used for any mass matrix estimate or mass matrix error term, i.e. if $\hat{M}(t)$ is an estimate of a true mass matrix M and $\Delta M(t) = \hat{M}(t) - M$ then these eigenvalues will be ordered such that $\hat{m}_{i-1}(t) \leq \hat{m}_i(t) \leq \hat{m}_{i+1}(t)$ and $\Delta m_{i-1}(t) \leq \Delta m_i(t) \leq \Delta m_{i+1}(t)$. We assume that the eigenvalues of physically realistic mass matrices are either constant or bounded for all time, i.e. there exists a scalar $a \in \mathbb{R}_+$ such that $m_1 < a$.

The $\ell 2$ norm, or Euclidean norm, for $x \in \mathbb{R}^n$ is defined as $\|x\| = (\sum_{i=1}^n x_i^2)^{1/2}$. The $\ell 2$ induced matrix norm, also known as the spectral norm, for $M \in \mathbb{R}^{n\times n}$ is defined as $\|M\|_2 = \max_{\|x\|=1} \|Mx\|$. Let a_{ij} be the individual entries of $A \in \mathbb{R}^{n\times n}$, the Frobenius norm of A is defined as $\|A\|_F = \left(\sum_{i,j=1}^n |a_{ij}|^2\right)^{1/2}$. For more information on these norms see [23]. We define the following matrix semi-norm

$$\|M\|_{\text{min}} = \min_{\|x\|=1} \|Mx\|. \tag{2.9}$$

For a given mass matrix M, these definitions and the cross product property $\|x_1 \times x_2\| \leq \|x_1\|\|x_2\|$ give rise to the following properties

$$m_n\|x\| = \|M\|_{\min}\|x\| \leq \|Mx\| \leq \|M\|_2\|x\| = m_1\|x\|, \tag{2.10}$$

$$\|-Mx\| \leq -m_n\|x\|, \tag{2.11}$$

$$\|M^{-1/k}\|_2 = \|M^{-1}\|_2^{1/k} = \left(\frac{1}{m_n}\right)^{1/k}, \tag{2.12}$$

$$\|ML\|_2 \leq \|M\|_2\|L\|_2 = m_1 l_1, \text{ and} \tag{2.13}$$

$$\|\mathcal{J}(Mx_1)x_2\| \leq \|Mx_1\|\|x_2\| \leq m_1\|x_1\|\|x_2\|. \tag{2.14}$$

2.3 Matrix Factorization Through the Skew Symmetric Operator

Lemma 2.3.1 *For all real orthogonal matrices $U \in \mathrm{O}(3)$ and $a \in \mathbb{R}^3$ the following equality holds*

$$U\mathcal{J}(x)U^T = \det(U)\mathcal{J}(Ua) \tag{2.15}$$

Proof: Let $x, y, z \in \mathbb{R}^3$ be defined such that $U^T = [x \quad y \quad z]$. The facts $UU^T = \mathbb{I}$ and $x^T\mathcal{J}(y)z = \det(U)$ imply that $\mathcal{J}(y)z = \det(U)x$, $\mathcal{J}(z)x = \det(U)y$, and $\mathcal{J}(x)y =$

$\det(U)z$. Note that $\forall\ \psi_1, \psi_2, a \in \mathbb{R}^3$ we know $\psi_1^T \mathcal{J}(a)\,\psi_2 = a^T \mathcal{J}(\psi_2)\,\psi_1$ and consider

$$
\begin{aligned}
U\mathcal{J}(a)\,U^T =& U \begin{bmatrix} \mathcal{J}(a)\,x & \mathcal{J}(a)\,y & \mathcal{J}(a)\,z \end{bmatrix} \\
=& \begin{bmatrix} x^T\mathcal{J}(a)\,x & x^T\mathcal{J}(a)\,y & x^T\mathcal{J}(a)\,z \\ y^T\mathcal{J}(a)\,x & y^T\mathcal{J}(a)\,y & y^T\mathcal{J}(a)\,z \\ z^T\mathcal{J}(a)\,x & z^T\mathcal{J}(a)\,y & z^T\mathcal{J}(a)\,z \end{bmatrix} \\
=& \begin{bmatrix} 0 & a^T\mathcal{J}(y)\,x & a^T\mathcal{J}(z)\,x \\ a^T\mathcal{J}(x)\,y & 0 & a^T\mathcal{J}(z)\,y \\ a^T\mathcal{J}(x)\,z & a^T\mathcal{J}(y)\,z & 0 \end{bmatrix} \\
=& \mathcal{J}\left(\begin{bmatrix} a^T\mathcal{J}(y)\,z \\ a^T\mathcal{J}(z)\,x \\ a^T\mathcal{J}(x)\,y \end{bmatrix}\right) \\
=& \det(U)\mathcal{J}(Ua)
\end{aligned}
\tag{2.16}
$$

Lemma 2.3.2 *For all diagonal matrices $D \in \mathbb{R}^{3\times 3}$ and $x \in \mathbb{R}^3$ the following equality holds*

$$
D\mathcal{J}(Dx)\,D = \det(D)\mathcal{J}(x) \tag{2.17}
$$

Proof: Let $\lambda_1, \lambda_2, \lambda_3 \in \mathbb{R}$ be the diagonal entries of D and $x_1, x_2, x_3 \in \mathbb{R}$ be the entries of $x \in \mathbb{R}^3$. Note that we have the equality $\det(D) = \lambda_1\lambda_2\lambda_3$, thus

$$
\begin{aligned}
D\mathcal{J}\left(Dx\right)D = & \begin{bmatrix} \lambda_1 & 0 & 0 \\ 0 & \lambda_2 & 0 \\ 0 & 0 & \lambda_3 \end{bmatrix} \begin{bmatrix} 0 & -\lambda_3 x_3 & \lambda_2 x_2 \\ \lambda_3 x_3 & 0 & -\lambda_1 x_1 \\ -\lambda_3 x_2 & \lambda_3 x_1 & 0 \end{bmatrix} \begin{bmatrix} \lambda_1 & 0 & 0 \\ 0 & \lambda_2 & 0 \\ 0 & 0 & \lambda_3 \end{bmatrix} \\
= & \begin{bmatrix} 0 & -\lambda_1\lambda_2\lambda_3 x_3 & \lambda_1\lambda_2\lambda_3 x_2 \\ \lambda_1\lambda_2\lambda_3 x_3 & 0 & -\lambda_1\lambda_2\lambda_3 x_1 \\ -\lambda_1\lambda_2\lambda_3 x_2 & \lambda_1\lambda_2\lambda_3 x_1 & 0 \end{bmatrix} \\
= & \lambda_1\lambda_2\lambda_3 \begin{bmatrix} 0 & -x_3 & x_2 \\ x_3 & 0 & -x_1 \\ -x_2 & x_1 & 0 \end{bmatrix} \\
= & \det(D)\mathcal{J}\left(x\right)
\end{aligned} \tag{2.18}
$$

Theorem 2.3.3 *For all matrices $A \in \mathbb{R}^{3\times 3}$ and $x \in \mathbb{R}^3$ the following equality holds*

$$A^T\mathcal{J}\left(Ax\right)A = \det(A)\mathcal{J}\left(x\right) \tag{2.19}$$

Proof: Consider the following facts

- From Lemma 2.3.2, $U \in \mathrm{O}(3)$, and $x \in \mathbb{R}^3$ we know $\mathcal{J}\left(Ux\right) = \det(U)U\mathcal{J}\left(x\right)U^T$.
- From Lemma 2.17, for all diagonal matrices $\Sigma \in \mathbb{R}^{3\times 3}$, and all $x \in \mathbb{R}^3$ we know $\Sigma^T\mathcal{J}\left(\Sigma\right)\Sigma = \det(\Sigma)\mathcal{J}\left(x\right)$.
- For all $A \in \mathbb{R}^{3\times 3}$ there exists an SVD decomposition for which $A = U\Sigma V^T$ where

$U \in \mathbb{R}^{3\times3}$ and $V \in \mathbb{R}^{3\times3}$ are real orthogonal matrices, and $\Sigma \in \mathbb{R}^{3\times3}$ is a diagonal matrix with the singular values of A along its diagonal.

- $\det(A) = \det(U)\det(\Sigma)\det(V)$.

Thus

$$\begin{aligned} A^T\mathcal{J}(Ax)A &= V\Sigma U^T\mathcal{J}\left(U\Sigma V^T x\right)U\Sigma V^T \\ &= \det(U)V\Sigma U^T U\mathcal{J}\left(\Sigma V^T x\right)U^T U\Sigma V^T \\ &= \det(U)V\Sigma\mathcal{J}\left(\Sigma V^T x\right)\Sigma V^T \\ &= \det(U)\det(\Sigma)V\mathcal{J}\left(V^T x\right)V^T \\ &= \det(U)\det(\Sigma)\det(V)VV^T\mathcal{J}(x)VV^T \\ &= \det(A)\mathcal{J}(x) \end{aligned} \tag{2.20}$$

Corollary 2.3.4 *For all $a, b, c, d \in \mathbb{R}$, $x \in \mathbb{R}^3$, and $I \in \mathbb{R}^{3\times3}$ such that I is PDS, the following equality holds*

$$I^a\mathcal{J}\left(I^b x\right)I^c = \det(I)^d I^{a-d}\mathcal{J}\left(I^{b-d}x\right)I^{c-d}. \tag{2.21}$$

Proof: Let λ_1, λ_2 and λ_3 be the eigenvalues of I, where the λ_i are labeled without regard to ordering for the largest or smallest eigenvalues. Since I is PDS, these eigenvalues are positive and there exists $R \in \mathrm{SO}(3)$ and PDS diagonal matrix $D \in \mathbb{R}^{3\times3}$ such that λ_1, λ_2 and λ_3 are the diagonal terms of D and $I = RDR^T$. Note that for $d \in \mathbb{R}$ we have the equality $\det(I)^d = \det(D)^d = \lambda_1^d\lambda_2^d\lambda_3^d$, from Lemma 2.3.2 we

know $\det(D)^d D^{-d}\mathcal{J}(x)D^{-d} = \mathcal{J}\left(D^d x\right)$ and for all $R \in \mathrm{SO}(3)$ we have the equality $R\mathcal{J}\left(x\right)R^T = \mathcal{J}\left(Rx\right)$. Thus

$$\begin{aligned}
I^a\mathcal{J}\left(I^b x\right)I^c =& RD^aR^T\mathcal{J}\left(RD^bR^Tx\right)RD^cR^T \\
=& RD^a\mathcal{J}\left(D^bR^Tx\right)D^cR^T \\
=& RD^a\mathcal{J}\left(D^dD^{b-d}R^Tx\right)D^cR^T \\
=& RD^a\left(\det\left(D^d\right)D^{-d}\mathcal{J}\left(D^{b-d}R^Tx\right)D^{-d}\right)D^cR^T \\
=& \det\left(I^d\right)RD^{a-d}\mathcal{J}\left(D^{b-d}R^Tx\right)D^{c-d}R^T \\
=& \det\left(I^d\right)RD^{a-d}R^T\mathcal{J}\left(RD^{b-d}R^Tx\right)RD^{c-d}R^T \\
=& \det\left(I^d\right)I^{a-d}\mathcal{J}\left(I^{b-d}x\right)I^{c-d}.
\end{aligned} \tag{2.22}$$

This completes the proof. In the following Chapters Corollary 2.3.4 is not explicitly used, but has been useful in developing Lyapunov functions for second-order rotational plants.

2.4 State Representations

2.4.1 Rotating Rigid-Body Kinematics

We use three state representations of rigid-body angular position and velocity:

- $q \in \mathbb{R}^3$, the angular position in so(3) exponential coordinates,
- $\omega \in \mathbb{R}^3$, the body-frame angular velocity, and
- $R \in \mathrm{SO}(3)$, the rotation matrix from the body-frame to the world-frame.

The relations between these state representations are given by

$$R = e^{\mathcal{J}(q)} \tag{2.23}$$

$$\dot{R} = R\mathcal{J}(\omega). \tag{2.24}$$

Throughout this study we make use of the relation between the body-frame angular velocity, ω, and the time derivative of the exponential coordinate position, $\dot{q}$, which takes the form

$$\omega = \mathcal{A}(q)\dot{q}. \tag{2.25}$$

The closed form for the Jacobian $A : \mathbb{R}^3 \to \mathbb{R}^{3\times 3}$ given by

$$A(q) = I + \left(\frac{1-\cos\|q\|}{\|q\|}\right)\frac{\mathcal{J}(q)}{\|q\|} + \left(1 - \frac{\sin\|q\|}{\|q\|}\right)\frac{\mathcal{J}(q)^2}{\|q\|^2}. \tag{2.26}$$

was first reported by Park in [55]. The inverse of this mapping,

$$\dot{q} = \mathcal{A}^{-1}(q)\omega, \tag{2.27}$$

$A^{-1} : \mathbb{R}^3 \to \mathbb{R}^{3\times 3}$ also has a closed functional form given by

$$\mathcal{A}^{-1}(q) = I_{3\times 3} - \frac{1}{2}\mathcal{J}(q) + \left(1 - \frac{\|q\|}{2}\cot\frac{\|q\|}{2}\right)\frac{\mathcal{J}(q)^2}{\|q\|^2}. \tag{2.28}$$

This inverse exists for $\|q\| < \pi$ [55]. See [12, 16] for additional properties.

2.4.2 Rotating and Translating Rigid-Body Kinematics

We use seven state representations of rigid-body pose and velocity:

- $\psi \in \mathbb{R}^6$, the pose in se(3) exponential coordinates,
- $v \in \mathbb{R}^6$, the body-frame velocity,
- $H \in \mathrm{SE}(3)$, the homogenious transform from the body-frame to the world-frame,
- $R \in \mathrm{SO}(3)$, the rotation matrix from the body-frame to the world-frame,
- $p \in \mathbb{R}^3$, the vector representing the body-frame's origin in the world-frame,
- $\nu \in \mathbb{R}^3$, the vehicle's body-frame translational velocity, and
- $\omega \in \mathbb{R}^6$, the vehicle's body-frame angular velocity.

The relations between these state representations are given by

$$H = e^{\widehat{\psi}}, \tag{2.29}$$

$$\dot{H} = H\widehat{v}, \tag{2.30}$$

$$H = \begin{bmatrix} R & p \\ 0_{1\times 3} & 1 \end{bmatrix}, \text{ and} \tag{2.31}$$

$$v = \begin{bmatrix} \nu \\ \omega \end{bmatrix}. \tag{2.32}$$

We employ the inverse SE(3) velocity Jacobian, $\hat{\mathcal{A}}^{-1} : \mathbb{R}^6 \rightarrow \mathbb{R}^{6\times 6}$, as a relation between the body-frame velocity and time derivative of exponential coordinate pose

$$\dot{\psi} = \hat{\mathcal{A}}^{-1}(\psi)v. \tag{2.33}$$

In [13] the authors derive a closed form expression for this matrix valued function, reprinted in Appendix B as (B.2). To the best of the author's knowledge a closed form expression for the SE(3) angular velocity Jacobian, $\hat{\mathcal{A}}(\psi)$, has not been reported. Appendix B provides further information on this Jacobian, including the derivation of a simpler closed form (B.5), proof that $\psi^T \left(\hat{\mathcal{A}}^{-T}(\psi) + \hat{\mathcal{A}}^{-1}(\psi)\right)\psi = \psi^T\psi$ (Appendix B.1), and an upper bound for $\|\hat{\mathcal{A}}^{-1}(\psi)x\|$ (Appendix B.2).

2.5 Rigid-Body Plants Subject to External Torques

This Section introduces the dynamics model for a second-order rotational plant and rotating UV.

2.5.1 3-DOF Rotational Dynamics Model

The commonly accepted model of a rigid-body rotating under the influence of an external torque $\tau \in \mathbb{R}^3$ is given by

$$\dot{R} = R\widehat{\omega}$$

$$\dot{\omega} = I^{-1}\left(\mathcal{J}\left(I\omega\right)\omega + \tau\right) \tag{2.34}$$

where $\omega \in \mathbb{R}^3$ is the plant's angular velocity, $R \in \mathrm{SO}(3)$ is the plant's rotational position, and $I \in \mathbb{R}^{3\times 3}$ is the plant's PDS inertia tensor [67].

An alternate form of plant dynamics can be developed using a regressor matrix since the second equality in (2.34) is linear I, the plant's inertia tensor. Let $\lambda_1, \cdots, \lambda_6 \in \mathbb{R}$ be the six unique scalars in I such that $I = \begin{bmatrix} \lambda_1 & \lambda_2 & \lambda_3 \\ \lambda_2 & \lambda_4 & \lambda_5 \\ \lambda_3 & \lambda_5 & \lambda_6 \end{bmatrix}$. Defining the matrix P_I as

$$P_I = \begin{bmatrix} 1 & 0 & 0 & 0 & 0 & 0 \\ 0 & 1 & 0 & 0 & 0 & 0 \\ 0 & 0 & 1 & 0 & 0 & 0 \\ 0 & 1 & 0 & 0 & 0 & 0 \\ 0 & 0 & 0 & 1 & 0 & 0 \\ 0 & 0 & 0 & 0 & 1 & 0 \\ 0 & 0 & 1 & 0 & 0 & 0 \\ 0 & 0 & 0 & 0 & 1 & 0 \\ 0 & 0 & 0 & 0 & 0 & 1 \end{bmatrix}, \tag{2.35}$$

and θ_I as

$$\theta_I = \begin{bmatrix} \lambda_1 & \lambda_2 & \lambda_3 & \lambda_4 & \lambda_5 & \lambda_6 \end{bmatrix}^T \tag{2.36}$$

we have the relation

$$I^S = P_I\theta_I. \tag{2.37}$$

The second equality in (2.34) can be factored as

$$\begin{aligned} \tau(t) &= \left(\dot{\omega}(t)^T \otimes \mathbb{I} + \omega(t)^T \otimes \mathcal{J}(\omega(t))\right) P_I\theta_I \\ &= \mathbb{W}_I(\omega, \dot{\omega})\theta_I, \end{aligned} \tag{2.38}$$

where $\mathbb{I} \in \mathbb{R}^{3\times3}$ is the identity matrix and

$$\mathbb{W}_I(\omega, \dot{\omega}) = \dot{\omega}(t)^T \otimes \mathbb{I} + \omega(t)^T \otimes \mathcal{J}(\omega(t))P_I. \tag{2.39}$$

2.5.2 3-DOF UV Rotational Dynamics Model

Modeling a submerged rotating rigid-body requires accounting for the surrounding fluid. The most commonly employed plant models for UV are finite dimensional lumped-parameter approximate models with vehicle-specific plant parameter terms including mass and added mass parameters; quadratic drag parameters; and gravity and buoyancy parameters. Previous studies have shown that including explicit terms for the quadratic drag and buoyancy torque within (2.34) results in a model which approximates the dynamics of a rotating UV [45]. Therefore, we model the rotational dynamics of an UV as

$$\begin{aligned} \dot{R} &= R\mathcal{J}(\omega) \\ \dot{\omega} &= I^{-1}\left(\mathcal{J}(I\omega)\omega + \left(\sum_{i=1}^{3}|\omega_i|C_i\right)\omega + \mathcal{J}(b)R^T e_3 + \tau\right) \end{aligned} \tag{2.40}$$

where I is the UV's inertia tensor, $e_3 = \begin{bmatrix} 0 & 0 & 1 \end{bmatrix}^T$, $C_1, C_2, C_3 \in \mathbb{R}^{3\times3}$ make up a general three DOF coupled quadratic drag matrix, and $b \in \mathbb{R}^3$ represents the torque applied to the vehicle due to the relative positions of the UV's center-of-gravity (COG) and center-of-buoyancy (COB). Quadratic drag is assumed to be dissipative thus, $\omega^T\left(\sum_{i=1}^{3}|\omega_i|C_i\right)\omega \leq 0$ for all $\omega \in \mathbb{R}^3$ — i.e. the symmetric part of $\sum_{i=1}^{3}|\omega_i|C_i$ is negative definite.

The second equality in (2.40) is linear in the plant parameters. Thus, an alternate form of UV rotational dynamics can be developed using a regressor matrix. Let the UVR sub-

script denote *UV rotational dynamics* and define $\theta_{UVR} \in \mathbb{R}^{36}$ as

$$\theta_{UVR} = \left[\theta_I^T \ (C_1^S)^T \ (C_2)^T \ (C_3^S)^T \ b^T\right]^T. \tag{2.41}$$

Then the second equality in (2.40) can be factored as

$$\begin{aligned}\tau(t) &= \begin{bmatrix} \mathbb{W}_I(\omega, \dot{\omega}) & -|\omega_1|\omega^T \otimes \mathbb{I} & -|\omega_2|\omega^T \otimes \mathbb{I} & -|\omega_3|\omega^T \otimes \mathbb{I} & \mathcal{J}(R^T e_3) \end{bmatrix} \theta_{UVR} \\ &= \mathbb{W}_{UVR}(\omega, \dot{\omega}, R)\theta_{UVR} \end{aligned} \tag{2.42}$$

where

$$\mathbb{W}_{UVR} = \begin{bmatrix} \mathbb{W}_I(\omega, \dot{\omega}) & -|\omega_1|\omega^T \otimes \mathbb{I} & -|\omega_2|\omega^T \otimes \mathbb{I} & -|\omega_3|\omega^T \otimes \mathbb{I} & \mathcal{J}(R^T e_3) \end{bmatrix}. \tag{2.43}$$

2.6 6-DOF UV Dynamics Model

Using the state representation conventions of Section 2.4.2, we represent the pose and velocity of an UV with $H \in \mathrm{SE}(3)$ and $v \in \mathbb{R}^6$ respectively. We model a UV as a rigid-body with added hydrodynamic mass, quadratic drag, gravitational force, and buoyancy torque moving under the influence of external torques $\tau \in \mathbb{R}^3$ and forces $f \in \mathbb{R}^3$. The commonly accepted second-order finite-dimensional lumped parameter dynamic model for fully submerged rigid-body UV, written in the body-frame, is

$$\begin{aligned} \dot{H} =& H\widehat{v} \\ M\dot{v} =& \mathrm{ad}_v^T (Mv) + \left(\sum_{i=1}^{6} |v_i| D_i \right) v + \mathcal{G}(R) + u \end{aligned} \tag{2.44}$$

where $\mathcal{G}(R) = \begin{bmatrix} gR^T e_3 \\ \mathcal{J}(b) R^T e_3 \end{bmatrix}$, $e_3 = \begin{bmatrix} 0 \\ 0 \\ 1 \end{bmatrix}$, $u = \begin{bmatrix} f \\ \tau \end{bmatrix}$, $M \in \mathbb{R}^{6\times 6}$ is the vehicle's mass matrix, the set $D_i \in \mathbb{R}^{6\times 6}$ ($i = 1 \cdots 6$) are the 6 DOF fully-coupled quadratic drag coefficients, $g \in \mathbb{R}$ is the net vertical force acting on the vehicle due to gravity and buoyancy (i.e. the net buoyancy), and $b \in \mathbb{R}^3$ is the torque applied to the vehicle due to the relative positions of the COG and COB (which will vary as a function of the vehicle's roll and pitch) [18].

Although the model (2.44) is derived empirically, its structure is well established in the literature [18]. Previous studies have demonstrated this model's capacity to approximate UV dynamics following typical operational trajectories and justified this model's exclusion of a linear drag term [45]. The parameters M, D, g, and b are expected to have the following properties:

- the mass matrix M is PDS, the sum of the vehicle's rigid-body mass matrix and its hydrodynamic added-mass matrix;
- the scalar g is the net difference of the force of gravity and force of buoyancy on the vehicle and is reported in newtons;

- the vector $b \in \mathbb{R}^3$ is the body-frame COB position multiplied by the force of buoyancy added to the body-frame COG position multiplied by the force of gravity and is reported in newton meters; and

- the quadratic drag D is dissipative (i.e. $v^T \left(\sum_{i=1}^{6} |v_i| D_i \right) v \leq 0$ for all $v \in \mathbb{R}^6$ or, equivalently, the symmetric part of $\sum_{i=1}^{6} |v_i| D_i$ is negative definite).

An alternate form of UV dynamics can be developed using a regressor matrix since the second equality in (2.44) is linear in M, D, g, and b. Let $\{m_1, \cdots, m_{21}\}$ be the 21 unique scalar values in M such that

$$M = \begin{bmatrix} m_1 & m_2 & m_3 & m_4 & m_5 & m_6 \\ m_2 & m_7 & m_8 & m_9 & m_{10} & m_{11} \\ m_3 & m_8 & m_{12} & m_{13} & m_{14} & m_{15} \\ m_4 & m_9 & m_{13} & m_{16} & m_{17} & m_{18} \\ m_5 & m_{10} & m_{14} & m_{17} & m_{19} & m_{20} \\ m_6 & m_{11} & m_{15} & m_{18} & m_{20} & m_{21} \end{bmatrix}. \tag{2.45}$$

Defining the matrix P_M as

$$P_M = \begin{bmatrix}
1 & 0 & 0 & 0 & 0 & 0 & 0 & 0 & 0 & 0 & 0 & 0 & 0 & 0 & 0 & 0 & 0 & 0 & 0 & 0 \\
0 & 1 & 0 & 0 & 0 & 0 & 0 & 0 & 0 & 0 & 0 & 0 & 0 & 0 & 0 & 0 & 0 & 0 & 0 & 0 \\
0 & 0 & 1 & 0 & 0 & 0 & 0 & 0 & 0 & 0 & 0 & 0 & 0 & 0 & 0 & 0 & 0 & 0 & 0 & 0 \\
0 & 0 & 0 & 1 & 0 & 0 & 0 & 0 & 0 & 0 & 0 & 0 & 0 & 0 & 0 & 0 & 0 & 0 & 0 & 0 \\
0 & 0 & 0 & 0 & 1 & 0 & 0 & 0 & 0 & 0 & 0 & 0 & 0 & 0 & 0 & 0 & 0 & 0 & 0 & 0 \\
0 & 0 & 0 & 0 & 0 & 1 & 0 & 0 & 0 & 0 & 0 & 0 & 0 & 0 & 0 & 0 & 0 & 0 & 0 & 0 \\
0 & 1 & 0 & 0 & 0 & 0 & 0 & 0 & 0 & 0 & 0 & 0 & 0 & 0 & 0 & 0 & 0 & 0 & 0 & 0 \\
0 & 0 & 0 & 0 & 0 & 0 & 1 & 0 & 0 & 0 & 0 & 0 & 0 & 0 & 0 & 0 & 0 & 0 & 0 & 0 \\
0 & 0 & 0 & 0 & 0 & 0 & 0 & 1 & 0 & 0 & 0 & 0 & 0 & 0 & 0 & 0 & 0 & 0 & 0 & 0 \\
0 & 0 & 0 & 0 & 0 & 0 & 0 & 0 & 1 & 0 & 0 & 0 & 0 & 0 & 0 & 0 & 0 & 0 & 0 & 0 \\
0 & 0 & 0 & 0 & 0 & 0 & 0 & 0 & 0 & 1 & 0 & 0 & 0 & 0 & 0 & 0 & 0 & 0 & 0 & 0 \\
0 & 0 & 0 & 0 & 0 & 0 & 0 & 0 & 0 & 0 & 1 & 0 & 0 & 0 & 0 & 0 & 0 & 0 & 0 & 0 \\
0 & 0 & 1 & 0 & 0 & 0 & 0 & 0 & 0 & 0 & 0 & 0 & 0 & 0 & 0 & 0 & 0 & 0 & 0 & 0 \\
0 & 0 & 0 & 0 & 0 & 0 & 0 & 1 & 0 & 0 & 0 & 0 & 0 & 0 & 0 & 0 & 0 & 0 & 0 & 0 \\
0 & 0 & 0 & 0 & 0 & 0 & 0 & 0 & 0 & 0 & 0 & 1 & 0 & 0 & 0 & 0 & 0 & 0 & 0 & 0 \\
0 & 0 & 0 & 0 & 0 & 0 & 0 & 0 & 0 & 0 & 0 & 0 & 1 & 0 & 0 & 0 & 0 & 0 & 0 & 0 \\
0 & 0 & 0 & 0 & 0 & 0 & 0 & 0 & 0 & 0 & 0 & 0 & 0 & 1 & 0 & 0 & 0 & 0 & 0 & 0 \\
0 & 0 & 0 & 1 & 0 & 0 & 0 & 0 & 0 & 0 & 0 & 0 & 0 & 0 & 0 & 0 & 0 & 0 & 0 & 0 \\
0 & 0 & 0 & 0 & 0 & 0 & 0 & 0 & 1 & 0 & 0 & 0 & 0 & 0 & 0 & 0 & 0 & 0 & 0 & 0 \\
0 & 0 & 0 & 0 & 0 & 0 & 0 & 0 & 0 & 0 & 0 & 0 & 1 & 0 & 0 & 0 & 0 & 0 & 0 & 0 \\
0 & 0 & 0 & 0 & 0 & 0 & 0 & 0 & 0 & 0 & 0 & 0 & 0 & 0 & 0 & 1 & 0 & 0 & 0 & 0 \\
0 & 0 & 0 & 0 & 0 & 0 & 0 & 0 & 0 & 0 & 0 & 0 & 0 & 0 & 0 & 0 & 1 & 0 & 0 & 0 \\
0 & 0 & 0 & 0 & 0 & 0 & 0 & 0 & 0 & 0 & 0 & 0 & 0 & 0 & 0 & 0 & 0 & 1 & 0 & 0 \\
0 & 0 & 0 & 0 & 1 & 0 & 0 & 0 & 0 & 0 & 0 & 0 & 0 & 0 & 0 & 0 & 0 & 0 & 0 & 0 \\
0 & 0 & 0 & 0 & 0 & 0 & 0 & 0 & 0 & 1 & 0 & 0 & 0 & 0 & 0 & 0 & 0 & 0 & 0 & 0 \\
0 & 0 & 0 & 0 & 0 & 0 & 0 & 0 & 0 & 0 & 0 & 0 & 0 & 1 & 0 & 0 & 0 & 0 & 0 & 0 \\
0 & 0 & 0 & 0 & 0 & 0 & 0 & 0 & 0 & 0 & 0 & 0 & 0 & 0 & 0 & 0 & 1 & 0 & 0 & 0 \\
0 & 0 & 0 & 0 & 0 & 0 & 0 & 0 & 0 & 0 & 0 & 0 & 0 & 0 & 0 & 0 & 0 & 1 & 0 & 0 \\
0 & 0 & 0 & 0 & 0 & 0 & 0 & 0 & 0 & 0 & 0 & 0 & 0 & 0 & 0 & 0 & 0 & 0 & 1 & 0 \\
0 & 0 & 0 & 0 & 0 & 0 & 0 & 0 & 0 & 0 & 0 & 0 & 0 & 0 & 0 & 0 & 0 & 0 & 0 & 1
\end{bmatrix}, \quad (2.46)$$

and θ_M as a vector of the unique scalar terms m_i from M in numerical order, we have the

relation

$$M^S = P_M \theta_M. \tag{2.47}$$

Let the UV subscript denotes 6-DOF UV dynamics and define θ_{UV} as

$$\theta_{UV} = \begin{bmatrix} \theta_M^T & (D_1^S)^T & (D_2^S)^T & (D_3^S)^T & (D_4^S)^T & (D_5^S)^T & (D_6^S)^T & g & b^T \end{bmatrix}^T. \tag{2.48}$$

Then the second equality in (2.44) can be factored as

$$\begin{aligned} u(t) &= \begin{bmatrix} \mathbb{W}_M(v, \dot{v}) & \mathbb{W}_D(v) & \mathbb{W}_{gb}(R) \end{bmatrix} \theta \\ &= \mathbb{W}_{UV}(v, \dot{v}, R)\theta_{UV} \end{aligned} \tag{2.49}$$

using the following definitions

- $\mathbb{W}_M(v, \dot{v}) = \left(\dot{v}(t)^T \otimes \mathbb{I} + v^T \otimes \mathrm{ad}(v)\right) P_M$,
- $\mathbb{W}_{Di}(v) = -|v_i| v^T \otimes \mathbb{I}$ for all $i \in \{1, \cdots, 6\}$,
- $\mathbb{W}_D(v) = \begin{bmatrix} \mathbb{W}_{D1}(v) & \mathbb{W}_{D2}(v) & \mathbb{W}_{D3}(v) & \mathbb{W}_{D4}(v) & \mathbb{W}_{D5}(v) & \mathbb{W}_{D6}(v) \end{bmatrix}$,
- $\mathbb{W}_{gb}(R) = \begin{bmatrix} -R^T e_3 & 0_{3\times 3} \\ 0_{3\times 1} & \mathcal{J}(R^T e_3) \end{bmatrix}$, and
- $\mathbb{W}_{UV} = \begin{bmatrix} \mathbb{W}_M(v, \dot{v}) & \mathbb{W}_D(v) & \mathbb{W}_{gb}(R) \end{bmatrix}$.

2.7 Open Kinematic Chain Dynamics Model

In Section 3.4 a parameter identification algorithm for an *n*-link OKC is reported. Let $\mathfrak{J} \subset \mathbb{R}^n$ be the joint space of a *n*-link OKC, a commonly accepted model for this plant is

$$\tau = M(q)\ddot{q} + C(q,\dot{q})\dot{q} + \mathfrak{g}(q), \tag{2.50}$$

where $q \in \mathfrak{J}$ is the vector of OKC joint angles, $\tau \in \mathbb{R}^n$ is the vector of torque inputs applied at each joint, $M \in \mathfrak{J} \to \mathbb{R}^{n\times n}$ is the mass matrix, $C \in \mathfrak{J} \times \mathbb{R}^n \to \mathbb{R}^{n\times n}$ is the Coriolis matrix, and $\mathfrak{g} \in \mathfrak{J} \to \mathbb{R}^n$ is the gravity vector. Note that for all OKCs there exist functions $M(q)$, $C(q,\dot{q})$, and $\mathfrak{g}(q)$ such that $M(q)$ is PDS and $\dot{M}(q) - 2C(q,\dot{q})$ is skew symmetric [66]. In the parameter identification algorithm presented, I assume that there exist r unknown scalar parameters which enter linearly into the functions $M(q)$, $C(q,\dot{q})$, and $\mathfrak{g}(q)$. This assumption is common in the robotics literature; applies to a wide class of robotic manipulators; and allows (2.50) to be factored as

$$M(a)b + C(a,c)d + \mathfrak{g}(a) = \mathbb{W}_{OKC}(b,a,c,d)\theta_{OKC} \tag{2.51}$$

for all $a,b,c,d \in \mathbb{R}^n$ where $\theta_{OKC} \in \mathbb{R}^r$ is a vector of the parameters in the manipulator model [17].

Chapter 3

State Estimation and Parameter Identification for Simple Mechanical Systems: Second-Order Rotational Plants and Open Kinematic Chains

This Thesis reports advances in state estimation, parameter identification, and control algorithms applicable to underwater vehicles (UVs). Chapters 4 and 5 present the development and experimental evaluation of UV algorithms. However, the theoretical antecedents of these algorithms are state and parameter estimation algorithms for a broader class of simple mechanical systems (SMSs). This Chapter presents three separate algorithms: an angular velocity observer for a second-order rotating rigid-body plant (Section 3.2); an

adaptive identification algorithm for the inertia tensor of a second-order rotating rigid-body plant (Section 3.3); and an adaptive identification algorithm for the dynamic parameters of an open kinematic chain (OKC) (Section 3.4).

The angular velocity observer and the inertia tensor adaptive identification (AID) algorithm address 3-degree-of-freedom (DOF) second-order rotating rigid-body plants. As such, they are applicable for a number of space, air, and marine vehicle applications. The AID algorithm for second-order rotational plants preforms dynamic estimation of the inertia tensor from input-output signals. In a variety of undersea, space, and air vehicle missions, the vehicle inertia tensor varies dynamically as consumables and payload vary over the duration of a mission. Thus dynamic inertia tensor estimation could facilitate forward modeling and model-based control with such vehicles.

The OKC AID algorithm estimates the plant model dynamic parameters that enter linearly into a general class of nonlinear second-order holonomic plants, including robotic manipulators. Dynamic parameters that enter linearly into the plant model such as mass, inertia, and friction coefficients can be estimated. Most previously reported AID algorithms methods for this class of plants have focused on model-based adaptive tracking controllers. However these approaches are not applicable when the manipulator is either uncontrolled, under open-loop control, under actuated, or is using any control law other than a specific adaptive tracking controller. The AID reported herein does not require any particular control algorithm and is also suitable for uncontrolled plants. In the case of both AID algorithms presented in this Chapter, continuous parameter monitoring of plant parameters

may enable the detection of unexpected changes that indicate system failures.

The AID algorithm presented in Section 3.3.1 was originally reported in 2012 [47].

3.1 Literature Review

State estimation and parameter identification algorithms for simple mechanical systems (SMSs) has been an active research area for over three decades. Controllers and observers that do not require access to angular velocity have been developed for plants for the form (2.34). Lizarralde and Wen reported an attitude controller for (2.34) that does not require access to angular velocity [38]. In [60] Salcudean reported a stable velocity observer for plants of the form (2.34) using unit quaternion representation of plant angular position. In [2] the authors report general results for intrinsic observers on a broad class of Lagrangian systems. In [43] the authors use the general result of [2] to address the special case of observers for mechanical systems on a Lie group. In [41, 42] the authors address the problem of developing complementary filters for the special orthogonal group in the presence of noisy velocity data. In [9] the authors apply the general approach of [41, 42] to develop observers for second-order SE(3) plants.

A broad class of nonlinear model-based trajectory tracking controllers developed since the 1980's — for example Koditschek's nonlinear tracking controller for second-order rotating plants [35] and exactly linearizing model-based trajectory tracking controllers for OKCs [20, 39] — require exact knowledge of the plant's kinematic and dynamic parame-

ters. Although kinematic parameters are often easily obtained, dynamic parameters generally must be measured empirically. Most previously reported parameter identification methods for OKCs employ one of two general approaches: (i) linear regression of experimental data or (ii) adaptive model-based trajectory tracking control.

A variety of previously reported studies have employed least-squares, total least-squares, or extended Kalman filters to identify plant parameters entering linearly into the plant equations of motion for robot manipulators [4,32], UV [3,14,44], and spacecraft [29,54]. Khalil and Dombre provide a summary of this work [30].

The problem of adaptive model-based reference trajectory tracking is well understood for several types of second-order holonomic nonlinear plants whose parameters enter linearly into the plant equations of motion, e.g., robot manipulator arms [17,59,63], UVs [27], spacecraft [36, 62], and general mechanical systems [37]. The previously reported result most closely related to the adaptive identifier reported herein is reported in [15], which addresses the specific problem of adaptive model-based tracking control of rotational plants of the form (2.34). [24] reports an adaptive identification algorithm for OKCs that employs a low pass filter approach for the parameter update law to avoid instrumenting joint acceleration, and reports a numerical simulation. Other than [24], although a great variety of adaptive model-based trajectory tracking controllers have been developed, to the best of our knowledge the corresponding model-based AID algorithm — without requiring simultaneous trajectory tracking control — have not been reported.

Adaptive methods for parameter identification of linear plants are well understood [6,

51, 61] and have been employed for a few application-specific nonlinear models, such as decoupled model for UVs [64]. To the best of our knowledge, the AID algorithm reported in Section 3.3 is the first reported inertia tensor adaptive estimation method for rotational plants of the form (2.34) *without* the additional need to simultaneously perform reference trajectory tracking. Section 3.4 reports an AID algorithm which does not require joint acceleration signals and provides physically feasible models.

3.2 Angular Velocity Observation for 3-DOF Rotational Plants

This Section addresses the velocity observer problem for three-dimensional second-order rotational plants of the form (2.34) when the signals of torque input and angular position are available, but the signal of plant angular velocity is unavailable. Using the input torque signal, angular position signal, and plant's known inertia tensor the goal of the velocity observer is to asymptotically exactly estimate the plant's unknown angular velocity.

This Section presents a novel angular velocity observer, along with an analysis of its stability. A comparative analysis of the novel and two previously reported nonlinear angular velocity observers is presented. Numerical simulations of all three show convergence of the observer state to the plant state and similar performance for most angular position trajectories and inertia tensors.

3.2.1 Velocity Observer from Body Frame

Consider the model of a rotating rigid-body under the influence of an external torque, τ, of the form (2.34) with angular position, R, and angular velocity, ω, repeated here for the reader as

$$\begin{aligned} \dot{R} &= R\widehat{\omega} \\ \dot{\omega} &= I^{-1}\left(\mathcal{J}\left(I\omega\right)\omega + \tau\right). \end{aligned} \tag{3.1}$$

Assume the plant's positive definite symmetric (PDS) inertia tensor, I, input torque signal, and angular position signal are known but the angular velocity signal is unknown. Without loss of generality we can assume I is diagonal with eigenvalues $0 < \lambda_3 \leq \lambda_2 \leq \lambda_1 < \infty$ in some arbitrary order along the diagonal. We define the observer states as $\hat{R}$ and $\hat{\omega}$, estimates of the plant's angular position R and angular velocity ω respectively. We define the error signals as

$$\Delta R = \hat{R}^T R \tag{3.2}$$

$$\Delta q = \log_{\mathrm{SO(3)}}(\Delta R) \tag{3.3}$$

$$\psi = \Delta R^T \hat{\omega} \tag{3.4}$$

$$\Delta\omega = \omega - \psi. \tag{3.5}$$

The remainder of this Section analyzes the stability of the previously unreported nonlinear angular velocity observer

$$\begin{aligned}\dot{\hat{R}} =&\hat{R}\mathcal{J}\left(\hat{\omega} - \Delta R\mathcal{A}(\Delta q)L\Delta q\right)\\ \dot{\hat{\omega}} =&\Delta R\left(I^{-1}\left(\mathcal{J}\left(I\psi\right)\psi + \tau + \Delta q\right) - \mathcal{J}(\psi)\mathcal{A}(\Delta q)L\Delta q\right)\end{aligned} \tag{3.6}$$

where $L \in \mathbb{R}^{3\times 3}$ is a observer gain matrix (possibly a function of ψ) yet to be determined.

3.2.1.1 Error System

The time derivative of (3.2) is

$$\begin{aligned}\Delta\dot{R} &= \dot{\hat{R}}^T R + \hat{R}^T\dot{R}\\ &= \Delta R\mathcal{J}\left(\Delta\omega + \mathcal{A}(\Delta q)L\Delta q\right)\end{aligned} \tag{3.7}$$

thus

$$\begin{aligned}\Delta\dot{q} &= \mathcal{A}^{-1}(\Delta q)\left(\Delta\omega + \mathcal{A}(\Delta q)L\Delta q\right)\\ &= L\Delta q + \mathcal{A}^{-1}(\Delta q)\Delta\omega.\end{aligned} \tag{3.8}$$

The time derivative of (3.5) is

$$\begin{aligned}\Delta\dot{\omega} =&\dot{\omega} - \Delta\dot{R}^T\hat{\omega} - \Delta R^T\dot{\hat{\omega}}\\ =&I^{-1}\left(\mathcal{J}\left(I\omega\right)\omega + \tau\right) + \mathcal{J}\left(\Delta\omega + \mathcal{A}(\Delta q)L\Delta q\right)\psi\\ &- I^{-1}\left(\mathcal{J}\left(I\psi\right)\psi + \tau + \Delta q\right) + \mathcal{J}(\psi)\mathcal{A}(\Delta q)L\Delta q\\ =&I^{-1}\left(\mathcal{J}\left(I\omega\right)\omega + I\mathcal{J}\left(\Delta\omega\right)\psi - \mathcal{J}\left(I\psi\right)\psi\right) - I^{-1}\Delta q\\ =&-I^{-1}\Delta q + I^{-1}\left(-I\mathcal{J}(\psi) + \mathcal{J}\left(I\omega\right) - \mathcal{J}(\psi)I\right)\Delta\omega,\end{aligned} \tag{3.9}$$

where this final equality makes use of the fact that

$$\mathcal{J}(I\omega)\omega + I\mathcal{J}(\Delta\omega)\psi - \mathcal{J}(I\psi)\psi = \mathcal{J}(I\omega)(\Delta\omega + \psi) - I\mathcal{J}(\psi)\Delta\omega - \mathcal{J}(I\psi)\psi$$
$$= (\mathcal{J}(I\omega) - I\mathcal{J}(\psi) - \mathcal{J}(\psi)I)\Delta\omega.$$

Define

$$\mathcal{B}(\omega, \psi) = -I\mathcal{J}(\psi) + \mathcal{J}(I\omega) - \mathcal{J}(\psi)I, \tag{3.10}$$

clearly $\mathcal{B}^T(\omega, \psi) = -\mathcal{B}(\omega, \psi)$ and thus $\mathcal{B}(\omega, \psi)$ is skew-symmetric. Defining

$$x = \begin{bmatrix} \Delta q \\ \Delta\omega \end{bmatrix} \tag{3.11}$$

and

$$\mathbb{A}(x, \omega, \psi) = \begin{bmatrix} L & \mathcal{A}^{-1}(\Delta q) \\ -I^{-1} & I^{-1}\mathcal{B}(\omega, \psi) \end{bmatrix}, \tag{3.12}$$

from (3.8) and (3.9), the full error system takes the form

$$\dot{x} = \mathbb{A}(x, \omega, \psi)x. \tag{3.13}$$

3.2.1.2 Stability Analysis

Theorem 3.2.1 *Consider the error system of the form of (3.13) with the following assumptions:*

- *The plant satisfies the condition* $4\lambda_3 > \lambda_1$*, and*
- $L(\psi)$ *in the observer is set such that* $L(\psi) = -E + F(\psi)$ *where* E *is a constant positive definite matrix,* $F(\psi) = -I^{1/2}\mathcal{J}(\psi)I^{-1/2} + I^{-1/2}\mathcal{J}(I\psi)I^{-1/2} - I^{-1/2}\mathcal{J}(\psi)I^{1/2}$ *and* $\psi = \Delta R^T\hat{\omega}$*.*

This error system is locally asymptotically stable in the sense of Lyapunov for a neighborhood of $x = \vec{0}$.

Proof: Note that for ϵ small enough the Lyapunov function

$$\mathfrak{L}_\epsilon = \frac{1}{2} x^T P_\epsilon x \tag{3.14}$$

is

- positive definite
- equal to zero if and only if $x = \vec{0}$

where

$$P_\epsilon = \begin{bmatrix} \mathbb{I} & -\epsilon I^{1/2} \\ -\epsilon I^{1/2} & I \end{bmatrix}, \tag{3.15}$$

$\mathbb{I}$ is the identity matrix, and I is the plant's inertia tensor.

In the sequel the explicit functional dependencies of $\mathcal{A}$, $\mathcal{B}$, and L are no longer specified. This compact notation improves the clarity of the equations. However, in this and all future equations: $\mathcal{A}$ denotes $\mathcal{A}(\Delta q)$, $\mathcal{B}$ denotes $\mathcal{B}(\psi, \omega)$, and L denotes $L(\psi)$. Consider $\dot{\mathfrak{L}}_\epsilon$ given

by

$$\begin{aligned}
\dot{\mathfrak{L}}_\epsilon =& \frac{1}{2}\dot{x}^T P_\epsilon x + \frac{1}{2}x^T P_\epsilon \dot{x} \\
=& \frac{1}{2}x^T \left(\mathbb{A}^T P_\epsilon + P_\epsilon \mathbb{A}\right) x \\
=& \frac{1}{2}x^T \begin{bmatrix} L^T + L + 2\epsilon I^{-1/2} & -\epsilon L^T I^{1/2} - \mathbb{I} + \mathcal{A}^{-1} - \epsilon I^{-1/2}\mathcal{B} \\ \mathcal{A}^{-T} + \epsilon\mathcal{B}I^{-1/2} - \epsilon I^{1/2}L - \mathbb{I} & -\epsilon\mathcal{A}^{-T}I^{1/2} + \mathcal{B}^T - \epsilon I^{1/2}\mathcal{A}^{-1} + \mathcal{B} \end{bmatrix} x \\
=& \frac{1}{2}x^T \begin{bmatrix} -2E + 2\epsilon I^{-1/2} & -\epsilon\left(-EI^{1/2} + I^{-1/2}\mathcal{J}\left(I\Delta\omega\right)\right) \\ -\epsilon\left(-I^{1/2}E - \mathcal{J}\left(I\Delta\omega\right)I^{-1/2}\right) & -\epsilon\left(\mathcal{A}^{-T}I^{1/2} + I^{1/2}\mathcal{A}^{-1}\right) \end{bmatrix} x.
\end{aligned} \tag{3.16}$$

The equality $L^T + L + 2\epsilon I^{-1/2} = -2E + 2\epsilon I^{-1/2}$ is a consequence of $F(\psi)$ being skew symmetric. The equality $-\epsilon\mathcal{A}^{-T}I^{1/2} + \mathcal{B}^T - \epsilon I^{1/2}\mathcal{A}^{-1} + \mathcal{B} = -\epsilon\left(\mathcal{A}^{-T}I^{1/2} + I^{1/2}\mathcal{A}^{-1}\right)$ is a consequence of $\mathcal{B}(\omega, \psi)$ being skew symmetric. The derivation of (3.16) also uses the facts that $\mathcal{A}^{-1}(\Delta q)\Delta q = \mathcal{A}^{-T}\Delta q = \Delta q$ implies

$$\Delta q^T\left(-\mathbb{I} + \mathcal{A}^{-1}\right)\Delta\omega = 0; \tag{3.17}$$

$-F(\psi)I^{1/2} + I^{-1/2}\mathcal{B}(\psi) = I^{-1/2}\mathcal{J}\left(I\Delta\omega\right)$ implies

$$\epsilon\left(L^T I^{1/2} + I^{-1/2}\mathcal{B}\right) = -\epsilon\left(-EI^{1/2} + I^{-1/2}\mathcal{J}\left(I\Delta\omega\right)\right); \tag{3.18}$$

and

$$L^T(\psi) = -E - F(\psi). \tag{3.19}$$

Since $\dot{\mathfrak{L}}_\epsilon$ depends only on Δq and $\Delta\omega$, $\dot{\mathfrak{L}}_\epsilon$ is bounded for all x such that $\|x\| < \pi$. First consider the term $-\epsilon\Delta\omega^T\left(\mathcal{A}^{-T}I^{1/2} + I^{1/2}\mathcal{A}^{-1}\right)\Delta\omega$. Noting the closed-form structure of

$\mathcal{A}^{-1}(\Delta q)$ from (2.28), the lower diagonal term of (3.16) obeys the following equality

$$\mathcal{A}^{-T} I^{1/2} + I^{1/2}\mathcal{A}^{-1} = 2I^{1/2} + \frac{1}{2}(-\mathcal{J}(\Delta q) I^{1/2} + I^{1/2}\mathcal{J}(\Delta q)) + \frac{1}{\|\Delta q\|^2}\left(1 - \frac{\|\Delta q\|}{2}\cot\left(\frac{\|\Delta q\|}{2}\right)\right)\left(\mathcal{J}(\Delta q)^2 I^{1/2} + I^{1/2}\mathcal{J}(\Delta q)^2\right).$$

The inequalities (2.10) from Section 2.2.2 and the fact $\left(1 - \frac{\|\Delta q\|}{2}\cot\left(\frac{\|\Delta q\|}{2}\right)\right) < 1 \quad \forall \|\Delta q\| \leq \|x\| < \pi$ imply

$$-\epsilon \Delta\omega^T \left(\mathcal{A}^{-T} I^{1/2} + I^{1/2}\mathcal{A}^{-1}\right)\Delta\omega \leq \epsilon(\lambda_1^{1/2}\|\Delta q\| + \lambda_1^{1/2} - 2\lambda_3^{1/2})\|\Delta\omega\|^2$$

$$\Delta q^T \left(-2E + 2\epsilon I^{-1/2}\right)\Delta q \leq -\left(2e_3 - \epsilon\lambda_1\right)\|\Delta q\|^2$$

$$-\epsilon \Delta q^T \left(\left(-E_1 I^{1/2} + I^{-1/2}\mathcal{J}(I\Delta\omega)\right)\right)\Delta\omega \leq \epsilon(e_{11}\lambda_1\|\Delta q\|\|\Delta\omega\| + \lambda_3^{1/2}\lambda_1\|\Delta q\|\|\Delta\omega\|^2).$$

In consequence

$$\begin{aligned} 2\dot{\mathfrak{L}}_\epsilon \leq & -\left(2e_{13} - \epsilon\lambda_1\right)\|\Delta q\|^2 + \epsilon\left(\lambda_1^{1/2}\|\Delta q\| + \lambda_1^{1/2} - 2\lambda_3^{1/2}\right)\|\Delta\omega\|^2 + \\ & 2\epsilon(e_{11}\lambda_1\|\Delta q\|\|\Delta\omega\| + \lambda_3^{1/2}\lambda_1\|\Delta q\|\|\Delta\omega\|^2) \\ \leq & -\left(2e_{13} - \epsilon\lambda_1\right)\|\Delta q\|^2 + \epsilon(\lambda_1^{1/2} - 2\lambda_3^{1/2})\|\Delta\omega\|^2 + \\ & \epsilon(2e_{11}\lambda_1 + 2\lambda_3^{1/2}\lambda_1\pi + \lambda_1^{1/2}\pi)\|\Delta q\|\|\Delta\omega\| \end{aligned} \tag{3.20}$$

$\forall\|\Delta\omega\| \leq \|x\| < \pi$. Define $a_1 = 2e_{11}\lambda_1 + 2\lambda_3^{1/2}\lambda_1\pi + \lambda_1^{1/2}\pi$, $a_2 = 2e_{13}$, $a_3 = \lambda_1$, $a_4 = -\lambda_1^{1/2} + 2\lambda_3^{1/2}$, and observe that

$$2\dot{\mathfrak{L}}_\epsilon \leq -z^T Q z \tag{3.21}$$

where

$$Q = \begin{bmatrix} a_2 - \epsilon a_3 & -\frac{\epsilon}{2}a_1 \\ -\frac{\epsilon}{2}a_1 & \epsilon a_4 \end{bmatrix} \tag{3.22}$$

and $z = \begin{bmatrix} \|\Delta q\| \\ \\ \|\Delta \omega\| \end{bmatrix}$. Q is negative definite if $\lambda_1 < 4\lambda_3$ and $\epsilon < \frac{4a_4a_2}{\|4a_4a_3 - a_1^2\|}$.

The local asymptotic stability of the angular velocity observer is proven. Note that accounting for the presence of the matrix valued function (3.10) in the error dynamics (3.13) as part of the stability analysis required careful selection of the Lyapunov function (3.14) and matrix valued function $F(\psi)$ from Theorem 3.2.1. Although Corollary 2.3.4 was not explicitly required for the stability analysis reported, the selections of $\mathfrak{L}(t)$ and $F(\psi)$ were enabled by this Corollary.

3.2.2 Velocity Observer from World Frame

In [60] Salcudean reports a velocity observer of the form:

$$\begin{aligned} \dot{\hat{R}} =& \mathcal{J}\left(\hat{R}R^T\left(\hat{\omega} + k_v \operatorname{sgn} y_o I_B^{-1} y\right)\right)\hat{R} \\ \frac{d}{dt}\left(I_B\hat{\omega}\right) =& \frac{1}{2}k_p I_B^{-1} y \operatorname{sgn}(y_o) + R^T\tau \end{aligned} \tag{3.23}$$

where $I_B = \hat{R}I\hat{R}^T$; $\Delta\bar{q} = \log_{\mathrm{SO}(3)}(R\hat{R}^T)$; $y = \frac{1}{\|\Delta\bar{q}\|}\sin\frac{\|\Delta q\|}{2}\Delta\bar{q}$; $y_o = \cos\frac{\|\Delta\bar{q}\|}{2}$; and k_v and k_p are positive scalar observer gains. Note that [60] uses the rotational error matrix $R\hat{R}^T$. This rotational error matrix structure is different than the definition used in this Section (3.2); it can not be interpreted as the transformation between the body-frame and observer-frame. Possible rotational error matrix choices are discussed further in [13].

3.2.3 Velocity Observer from Coordinate Free Perspective

In [43] Maithripala, Berg, and Dayawansa use a methodology similar to techniques from geometric control to develop an intrinsic observer on $\mathrm{SO}(3) \times \mathbb{R}^3$ as well as on similar invariant Lie groups. This study employs contraction analysis to show convergence of the observer state to plant state. This result relies on a more general intrinsic observer for simple mechanical systems on a general Riemannian manifold [2]. This study reports an intrinsic observer for a second-order rotational plant using exponential coordinates:

$$\begin{aligned}
\dot{\hat{R}} =& \hat{R}\mathcal{J}\left(\hat{\omega} - 2\alpha\Delta\tilde{q}\right) \\
\dot{\hat{\omega}} =& I^{-1}\left(\mathcal{J}\left(I\hat{\omega}\right)\hat{\omega} + \alpha\left(\mathcal{J}\left(I\hat{\omega}\right)\Delta\tilde{q} + \mathcal{J}\left(I\Delta\tilde{q}\right)\hat{\omega}\right)\right) \\
& - \alpha\mathcal{J}\left(\Delta\tilde{q}\right)\hat{\omega} - \Gamma(I^{-1}\tau, \Delta\tilde{q}) - J(\hat{\omega}, \Delta\tilde{q})\hat{\omega} - \beta\Delta\tilde{q},
\end{aligned} \tag{3.24}$$

where α and β are positive scalar observer gains and the error term is $\Delta\tilde{q} = \log_{\mathrm{SO}(3)}(R^T\hat{R})$. Note that [43] uses the rotational error matrix $R^T\hat{R}$; this is the transpose of the definition used in this Section (3.2). Using index summation notation for the following definitions $\Gamma(Y,\xi) = \left(Y^k - \nu_{ij}^k Y^i \xi^j\right) b_k$ and $J(\zeta,\xi)\eta = b_k\left(\mathcal{R}_{jab}^k \eta^j(\zeta^a\xi^b - \zeta^b\xi^a) - \nu_{ij}^k C_{ab}^i \zeta^a \eta^j\right)$ where b_k are a basis of the Lie algebra so(3), ν_{ij}^k are the Levi-Civita connection coefficients, C_{ji}^k are the structure constants, and $\mathcal{R}_{jab}^k$ are the curvature coefficients. Note that C_{ji}^k, ν_{ij}^k, and $\mathcal{R}_{jab}^k$ are constant for a selected basis b_k of so(3). The $\Gamma(Y,\xi)$ uses the concept of parallel transport to have the input torque τ act on this observer system in an equivalent fashion to the effect of τ on (2.34).

3.2.4 Angular Velocity Observer Comparative Numerical Simulation Study

This Section reports a comparative analysis of numerical simulations for the three angular velocity observers described in Sections 3.2.1, 3.2.2, and 3.2.3. We assume the plant's inertia tensor, I, is known and the signals of the plant rotational position, $q(t)$, and the plant torque input, $\tau(t)$, are available.

Each observer's performance was evaluated numerically using a fourth order Runge-Kutta numerical solution with fifth order error control. In every case during simulation the initial state of the observer was $\hat{q}(0) = \vec{0}$ and $\hat{\omega}(0) = \vec{0}$.

Plant position trajectories and control inputs satisfying (2.34) were generated numerically. Plant position trajectories, $q(t)$, were generated analytically as a sum of sines and cosines, each with different frequencies and amplitudes, such that $\|q(t)\| < \frac{\pi}{2}$. Corresponding plant velocity signals $\dot{q}(t)$ and $\omega(t)$ were similarly generated analytically. Plant signals $\dot{\omega}(t)$ and $\tau(t)$ were computed numerically. In this simulation study we report

- the body-frame observer (3.6) as Observer A,
- the world-frame observer (3.23) as Observer B, and
- the coordinate free observer (3.24) as Observer C.

Feedback gains appearing in the three observers differ in form and dimension. In an effort to achieve a fair comparison, we chose observer gains such that, when the observer

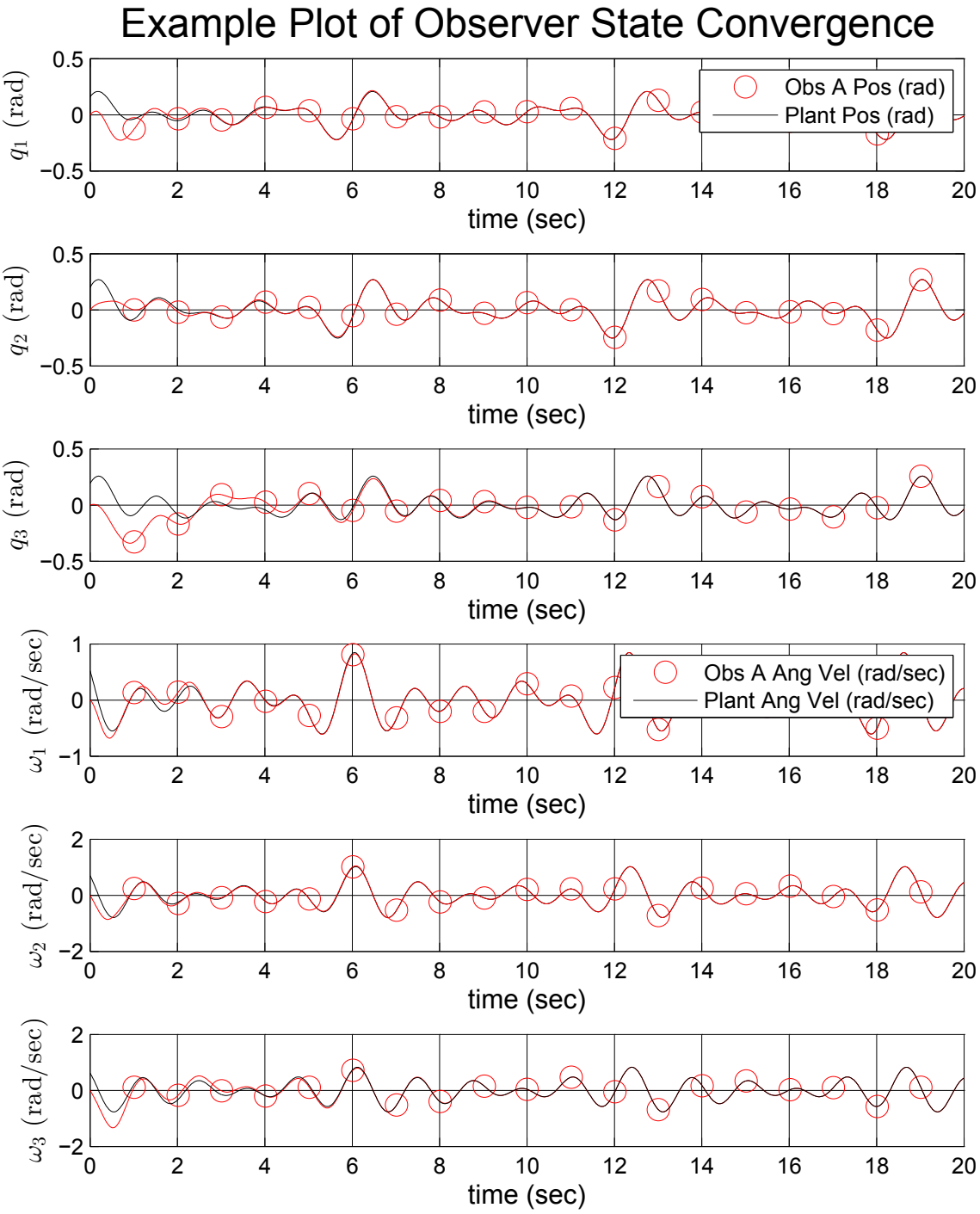

Figure 3.1: Angular position and angular velocity simulation the plant, (2.34), and Observer A, (3.6). Note convergence of Observer A state to plant state in each of the 6 DOF.

error systems were linearized about the equilibrium point $\Delta q = \Delta\bar{q} = \Delta\tilde{q} = \vec{0}$ and $\Delta\omega = \vec{0}$, the resulting linearized gain terms were approximately equal. Equality was be achieved for the linearized error dynamics of Observers A and B. The gains of Observer C, which differ in structure from A and B, were set such that the average of the eigenvalues of the gain matrices of its linearized error dynamics were equal to the average eigenvalue of the gain matrices of the linearized error dynamics of both Observers A and B. Given $k \in \mathcal{R}$ such that $k > 0$ then each observer was proven to be locally convergent to the plant's state and the gain equivalence described was achieved by using the following formulas

- $E = (\frac{k}{2})I^{-1}$ Observer A
- $k_p = 1$ and $k_v = k$ Observer B
- $\alpha = \frac{k}{4}g_{avg}$ and $\beta = \frac{1}{2}g_{avg}$ for Observer C

where g_{avg} is the average of the eigenvalues of I^{-1}.

To evaluate and compare differences in observer convergence we simulated a number of scenarios. For observer gains such that $k > 0$, all three observers were seen to be asymptotically stable (i.e. state estimates converged to the state of the plant). For example Figure 3.1 shows a typical case of Observer A converging to the plant's state in all six DOF. Figure 3.2 is a sample plot showing the magnitude of angular position error and angular velocity error with respect to time for all three observers. For simulations of plants with inertia tensor eigenvalues near or less than 1.0, the three observers seemed to converge in a similar fashion. However, Figure 3.2 shows Observer B displaying under-damped behavior

which slows its convergence. This behavior diminished as either the gain is increased or the inertia is lowered. Figure 3.3 shows the average of 50 trials with inertia tensor eigenvalues less than unity and, on average, you can see the similar behavior of the different velocity observers.

3.2.5 Angular Velocity Observer Conclusions

This Section reports a comparative analysis of three angular velocity observers for second-order rotational plants of the form (2.34) for which the inertia tensor is known, and the signals of angular position and torque input are available. Two very different previously reports angular velocity observers were reviewed [43, 60]. We report one novel angular velocity observer together with a proof of its local asymptotic stability. The results of a comparative numerical simulation study of the three observers is reported. The observers were seen to provide similar performance over a range of inertia tensors, angular position profiles, and feedback gains. For the range of inertia tensors used, each of the three observers were analytically guaranteed to converge to the correct angular velocity estimate. However, these analytic stability analyses do not provide information on the rate of convergence. Each simulated observer's angular velocity estimate converged to the plant state as expected; however, the coordinate free and body-frame observers (though more complex to implement) were not seen to display the underdamped behavior which appeared to degrade the world-frame observer's state estimate convergence rate for some of the simulated

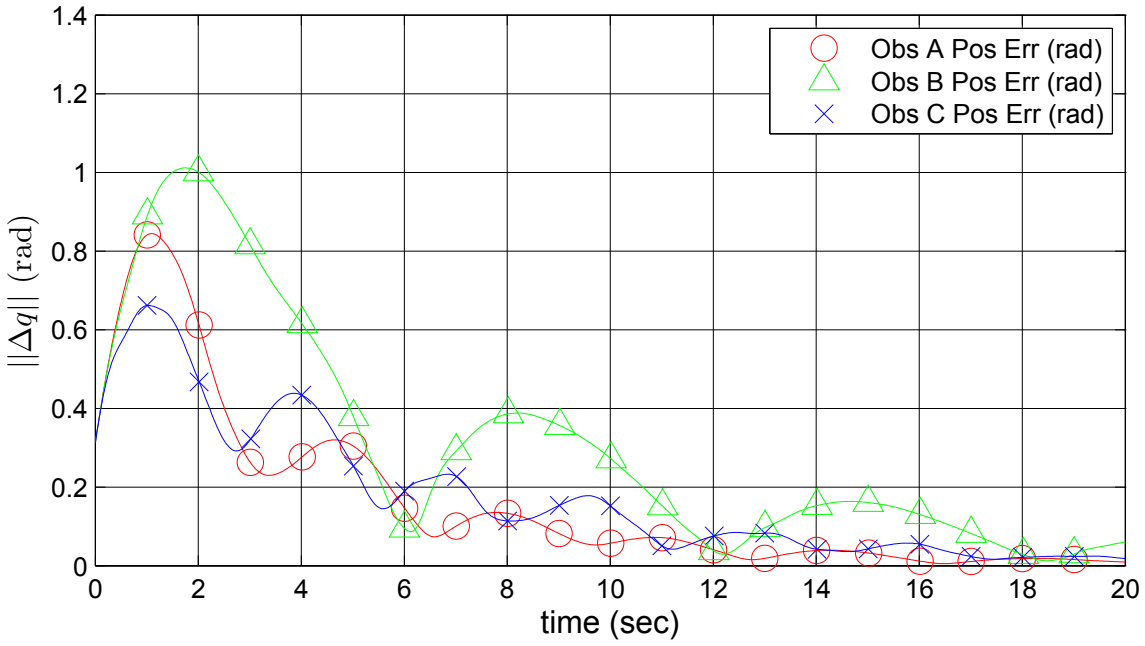

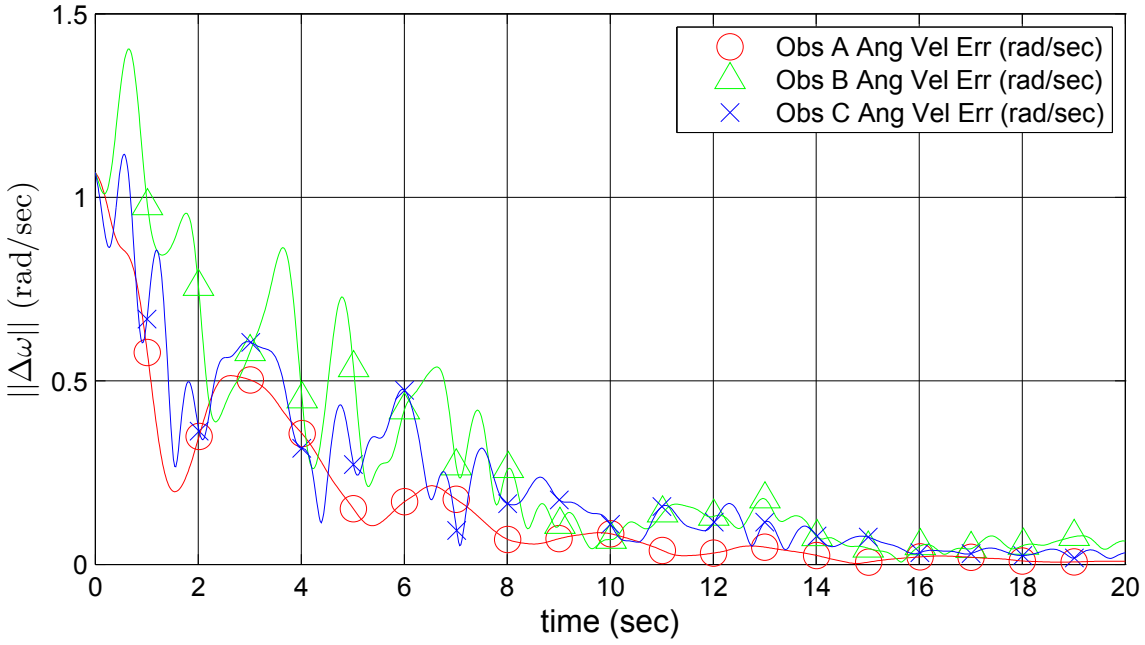

Figure 3.2: Rotational error magnitude and angular velocity error magnitude between observer state and plant state.

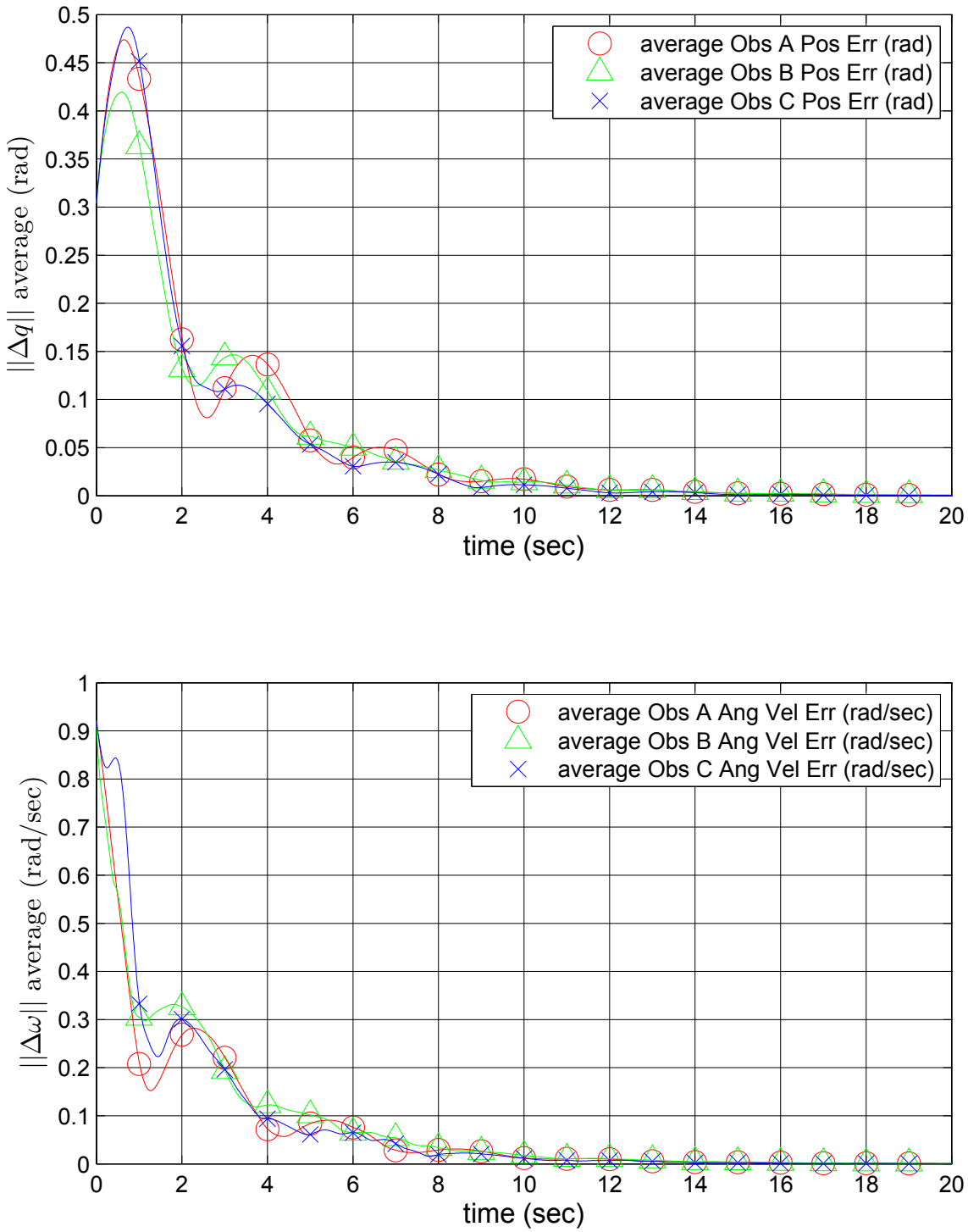

Figure 3.3: Average rotational error magnitude and average angular velocity error magnitude between observer state and plant state of an ensemble of 50 randomized angular position profile trials and inertia tensor eigenvalues less than one.

comparisons in our ensemble of simulation studies. For simple second-order linear systems, underdamped behavior results from a poorly tuned combination of the proportional and derivative gains; we would expect similar performance for each of the three observers when state errors are small enough that the linearization assumptions used to match the gains are valid. The lack of underdamped behavior in the coordinate free and body-frame observers could indicate that the additional nonlinear terms improve performance of both when the linearization assumptions are no longer valid. However, the difference in structure of these three nonlinear observers makes it difficult to analytically prove the existence of such benefits. Exploring these differences, as well as any link between the extra coordinate free and body-frame terms, is a topic for further research.

3.3 Adaptive Identification for 3-DOF Rotational Plants

This Section addresses the problem of estimation the inertia tensor of 3-DOF rotational plants of the form (2.34). We report a novel AID algorithm which estimates the inertia tensor for a rotating rigid-body using the signals of external torque and angular velocity. A local stability proof of the new AID algorithm is reported. A numerical simulation study investigates the effect of richness of the torque input signal on parameter estimation, the effect of feedback gains, the effect of initial condition, and the domain of stability. The simulation studies corroborate the analytic stability analysis, showing that the angular

velocity estimate converges asymptotically to the actual angular velocity of the plant and the adaptive estimate of the inertia tensor converges to a constant value. Additionally, the simulation studies show that the inertia tensor estimate converges to the true plant inertia tensor value in the presence of a sufficiently rich input torque signal. The simulation studies reveal the actual domain of attraction to exceed the conservative bounds arising in the stability proof, and identify practically useful ranges of feedback gains.

3.3.1 3-DOF Rotational Dynamics AID

Consider a rotating rigid-body under the influence of an external torque of the form (2.34) where the plant's input torque $\tau(t)$, angular position $R(t)$, and angular velocity $\omega(t)$ are accessible signals and the plant's PDS inertia tensor is assumed constant but is unknown. We consider the class of inputs $\tau(t)$ such that both $\tau(t)$ and the angular velocity of the uncontrolled plant, $\omega(t)$, are bounded. Throughout this Section we will use the following error signals

$$\Delta\omega(t) = \hat{\omega}(t) - \omega(t) \tag{3.25}$$

$$\Delta I(t) = \hat{I}(t) - I. \tag{3.26}$$

In this Section we will omit explicit notation of variable dependence on time except where such dependence is required to discuss the initial condition of the AID algorithm.

Theorem 3.3.1 *Consider the following AID algorithm for plants of the form (2.34)*

$$\dot{\hat{\omega}} = \hat{I}^{-1}\mathcal{J}(\hat{I}\omega)\omega - a\Delta\omega + \hat{I}^{-1}\tau \tag{3.27}$$

$$\dot{\hat{I}} = -\frac{1}{2}\left(\psi_1\omega^T + \omega\psi_1^T - \Delta\omega\psi_2^T - \psi_2\Delta\omega^T\right) \tag{3.28}$$

where $a \in \mathbb{R}_+$, $\psi_1 = \mathcal{J}(\omega)\Delta\omega$, *and* $\psi_2 = \hat{I}^{-1}\left(\mathcal{J}\left(\hat{I}\omega\right)\omega + \tau\right)$ *with the following assumptions:*

- $\tau(t)$ *and* $\omega(t)$ *are bounded*
- $\hat{I}(t_0)$ *is PDS*
- $\hat{\omega}(t_0) = \omega(t_0)$
- $\exists\epsilon \in \mathbb{R}_+$ *such that* $\|\Delta I(t_0)\|_F + \epsilon \leq \lambda_3$

Under these conditions $\lim_{t\to\infty}\Delta\omega = \vec{0}$, *i.e. the estimated angular velocity is asymptotically stable in the sense of Lyapunov, and* $\lim_{t\to\infty}\Delta\dot{I} = 0_{3\times3}$, *i.e. the estimated inertia tensor will converge to a constant value. These limits imply that the plant estimate converges to values that provide input/output behavior identical to that of the actual experimental plant for the given input torque* $\tau(t)$.

Note that since the initial parameter estimate is PDS and the parameter estimate law is symmetric, both $\hat{I}(t)$ and $\Delta I(t)$ will be symmetric $\forall t > t_0$, and thus will have strictly real eigenvalues.

3.3.2 Error System

The time derivative of (3.26) is

$$\begin{aligned}\dot{\Delta I} &= \dot{\hat{I}} \\ &= -\frac{1}{2}\left(\psi_1\omega^T + \omega\psi_1^T - \Delta\omega\psi_2^T - \psi_2\Delta\omega^T\right). \end{aligned} \tag{3.29}$$

We make use of the fact that $I\hat{I}^{-1} = \mathbb{I} - \Delta I\hat{I}^{-1}$, where $\mathbb{I}$ is the identity matrix, thus,

$$\begin{aligned} I\dot{\Delta\omega} =& I\left(\dot{\hat{\omega}} - \dot{\omega}\right) \\ =& - aI\Delta\omega + I\hat{I}^{-1}\mathcal{J}(\hat{I}\omega)\omega + I\hat{I}^{-1}\tau - \mathcal{J}(I\omega)\omega - \tau \\ =& - aI\Delta\omega + \left(\mathbb{I} - \Delta I\hat{I}^{-1}\right)\mathcal{J}(\hat{I}\omega)\omega - \mathcal{J}(I\omega)\omega - \Delta I\hat{I}^{-1}\tau \\ =& - aI\Delta\omega - \mathcal{J}(\omega)\Delta I\omega - \Delta I\hat{I}^{-1}\left(\mathcal{J}(\hat{I}\omega)\omega + \tau\right) \\ =& - aI\Delta\omega - \mathcal{J}(\omega)\Delta I\omega - \Delta I\psi_2. \end{aligned} \tag{3.30}$$

3.3.3 Stability Proof

Consider the following Lyapunov function candidate

$$V(t) = \frac{1}{2}\left(\Delta\omega^T I\Delta\omega + \mathrm{tr}\left(\Delta I\Delta I^T\right)\right). \tag{3.31}$$

$V(t)$ is positive definite and equal to zero if and only if $\Delta\omega = \vec{0}$ and $\Delta I = 0_{3\times 3}$. From (3.30) and the fact that for any matrices A and B of appropriate dimension, $\mathrm{tr}(AB) =$

$\mathrm{tr}(BA)$, the time derivative of (3.31) is

$$\begin{aligned}
\dot{V}(t) =& \frac{1}{2}\left(\dot{\Delta\omega}^T I\Delta\omega + \Delta\omega^T I\dot{\Delta\omega} + \mathrm{tr}\left(2\Delta I\dot{\Delta I}^T\right)\right) \\
=& -a\Delta\omega^T I\Delta\omega + \frac{1}{2}\left(\omega^T\Delta I\mathcal{J}(\omega)\Delta\omega\right) + \mathrm{tr}\left(\Delta I\dot{\Delta I}^T\right) \\
&+ \frac{1}{2}\left(-\psi_2^T\Delta I\Delta\omega - \Delta\omega^T\mathcal{J}(\omega)\Delta I\omega - \Delta\omega^T\Delta I\psi_2\right) \\
=& -a\Delta\omega^T I\Delta\omega + \mathrm{tr}\left(\Delta I\dot{\Delta I}^T\right) + \frac{1}{2}\left(\omega^T\Delta I\psi_1 + \psi_1^T\Delta I\omega - \psi_2^T\Delta I\Delta\omega - \Delta\omega^T\Delta I\psi_2\right) \\
=& -a\Delta\omega^T I\Delta\omega + \mathrm{tr}\left(\Delta I\dot{\Delta I}^T\right) + \frac{1}{2}\mathrm{tr}\left(\Delta I\left(\psi_1\omega^T + \omega\psi_1^T - \Delta\omega\psi_2^T - \psi_2\Delta\omega^T\right)\right).
\end{aligned} \tag{3.32}$$

Using the update law (3.28) results in

$$\dot{V}(t) = -a\Delta\omega^T I\Delta\omega, \tag{3.33}$$

which is negative definite in $\Delta\omega$ and negative semidefinite in the error coordinates $\Delta\omega$ and ΔI. Lyapunov's theorem and (3.31) - (3.33) imply that $\Delta\omega$ and ΔI are bounded and stable. The structure of $\dot{V}(t)$ implies that $\Delta\omega \in \mathcal{L}_2$ or, equivalently, $\lim_{t\to\infty}\left(\int_0^t \Delta\omega^T\Delta\omega\right)^{1/2} < \infty$. To ensure all the signals in (3.27) are bounded, we must ensure that both $\hat{I}(t)$ and $\hat{I}^{-1}(t)$ remain bounded. The facts $0 \le V(t) \le V(t_0)$, $\Delta\omega(t_0) = \vec{0}$, $\Delta\omega^T(t)I\Delta\omega(t) \ge 0$ for all t, and $\mathrm{tr}\left(\Delta I(t)\Delta I^T(t)\right) = \sum_{i=1}^3 |\Delta\lambda_i(t)|^2 = \|\Delta I(t)\|_F^2$ imply that the following inequality holds for all time:

$$\|\Delta I(t)\|_F \le \|\Delta I(t_o)\|_F. \tag{3.34}$$

By the Rayleigh-Ritz Theorem, $\min_{\|x\|=1} x^T\hat{I}(t)x = \hat{\lambda}_3(t)$. Additionally since $\hat{I}(t) =$

$I + \Delta I(t)$ and by assumption $\|\Delta I(t_0)\|_F + \epsilon \leq \lambda_3$ the following inequalities hold

$$\begin{aligned}
\hat{\lambda}_3(t) &= \min_{\|x\|=1} \left(x^T I x + x^T \Delta I(t) x \right) \\
&\geq \min_{\|x\|=1} \left(x^T I x \right) - \max_{\|x\|=1} |x^T \Delta I(t) x| \\
&\geq \lambda_3 - \|\Delta I(t)\|_2 \\
&\geq \lambda_3 - \left(\sum_{i=1}^{3} |\Delta\lambda_i(t)|^2 \right)^{1/2} \\
&\geq \lambda_3 - \|\Delta I(t)\|_F \\
&\geq \lambda_3 - \|\Delta I(t_0)\|_F \\
&\geq \lambda_3 - (\lambda_3 - \epsilon) \\
&\geq \epsilon
\end{aligned} \tag{3.35}$$

where ϵ is a finite positive scalar and we use the fact that $\|\Delta I(t)\|_2^2 = \max(|\Delta\lambda_1(t)|^2, |\Delta\lambda_3(t)|^2)$ because the singular values of a symmetric matrix are equal to the absolute values of its eigenvalues. The above inequality guarantees that all eigenvalues of $\hat{I}(t)$ are positive and bounded away from zero for all time. Similarly,

$$\begin{aligned}
\hat{\lambda}_1(t) &= \max_{\|x\|=1} \left(x^T I x + x^T \Delta I(t) x \right) \\
&\leq \lambda_1 + \max_{\|x\|=1} | \left(x^T \Delta I(t) x \right) | \\
&\leq \lambda_1 + \left(\sum_{i=1}^{3} |\Delta\lambda_i(t)|^2 \right)^{1/2} \\
&\leq \lambda_1 + \lambda_3 - \epsilon
\end{aligned} \tag{3.36}$$

which implies that the eigenvalues of $\hat{I}(t)$ are positive and bounded above for all time since

$\epsilon < \lambda_3$. Since the input τ and plant state ω are bounded by assumption, bounded $\Delta\omega$, $\hat{I}$, and $\hat{I}^{-1}$ imply that $\dot{\omega}$ and $\dot{\hat{\omega}}$ are bounded. The bounded angular velocities imply $\Delta\dot{\omega}$ is bounded. Note that bounded $\Delta\dot{\omega}$ and $\Delta\omega \in \mathcal{L}_2$ implies

$$\lim_{t\to\infty} \Delta\omega = \vec{0}. \tag{3.37}$$

Since every signal in $\dot{\hat{I}}$ is bounded and $\lim_{t\to\infty} \Delta\omega = \vec{0}$ this implies

$$\lim_{t\to\infty} \dot{\hat{I}} = 0_{3\times 3}. \tag{3.38}$$

Thus, the estimator's angular velocity asymptotically converges to the angular velocity of the actual plant, and the estimated inertial tensor, $\hat{I}$, asymptotically converges to a constant value. The local stability of the AID algorithm for 3-DOF rotational plants is proven.

3.3.4 Simulation

This Section describes the performance of the proposed AID algorithm in numerical simulation. The numerical results presented herein used a fourth order Runge-Kutta numerical solution to simulate both the AID algorithm, (3.27) and (3.28), and the plant, (2.34). Since the AID algorithm assumed access to both $\omega(t)$ and $\tau(t)$, without loss of generality we choose $\hat{\omega}(t_0) = \omega(t_0)$. The input torque $\tau(t)$ was generated as a sum of sines and cosines, each with different frequencies and amplitudes. In each trial the plant's inertia tensor, I, was chosen and the inertia tensor estimate was initialized to the identity matrix, i.e. $\hat{I}(t_0) = \mathbb{I}$.

3.3.4.1 Convergence of State and Parameter Estimates

To test the differences in identification performance we explored the effects of factors including initial parameter error, input torque richness, and feedback gain. Figure 3.4 is representative of simulated performance in the majority of cases. This representative simulation study used a feedback gain $a = 1$; an input torque of

$$\tau(t) = \begin{bmatrix} -2\cos(2t) & -2\sin(t) & 2cos(t) \end{bmatrix}^T; \tag{3.39}$$

an inertia tensor of $I = 1.5\mathbb{I}$; and an estimate of $\hat{I}(t_0) = \mathbb{I}$ (this was the initial inertia tensor for every simulation study in this Section). This Figure explicitly shows state and parameter convergence of the angular velocity and inertia tensor eigenvalue estimates. The eigenvalues of the PDS inertia tensors are plotted to show parameter convergence.

3.3.4.2 Effect of Scalar feedback Gain Parameter a

Figure 3.5 shows how AID algorithm performance varies with changes of the scalar gain a. In the case that a is large, the angular velocity error remains small for all time, and the small angular velocity error limits the ability of this error signal to drive parameter adaptation as seen in (3.28). For the case of very small values of a, the parameter convergence is slow. In the limiting case of $a = 0$ the identifier is stable, but not asymptotically stable.

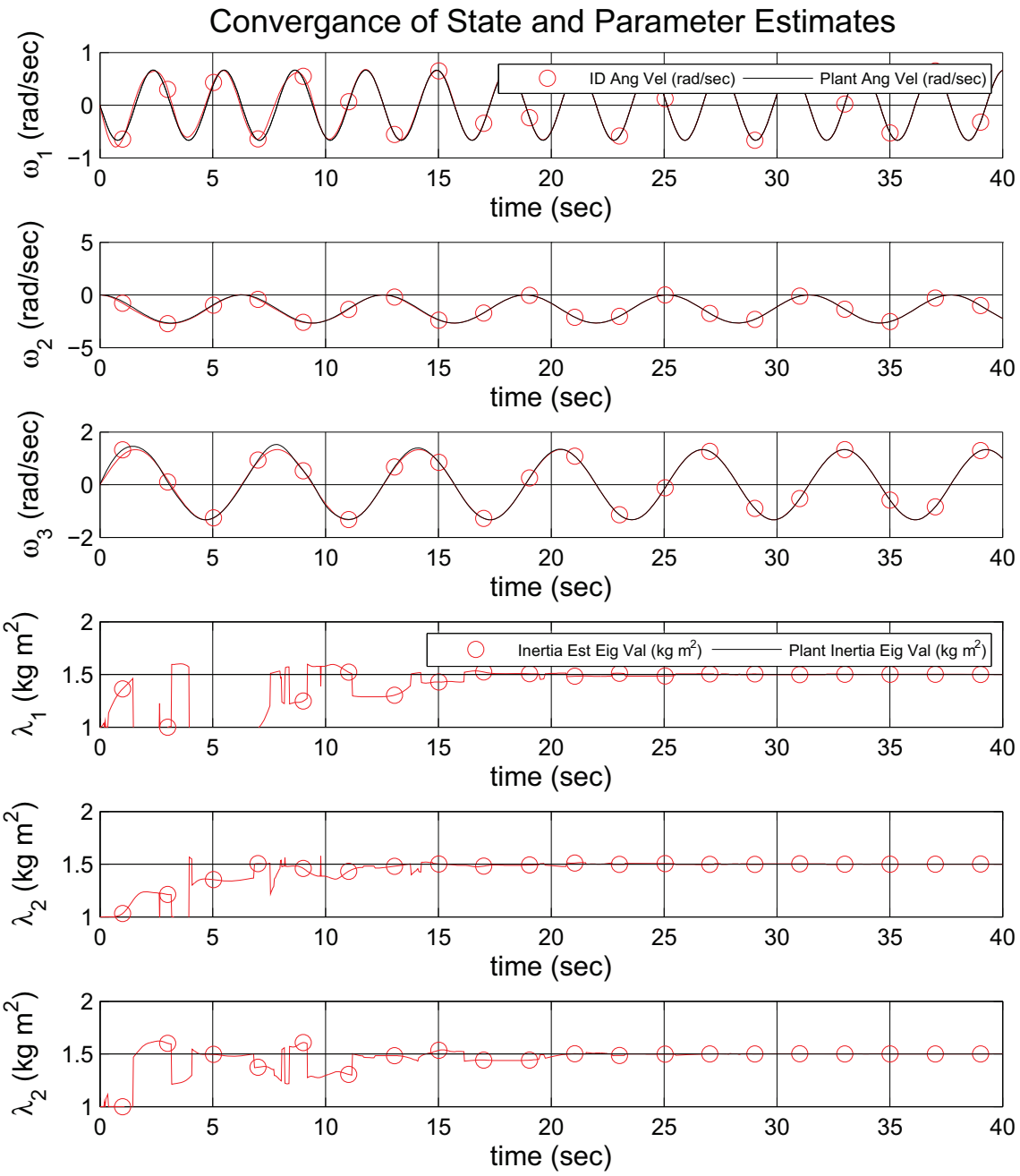

Figure 3.4: Data showing state and parameter convergence during a representative simulation study. Estimated values are highlighted with circles. The top three plots show the estimated angular velocity's convergence to the true plant angular velocity in each DOF. The bottom three plots show the eigenvalues of the estimated inertia tensor converging the true inertia tensor eigenvalues.

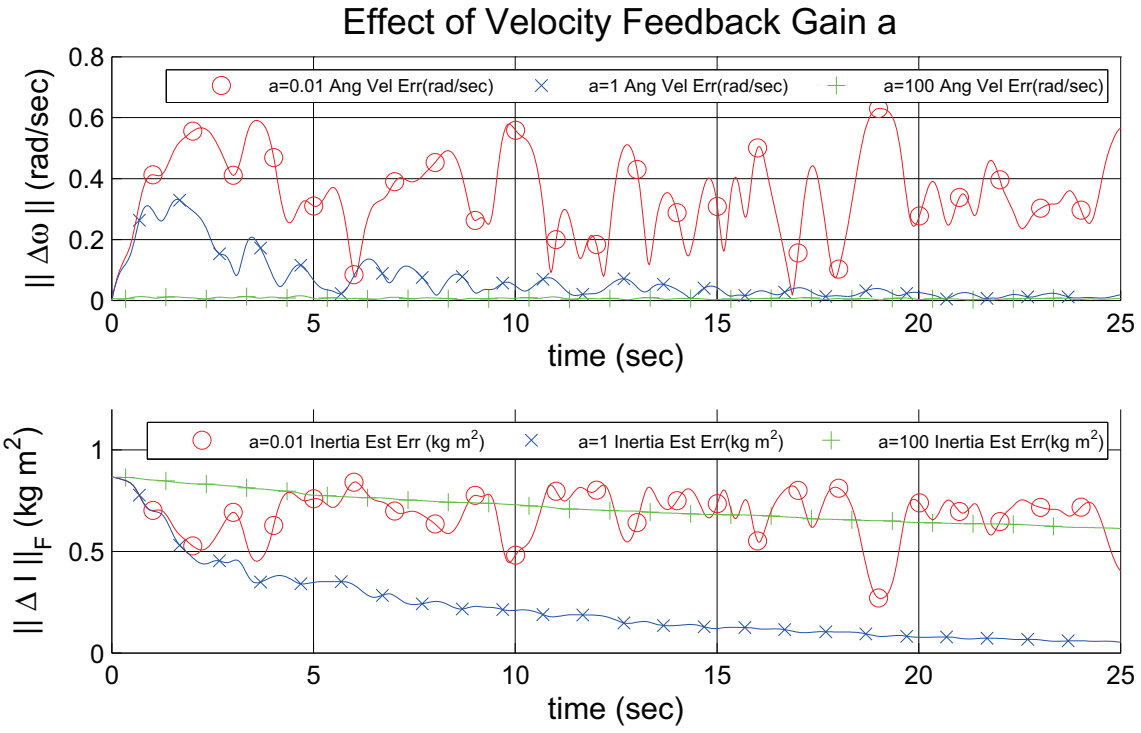

Figure 3.5: The effect of the feedback gain, a, on angular velocity and parameter convergence. The upper graph plots the norm of the body angular velocity error versus time. The lower graph plots the Frobenius norm of the inertia tensor error versus time. The cases of AID for $a = 0.01$, $a = 1.0$, and $a = 100$ are shown. Parameter convergence deteriorates for very large and very small gains.

3.3.4.3 Effect of Input $\tau(t)$ Richness

Figure 3.6 demonstrates the well know fact that exact parameter identification requires a sufficiently rich input torque signal. For these simulations we employed the following values for the identification algorithm: $a = 1$, $I = 1.5\mathbb{I}$, $\hat{I}(t_0) = \mathbb{I}$, and either $\tau(t) = \begin{bmatrix} -2\cos(2t) & -2\sin(t) & 2\cos(t) \end{bmatrix}^T$ or $\tau(t) = \begin{bmatrix} 0 & -2\sin(t) & 0 \end{bmatrix}^T$. In both cases the estimated angular velocity converged to the true angular velocity. For the case of the richer input signal, the inertia tensor estimate converged to the actual plant inertia tensor value. For the case of the simple input signal, however, the inertia tensor estimate converged to a value different from the plant's inertia tensor value. Note that the inertia tensor estimate still converged to a value that results in identical input-output behavior of the *estimated plant* and actual plant for this simple input signal (where an *estimated plant* is a second-order rotational plant of the form (2.34) with its inertia tensor equal to an inertia tensor estimate).

3.3.4.4 Effect of $\hat{I}(t_0)$

This Section examines the effect of initial parameter estimate error, $\Delta I(t_0)$, on parameter convergence. Figure 3.7 shows parameter convergence for 30 simulated initial conditions. In all cases $\hat{I}(t_0) = \mathbb{I}$ and $a = 1$. In each case $\tau(t)$ was generated from sums of sinusoids of different frequencies with randomly generated amplitudes. Three sets of ten inertia tensors were used. Every inertia tensor was randomly generated such that it was a

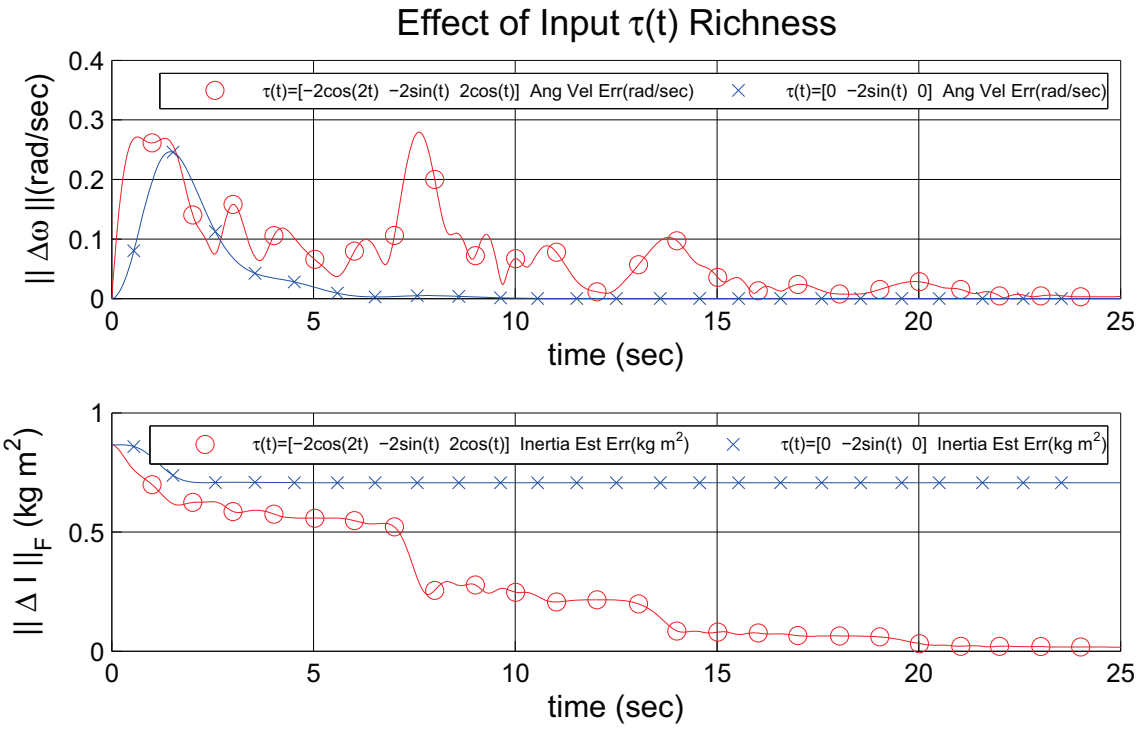

Figure 3.6: Two plots showing that parameter convergence requires a sufficiently rich input signal. The upper graph plots the norm of the body angular velocity error versus time for two inputs $\tau(t)$. The lower graph plots the Frobenius norm of the inertia tensor error versus time for both cases. The angular velocity estimate converges in either case. $\tau(t) = [0 \quad -2\sin(t) \quad 0]$ is not rich enough to force parameter convergence for this initial condition, whereas parameter convergence occurs for input torque $\tau(t) = [-2\cos(2t) \quad -2\sin(t) \quad 2\cos(t)]$.

non-diagonal PDS matrix with the eigenvalues greater than 0.5. Within each set the Frobenius norm of $\|\Delta I(t_0)\|_F$ was either 0.15, 0.5, or 1. Figure 3.7 plots parameter convergence of the AID algorithm to every inertia tensor in each of the three sets. For sets one and two, with $\|\Delta I(t_0)\|_F = 0.15$ and $\|\Delta I(t_0)\|_F = 0.5$, all conditions of Theorem 3.3.1 were met. For set three, often $\|\Delta I(t_0)\|_F > \lambda_3$ and thus the conditions of Theorem 3.3.1 were not met. Despite this, every inertia tensor estimate converged to the true inertia tensor for each randomly generated initial condition. This convergence corroborates our analytic result and indicates that the condition requiring $\|\Delta I(t_0)\|_F < \lambda_3$ from Theorem 3.3.1 is sufficient but not necessary for asymptotic convergence.

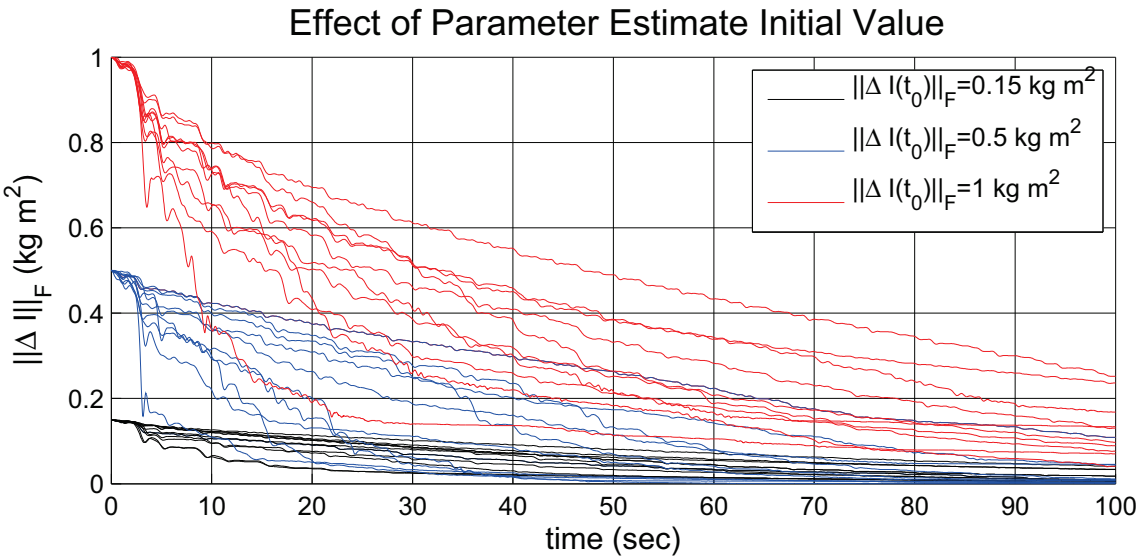

Figure 3.7: Three sets of ten simulations showing parameter convergence. The Frobenius norm of the inertia tensor error is plotted versus time. Each of the simulations used a randomly selected inertia tensor for the system, but within each set the Frobenius norm of the initial inertia error was a constant value for the entire set, either 0.15, 0.5, or 1.

3.3.5 3-DOF Rotational Plant AID Conclusion

This Section reports an AID algorithm for the dynamic estimation of the inertia tensor of rotating plants. The proof of Theorem 3.3.1 shows the local asymptotic stability of the estimated angular velocity to the plant's angular velocity and the local stability of the estimated inertia tensor. Numerical simulations show that for a sufficiently rich external torque signal the inertia tensor estimate value converges to the true inertia tensor value, and the domain of attraction of Theorem 3.3.1 is conservative. In Chapter 4, Theorems 4.2.1 and 4.3.1 extend this result to plant models of UV dynamics.

3.4 Adaptive Identification for Open Kinematic Chains

This Section addresses the problem of parameter estimation for an *n*-link open kinematic chain (OKC) of the form of (2.50). We report a novel AID algorithm which estimates these plant parameters. This algorithm assumes the joint torque inputs, τ, joint positions, q, and joint velocities, $\dot{q}$, are accessible signals.

3.4.1 OKC State Error Coordinates

The AID algorithm presented herein uses the joint velocity estimate $v \in \mathbb{R}^n$ and the parameter vector estimate $\hat{\theta}_{OKC} \in \mathbb{R}^r$ as its state variables. Let $\mathfrak{J} \subset \mathbb{R}^n$ be the OKC's joint

space and note estimated plant terms $\hat{M}$, $\hat{C}$, and $\hat{\mathfrak{g}}$ can be factored as

$$\hat{M}(a)b + \hat{C}(a,c)d + \hat{\mathfrak{g}}(a) = \mathbb{W}_{OKC}(b,a,c,d)\hat{\theta}_{OKC} \tag{3.40}$$

for all $a, b, c, d \in \mathbb{R}^n$ where $\mathbb{W}_{OKC} : \mathbb{R}^n \times \mathfrak{J} \times \mathbb{R}^n \times \mathbb{R}^n \to \mathbb{R}^{n \times r}$ is often termed the *regressor*. We employ the following joint velocity and inertia tensor error coordinates

$$\Delta v = v(t) - \dot{q}(t) \tag{3.41}$$

$$\Delta\theta_{OKC} = \hat{\theta}_{OKC}(t) - \theta_{OKC}. \tag{3.42}$$

Our goal is to develop an update law for v and $\hat{\theta}_{OKC}$ which, for initial values of $\hat{\theta}_{OKC}(t_0)$ in the neighborhood of θ_{OKC}, guarantees that $\lim_{t\to\infty} \Delta v = \vec{0}$ and $\lim_{t\to\infty} \Delta\dot{\theta}_{OKC} = \vec{0}$. Considering torque as the system input and joint velocity as the system output, the two limits above imply the input-output behavior of the estimator asymptotically converges to the input-output behavior of the plant.

3.4.2 Adaptive Identifier Description

Theorem 3.4.1 *Consider the following AID algorithm for plants of the form (2.50):*

$$\dot{v} = \hat{M}^{-1}(q)\left(\tau - \hat{C}(q,\dot{q})v - \hat{\mathfrak{g}}(q) - K\Delta v\right) \tag{3.43}$$

$$\dot{\hat{\theta}}_{OKC} = \mathbb{W}_{OKC}(\dot{v}, q, \dot{q}, v)^T \Delta v, \tag{3.44}$$

where $K \in \mathbb{R}^{n\times n}$ is PDS, with the following assumptions:

- *τ, q and $\dot{q}$ are bounded by assumption*

- $v(t_0) = \dot{q}(t_0)$

- $\exists \epsilon \in \mathbb{R}_+$ *such that*

$$\|\Delta\theta_{OKC}(t_0)\|_2 \leq \frac{1}{\sqrt{a_M r}} (\lambda_m - \epsilon) \tag{3.45}$$

where λ_m is the smallest eigenvalue for $M(q)$ in any configuration and

$$a_M = \max_{\hat{\theta} \in \{e_1, e_2, \ldots, e_r\}} \left(\max_{q \in \mathbb{R}^r} \left(\text{eig}(\hat{M}(q)) \right) \right) \tag{3.46}$$

where the set $\{e_i\}$ are the standard unit length basis vectors of the space $\mathbb{R}^r$ (see Section 3.4.5 for a complete development of a_M).

Under these conditions the joint velocity error will be asymptotically stable in the sense of Lyapunov, i.e., $\lim_{t\to\infty} \Delta v = \vec{0}$, and the model using the estimated parameters will be indistinguishable from the model using the true parameters for the given torque input, i.e., $\lim_{t\to\infty} \Delta\dot{\theta}_{OKC} = 0$.

3.4.3 Error System

Consider (2.50), (3.43), (2.51), and (3.42) as well as the fact that

$$\left(\mathbb{W}_{OKC}(b_1, a, c, d_1) - \mathbb{W}_{OKC}(b_2, a, c, d_2)\right) \theta_{OKC} = M(a)(b_1 - b_2) + C(a, c)(d_1 - d_2)$$

in the following equalities

$$\begin{aligned} 0 &= \tau - \tau \\ &= \mathbb{W}_{OKC}(\dot{v}, q, \dot{q}, v)\hat{\theta}_{OKC} + K\Delta v - \mathbb{W}_{OKC}(\ddot{q}, q, \dot{q}, \dot{q})\theta_{OKC} \\ &= \mathbb{W}_{OKC}(\dot{v}, q, \dot{q}, v)\Delta\theta_{OKC} + K\Delta v + \left(\mathbb{W}_{OKC}(\dot{v}, q, \dot{q}, v) - \mathbb{W}_{OKC}(\ddot{q}, q, \dot{q}, \dot{q})\right)\theta_{OKC} \\ &= \mathbb{W}_{OKC}(\dot{v}, q, \dot{q}, v)\Delta\theta_{OKC} + K\Delta v + M(q)\Delta\dot{v} + C(q, \dot{q})\Delta v. \end{aligned} \tag{3.47}$$

The final equality of (3.47) can be rewritten as

$$\Delta\dot{v} = M^{-1}(q)\left(-C(q, \dot{q})\Delta v - K\Delta v - \mathbb{W}_{OKC}(\dot{v}, q, \dot{q}, v)\Delta\theta_{OKC}\right). \tag{3.48}$$

3.4.4 Lyapunov Stability

Consider the following Lyapunov function candidate:

$$V(t) = \frac{1}{2}\Delta v^T M(q)\Delta v + \frac{1}{2}\Delta\theta_{OKC}^T\Delta\theta_{OKC}. \tag{3.49}$$

$V(t)$ is

- positive definite
- radially unbounded
- equal to zero if and only if $\Delta v = \vec{0}$ and $\Delta\theta_{OKC} = \vec{0}$.

Using (3.48) the time derivative of (3.49) is

$$\begin{aligned}\dot{V}(t) =& \Delta v^T M(q)\Delta\dot{v} + \frac{1}{2}\Delta v^T \dot{M}(q)\Delta v + \Delta\theta_{OKC}^T \Delta\dot{\theta}_{OKC} \\ =& -\Delta v^T K \Delta v + \Delta v^T \left(\frac{1}{2}\dot{M}(q) - C(q,\dot{q})\right)\Delta v \\ & - \Delta v^T \mathbb{W}_{OKC}(\Delta\dot{v}, q, \dot{q}, \Delta v)\theta_{OKC} + \Delta\theta_{OKC}^T \Delta\dot{\theta}_{OKC}\end{aligned}$$

Using the fact that $\dot{M}(q) - 2C(q,\dot{q})$ is skew symmetric and the update law (3.44) results in

$$\dot{V}(t) = -\Delta v^T K \Delta v. \tag{3.50}$$

$\dot{V}(t)$ is negative definite in Δv and negative semidefinite in the error coordinates Δv and $\Delta\theta_{OKC}$. Lyapunov's theorem and (3.49) - (3.50) imply that Δv and $\Delta\theta_{OKC}$ are bounded and stable. The structure of $\dot{V}(t)$ implies that $\Delta v \in \mathcal{L}_2$, or equivalently $\lim_{t\to\infty}\left(\int_0^t \Delta v^T \Delta v\right)^{1/2} < \infty$. To ensure all the signals in (3.43) are bounded, we must ensure that both $\hat{M}^{-1}(q)$ and $\hat{M}(q)$ remain bounded. Section 3.4.5 proves both are implied by the conditions specified in Theorem 3.4.1. Since τ, q, and $\dot{q}$ are bounded by assumption, bounded Δv, $\hat{M}(q)$, and $\hat{M}^{-1}(q)$ imply that $\dot{q}$ and $\dot{\hat{\theta}}_{OKC}$ are bounded. The bounded joint velocities imply $\Delta\dot{v}$ is bounded. Note that bounded $\Delta\dot{v}$ and $\Delta v \in \mathcal{L}_2$ implies

$$\lim_{t\to\infty} \Delta v = \vec{0}. \tag{3.51}$$

Moreover, since every signal in $\dot{\hat{\theta}}_{OKC}$ is bounded and $\lim_{t\to\infty}\Delta v = \vec{0}$ this implies

$$\lim_{t\to\infty} \dot{\hat{\theta}}_{OKC} = \vec{0}. \tag{3.52}$$

Thus the estimator's joint velocity asymptotically converges to the joint velocity of the actual plant, and the estimated plant parameters, $\hat{\theta}_{OKC}$, asymptotically converge to a constant

value.

The local stability of this OKC AID algorithm is proven if condition (3.45) is sufficient to bound the mass matrix estimate eigenvalues away from zero.

3.4.5 Bound for Estimated Inertia Matrix

The final requirement to prove Theorem 3.4.1 is that the condition $\|\Delta\theta_{OKC}(t_0)\|_2 \leq \frac{1}{\sqrt{a_M r}}(\lambda_m - \epsilon)$ implies $\hat{M}(q,t)$ and $\hat{M}^{-1}(q,t)$ are bounded for all time and all configurations. Before showing the eigenvalues of $\hat{M}(q,t)$ are bounded both above and below we need to further clarify some facts about manipulator mass matrices and define a useful vector semi-norm.

Since $M(q)$ is PDS we know its largest and smallest singular values are its largest and smallest eigenvalues. Further, we know that for any physical manipulator every eigenvalue of $M(q)$ is both positive and bounded for every joint configuration, q, in the manipulator's joint space, $\mathfrak{J}$. In the sequel, we will use the following definitions: let the constants $\lambda_m, \lambda_M \in \mathbb{R}_+$ be such that $\lambda_m = \min_{q\in\mathfrak{J}}\left(\min_{\|x\|_2=1} x^T M(q)x\right)$ and $\lambda_M = \max_{q\in\mathfrak{J}}\|M(q)\|_2$. Since $M(q)$ is assumed to be completely known up to the uncertain base parameters, θ_{OKCi}, this knowledge allows the complete specification of a set of functions $A_i : \mathbb{R}^n \to \mathbb{R}^{n\times n}$ such that

$$M(q) = \sum_{i=1}^{r} \theta_{OKCi} A_i(q). \tag{3.53}$$

Further, each $A_i(q)$ is symmetric and bounded, i.e. $\forall i \quad \exists a_i \geq 0$ such that $\|A_i(q)\|_2 \leq a_i$

$\forall q \in \mathfrak{J}$. Based on these non-negative bounding scalars we define the following vector semi-norm

$$\|b\|_a = \sum_{i=1}^{r} a_i |b_i| \tag{3.54}$$

where $b = [b_1 \ \cdots \ b_r]^T \in \mathbb{R}^r$. Note that for any two vector norms there exists a constant, p, such that $\|b\|_a \leq p\|b\|_2$ [23]. To find a conservative value for p in the case of $\| \bullet \|_a$ and $\| \bullet \|_2$ we use that $0 \leq (|b_i - b_j|)^2$ implies $2|b_i||b_j| \leq |b_i|^2 + |b_j|^2 \ \forall i, j$. Let a_M be such that $\forall i \quad a_M \geq a_i$ and consider

$$\begin{aligned}
\|b\|_a^2 &= \left(\sum_{i=1}^{r} a_i |b_i| \right)^2 \\
&= \sum_{i=1}^{r} a_i^2 |b_i|^2 + \sum_{i=1}^{r-1} \sum_{j=i+1}^{r} 2a_i a_j |b_i||b_j| \\
&\leq \sum_{i=1}^{r} a_M^2 |b_i|^2 + \sum_{i=1}^{r-1} \sum_{j=i+1}^{r} 2a_M^2 |b_i||b_j| \\
&\leq a_M \left(\sum_{i=1}^{r} |b_i|^2 + \sum_{i=1}^{r-1} \sum_{j=i+1}^{r} \left(|b_i|^2 + |b_j|^2 \right) \right) \\
&\leq a_M \left(\sum_{i=1}^{r} r |b_i|^2 \right) \\
&\leq a_M r \|b\|_2^2.
\end{aligned} \tag{3.55}$$

Since the square root is a strictly increasing function $\sqrt{a_M r}$ is a conservative value for p because the previous inequality implies

$$\|b\|_a \leq \sqrt{a_M r} \|b\|_2. \tag{3.56}$$

Now let us turn to the task of bounding $\hat{M}(q,t)$. Note that the facts $0 \leq V(t) \leq V(t_0)$, $\Delta v(t_0) = \vec{0}$, and $\Delta v^T(t) M(q) \Delta v(t) \geq 0$ for all t imply that the following inequality holds

$\forall t \geq t_0$:

$$\|\Delta\theta_{OKC}(t)\|_2 \leq \|\Delta\theta_{OKC}(t_o)\|_2. \tag{3.57}$$

By defining Rayleigh-Ritz Theorem the minimum possible eigenvalue of $\hat{M}(q,t)$ at a certain time, $\hat{\lambda}_m(t)$, is given by $\hat{\lambda}_m(t) = \min_{q\in\mathfrak{J}}\left(\min_{\|x\|=1} x^T\hat{M}(q,t)x\right)$. Defining ΔM such that $\mathbb{W}_{OKC}(a,b,c,d)\Delta\theta_{OKC} = \Delta M(b)a + \Delta C(b,c)d + \Delta\mathfrak{g}(b)$ note the implied equality of $\hat{M}(q,t) = M(q) + \Delta M(q,t)$. Consider the following,

$$\begin{aligned}
\hat{\lambda}_m &= \min_{q\in\mathfrak{J}}\left(\min_{\|x\|=1} x^T\left(M(q)+\Delta M(q,t)\right)x\right)\\
&\geq \min_{q\in\mathfrak{J}}\min_{\|x\|=1} x^TM(q)x - \max_{q\in\mathfrak{J}}\left(\max_{\|x\|=1}|x^T\Delta M(q,t)x|\right)\\
&\geq \lambda_m - \max_{q\in\mathfrak{J}}\left(\max_{\|x\|=1}|\sum_{i=1}^{r}\Delta\theta_{OKCi}(t)x^TA(q)x|\right)\\
&\geq \lambda_m - \max_{q\in\mathfrak{J}}\left(\sum_{i=1}^{r}\max_{\|x\|=1}|\Delta\theta_{OKCi}(t)||x^TA(q)x|\right)\\
&\geq \lambda_m - \sum_{i=1}^{r}|\Delta\theta_{OKCi}(t)|a_i\\
&\geq \lambda_m - \|\Delta\theta_{OKC}(t)\|_a\\
&\geq \lambda_m - \sqrt{a_Mr}\|\Delta\theta_{OKC}(t)\|_2\\
&\geq \lambda_m - \sqrt{a_Mr}\|\Delta\theta_{OKC}(t_0)\|_2\\
&\geq \lambda_m - \sqrt{a_Mr}\left(\frac{1}{\sqrt{a_Mr}}\left(\lambda_m-\epsilon\right)\right)\\
&\geq \epsilon.
\end{aligned} \tag{3.58}$$

The previous inequality shows that the condition $\exists\epsilon \in \mathbb{R}_+$ such that $\|\Delta\theta_{OKC}(t_0)\|_2 \leq$

$\frac{1}{\sqrt{a_M r}}(\lambda_m - \epsilon)$ implies that $M(q)$ is invertible for all time. Similarly,

$$\begin{aligned}
\hat{\lambda}_M &= \max_{q \in \mathfrak{J}} \left(\max_{\|x\|=1} x^T \left(M(q) + \Delta M(q,t) \right) x \right) \\
&\leq \lambda_M + \max_{q \in \mathfrak{J}} \left(\max_{\|x\|=1} |x^T \Delta M(q,t) x| \right) \\
&\leq \lambda_M + \|\Delta \theta_{OKC}(t)\|_a \\
&\leq \lambda_M + (\lambda_m - \epsilon) \qquad (3.59)
\end{aligned}$$

which implies that $\hat{M}(q,t)$ is bounded for all time since $\epsilon < \lambda_m$.

3.4.6 Open Kinematic Chain Adaptive Identification Conclusion

In this Section an AID algorithm for a robotic manipulator is reported. The AID algorithm presented herein has the advantages of being intuitive, having no requirement for joint acceleration, and providing physically feasible plant parameter estimates. However, an experimental comparison with proven linear regression techniques, such as the method proposed by Khalil et al. [31], would be required to understand the comparative performance of this adaptive identifier. We are interested in exploring AID of coupled UV OKC systems with applications to work-class remotely operated vehicle (ROV) deployments. With only a brief discussion of persistent excitation for open kinematic chain adaptive identification algorithms reported thus far [24], we feel further consideration of persistent excitation in the context of manipulator adaptive identification would clarify the compar-

ative strengths and weaknesses between adaptive identification and the more established methods.

3.5 Summary

This Chapter reports one state estimation and two parameter identification algorithms for simple simple mechanical systems (SMSs). An angular velocity observer is reported for a 3-DOF rotational plant, and a comparative analysis is reported between the novel and two previously reported nonlinear angular velocity observers. In numerical simulation all three show similar performance. An AID algorithm is reported for 3-DOF rotational plants. Numerical simulations of the inertia tensor AID algorithm corroborate the analytical stability analysis and investigate parameter convergence for varying initial conditions, feedback gains, and input torques. An AID algorithm for OKCs is also reported; the local stability analysis reveals that plant parameter estimates converge to values that provide plant model input-output behavior identical to that of the actual second-order OKC plant.

Chapter 4

Adaptive Identification for Underwater Vehicles

This Chapter addresses the problem of estimation of plant parameters for 6-degree-of-freedom (DOF) rigid-body underwater vehicles (UVs). We report two novel adaptive identification (AID) algorithms. Each algorithm estimates the parameters for a rigid-body plant such as vehicle mass with added hydrodynamic mass; quadratic drag; and gravitational and buoyancy parameters that arise in the dynamic models of rigid-body UVs. The first AID algorithm identifies parameters to model 3-DOF UV rotational plant dynamics; its development is a precursor to the second AID algorithm. The second algorithm, 6-DOF underwater vehicle (UV) adaptive identification (AID), identifies parameters to model general 6-DOF UV motion. For both AID algorithms a local stability proof is reported showing velocity signal estimates converge asymptotically to the plant velocity signals; parameter

estimates are stable; and parameter estimates converge asymptotically to values that provide input-output model behavior identical to that of the actual plant. The Johns Hopkins University Remotely Controlled Vehicle (JHU ROV) was used for comparative experimental evaluations of both AID algorithms. Sections 4.5 and 4.6 report comparisons of an adaptively identified plant model (AIDPM) and a least squares identified plant model (LSPM) in cross-validation experiments. Both models are shown to match closely the JHU ROV's experimentally observed input-output behavior.

As discussed in Section 3.1, a rich literature exists on the problem of model-based adaptive trajectory-tracking control. These approaches are not applicable when the plant is either uncontrolled, under open-loop control, or under the control of a control law other than a specific adaptive tracking controller. In contrast, the AID algorithms reported herein provide an approach to plant parameter estimation applicable to the commonly occurring cases of uncontrolled plants, plants under open-loop control, and plants using control methods prescribed to meet considerations for an application.

Unlike least squares identification (LS) approaches, which requires actuator thrust, position, velocity, and acceleration signals, AID requires only actuator thrust, position, and velocity signals. Several parameter identification methods have been reported which do not require direction instrumentation of acceleration. [24] reports an AID algorithm for open kinematic chains (OKCs) that employs a low pass filter approach to the parameter update law that does not require joint acceleration signals, and reports a numerical simulation. UV parameter identification algorithms not requiring acceleration signals have been reported

which use adaptive methods [64] or numerical differentiation [7, 57]. These reported UV algorithms, as presented, are for decoupled plants and have not been shown to generalize to the fully-coupled UV models, such as (2.40) or (2.44). To the best of our knowledge, Theorem 4.3.1 is the first reported adaptive method for parameter estimation of a fully coupled 6-DOF UV model *without* the additional need to simultaneously perform reference trajectory-tracking.

The need to dynamically estimate the rigid-body model parameters from input-output signals arises in a variety of vehicle dynamics and control problems including space and air missions, where the vehicle's mass distribution may vary as fuel or payload are expended over the duration of a mission. The issues of parameter identification are also important for UVs; in comparison to rigid-body 6-DOF spacecraft models (where characterizing vehicle inertia can require 10 scalar values), the effects of added mass, gravity, buoyancy, and drag require additional parameter and model complexity to characterize UV dynamics (full characterization of these effects during dynamic UV operation can require hundreds of scalar parameter values). In addition, for most UVs the drag parameters and mass parameters (which include both the characteristics of the vehicle's mass and those of the ambient fluid surrounding the vehicle) cannot be computed analytically, and thus must be identified experimentally.

The solution to the identification problem reported herein may prove useful in applications with controlled or uncontrolled plants in which reference trajectory-tracking is impractical or infeasible. Of particular interest to the authors are two use case applications

common in our UV field deployments. The first is the case of vehicles for which the user does not have the ability to specify an adaptive tracking control algorithm. This can be the case with commercially available vehicles because often the user can not replace the controller provided by the vehicle's manufacturer. The second is the case of under-actuated vehicles. Adaptive tracking controllers require actuation in all DOF. Frequently vehicle designers utilize UV passive stability of pitch and roll in the design of under-actuated vehicles, making adaptive tracking control not applicable for either control or model identification. In these examples, the ability to estimate continuously the plant model parameters from available input-output signals may enable improved model-based control. Continuous parameter monitoring may also enable the detection of unexpected changes that indicate system failures.

The UV rotational dynamics AID algorithm and its experimental evaluation were originally reported in 2012 [47]. The UV AID algorithm and its experimental evaluation were originally reported in 2013 [48].

4.1 Problem Statements

In this Chapter we report two parameter AID algorithms, one for 3-DOF UV rotational dynamics, and the other for 6-DOF UV dynamics. In both cases the AID algorithm estimates the plant parameters using the UV state and control input signals. In these problem statements, the torque and force signals are the plant inputs and the velocity signals are

the plant outputs. The AID convergence proofs imply the input-output behavior of the estimator converges asymptotically to the input-output behavior of the plant. Below are the precise problem statements for the two AID algorithms.

3-DOF UV Rotational Dynamics AID Problem Statement: Using the notation defined in Section 2.5.2 to model a UV subjected to external torques with (2.40), the AID algorithm reported in Section 4.2 addresses plants where $R(t)$, $\omega(t)$, and $\tau(t)$ are accessible signals and the parameters $\{I,\ C_1,\ C_2,\ C_3,\ b\}$ are constant but unknown. This AID algorithm addresses the class of inputs $\tau(t)$ such that the input torque and output velocity signals of the uncontrolled plant ($\tau(t)$ and $\omega(t)$) are bounded. The algorithm uses an angular velocity estimate $\hat{\omega}(t) \in \mathbb{R}^3$, inertia tensor estimate $\hat{I}(t) \in \mathbb{R}^{3\times3}$, quadratic drag estimates $\hat{C}_i(t) \in \mathbb{R}^{3\times3}$, and buoyancy torque estimate $\hat{b}(t) \in \mathbb{R}^3$ as state variables. Defining the error coordinates

$$\Delta\omega(t) = \hat{\omega}(t) - \omega(t) \tag{4.1}$$

$$\Delta I(t) = \hat{I}(t) - I \tag{4.2}$$

$$\Delta C_i(t) = \hat{C}_i(t) - C_i \tag{4.3}$$

$$\Delta b(t) = \hat{b}(t) - b \tag{4.4}$$

the goal is to develop update laws for $\hat{\omega}(t)$, $\hat{I}(t)$, $\hat{C}_i(t)$, and $\hat{b}(t)$ which, for initial parameter values in the neighborhood of their respective true values, guarantee that $\lim_{t\to\infty} \Delta\omega(t) =$

$\vec{0}$, $\lim_{t\to\infty} \dot{\hat{I}}(t) = 0_{3\times3}$, $\lim_{t\to\infty} \dot{\hat{C}}_i(t) = 0_{3\times3}$, and $\lim_{t\to\infty} \dot{\hat{b}}(t) = \vec{0}$.

6-DOF UV AID Problem Statement: Using the notation defined in Section 2.6 to model a UV subjected to external forces and torques with (2.44), the AID algorithm reported in Section 4.3 addresses plants where $R(t)$, $v(t)$, and $u(t)$ are accessible signals and the parameters $\{M,\ D_i \text{ for } i = 1\cdots6,\ g,\ b\}$ are constant but unknown. This AID algorithm addresses the class of inputs $u(t)$ such that the input and output signals of the uncontrolled plant are bounded (i.e. $u(t)$ and $v(t)$, or equivalently $f(t)$, $\tau(t)$ and $\nu(t)$, $\omega(t)$, are bounded). The algorithm uses a vehicle velocity estimate $\hat{v}(t) \in \mathbb{R}^3$, hydrodynamic mass matrix estimate $\hat{M}(t) \in \mathbb{R}^{6\times6}$, quadratic drag estimates $\hat{D}_i(t) \in \mathbb{R}^{6\times6}$, gravitational constant estimate $\hat{g}(t) \in \mathbb{R}$, and buoyancy torque estimate $\hat{b}(t) \in \mathbb{R}^3$ as state variables. Defining the error coordinates

$$\Delta v(t) = \hat{v}(t) - v(t) \tag{4.5}$$

$$\Delta M(t) = \hat{M}(t) - M \tag{4.6}$$

$$\Delta D_i(t) = \hat{D}_i(t) - D_i \tag{4.7}$$

$$\Delta g(t) = \hat{g}(t) - g \tag{4.8}$$

$$\Delta b(t) = \hat{b}(t) - b \tag{4.9}$$

the goal is to develop update laws for $\hat{v}(t)$, $\hat{M}(t)$, $\hat{D}_i(t)$, $\hat{g}(t)$, and $\hat{b}(t)$ which, for initial parameter values in the neighborhood of their respective true values, guarantee that $\lim_{t\to\infty} \Delta v(t) = \vec{0}$, $\lim_{t\to\infty} \dot{\hat{M}}(t) = 0_{6\times6}$, $\lim_{t\to\infty} \dot{\hat{D}}_i(t) = 0_{6\times6}$, $\lim_{t\to\infty} \dot{\hat{g}}(t) = \vec{0}$, and $\lim_{t\to\infty} \dot{\hat{b}}(t) = \vec{0}$.

In the remainder of this Chapter we omit explicit notation of variable dependence on time except where such dependence is required to discuss the initial condition of the AID algorithms.

4.2 3-DOF UV Rotational Dynamics AID

This Section reports a novel nonlinear AID algorithm for plants of the form (2.40), a model of 3-DOF UV rotational dynamics. A local stability analysis is also included. This proof of Theorem 4.2.1 is provided in two parts. First, in Section 4.2.1, the error system is developed. Then, in Section 4.2.2, we prove the result.

Theorem 4.2.1 *Consider the following AID algorithm for plants of the form (2.40):*

$$\dot{\hat{\omega}} = \hat{I}^{-1}\left(\mathcal{J}(\hat{I}\omega)\omega + \sum_{i=1}^{3}|\omega_i|\hat{C}_i\omega + \mathcal{J}(\hat{b})R^T e_3 + \tau\right) - a\Delta\omega \tag{4.10}$$

$$\dot{\hat{I}} = -\frac{\gamma_1}{2}\left(\psi_4\omega^T + \omega\psi_4^T - \Delta\omega\psi_3^T - \psi_3\Delta\omega^T\right) \tag{4.11}$$

$$\dot{\hat{C}}_i = -\gamma_2|\omega_i|\Delta\omega\omega^T \tag{4.12}$$

$$\dot{\hat{b}} = -\gamma_3\mathcal{J}(R^T e_3)\Delta\omega \tag{4.13}$$

with the following definitions:

- $a, \gamma_1, \gamma_2, \gamma_3 \in \mathbb{R}_+$,
- $\psi_4 = \mathcal{J}(\omega)\Delta\omega$,
- $\psi_3 = \hat{I}^{-1}\left(\mathcal{J}(\hat{I}\omega)\omega + \sum_{i=1}^{3}|\omega_i|\hat{C}_i\omega + \mathcal{J}(\hat{b})R^T e_3 + \tau\right)$

and the following assumptions:

- $\tau(t)$ *is bounded by assumption*

- $\hat{I}(t_0)$ *is positive definite symmetric (PDS)*

- $\hat{\omega}(t_0) = \omega(t_0)$

- $\exists \epsilon \in \mathbb{R}_+$ *such that* $\lambda_3 \geq \left(\|\Delta I(t_0)\|_F^2 + \frac{\gamma_1}{\gamma_2} \sum_{i=1}^{3} \|\Delta C_i(t_0)\|_F^2 + \frac{\gamma_1}{\gamma_3} \|\Delta b(t_0)\|_2^2 \right)^{1/2} + \epsilon$.

Under these conditions the estimated angular velocity error will be asymptotically stable in the sense of Lyapunov, i.e., $\lim_{t\to\infty} \Delta\omega = \vec{0}$*, and parameter estimates converge to constant values.*

This local stability result implies that the plant parameter estimates converge to values that provide plant model input/output behavior identical to that of the actual experimental plant for the given input torque $\tau(t)$.

4.2.1 UV Rotational Dynamics AID Error System

Note that (4.2) implies $I\hat{I}^{-1} = \mathbb{I} - \Delta I\hat{I}^{-1}$ and consider the following expression for the angular velocity error dynamics

$$\begin{aligned}
I\Delta\dot{\omega} =& I\hat{I}^{-1}\left(\mathcal{J}\left(\hat{I}\omega\right)\omega + \sum_{i=1}^{3}|\omega_i|\hat{C}_i\omega + \mathcal{J}\left(\hat{b}\right)R^T e_3 + \tau\right) - aI\Delta\omega \\
&- \mathcal{J}\left(I\omega\right)\omega - \sum_{i=1}^{3}|\omega_i|C_i\omega - \mathcal{J}\left(b\right)R^T e_3 - \tau \\
=& - aI\Delta\omega - \mathcal{J}\left(\omega\right)\Delta I\omega - \Delta I\hat{I}^{-1}\left(\mathcal{J}\left(\hat{I}\omega\right)\omega + \tau\right) \\
&+ \left(\mathbb{I} - \Delta I\hat{I}^{-1}\right)\left(\sum_{i=1}^{3}|\omega_i|\hat{C}_i\omega\right) - \left(\sum_{i=1}^{3}|\omega_i|C_i\omega\right) \\
&+ \left(\mathbb{I} - \Delta I\hat{I}^{-1}\right)\mathcal{J}\left(\hat{b}\right)R^T e_3 - \mathcal{J}\left(b\right)R^T e_3 \\
=& - aI\Delta\omega - \mathcal{J}\left(\omega\right)\Delta I\omega + \sum_{i=1}^{3}|\omega_i|\Delta C_i\omega + \mathcal{J}\left(\Delta b\right)R^T e_3 \\
&- \Delta I\hat{I}^{-1}\left(\mathcal{J}\left(\hat{I}\omega\right)\omega + \sum_{i=1}^{3}|\omega_i|\hat{C}_i\omega + \mathcal{J}\left(\hat{b}\right)R^T e_3 + \tau\right) \\
=& - aI\Delta\omega - \mathcal{J}\left(\omega\right)\Delta I\omega + \Delta I\psi_3 + \sum_{i=1}^{3}|\omega_i|\Delta C_i\omega + \mathcal{J}\left(\Delta b\right)R^T e_3 \qquad (4.14)
\end{aligned}$$

4.2.2 UV Rotational Dynamics AID Convergence Proof

Consider the following Lyapunov function candidate

$$V(t) = \frac{1}{2}\Delta\omega^T I\Delta\omega + \frac{1}{2\gamma_1}\operatorname{tr}\left(\Delta I\Delta I^T\right) + \frac{1}{2\gamma_2}\sum_{i=1}^{3}\operatorname{tr}\left(\Delta C_i\Delta C_i^T\right) + \frac{1}{2\gamma_3}\Delta b^T\Delta b. \quad (4.15)$$

$V(t)$ is

- positive definite

- equal to zero if and only if $\Delta\omega = \vec{0}$, $\Delta I = 0_{3\times3}$, $\forall i\ \Delta C_i = 0_{3\times3}$, and $\Delta b = \vec{0}$.

From (4.14) and the facts that for any matrices A and B of appropriate dimension $\mathrm{tr}(AB) = \mathrm{tr}(BA)$ and for any $x_1, x_2, x_3 \in \mathbb{R}^3 \quad x_1^T \mathcal{J}(x_2)\, x_3 = x_2^T \mathcal{J}(x_3)\, x_1$, the time derivative of (4.15) is

$$\begin{aligned}
\dot{V}(t) =& \frac{1}{2}\left(\Delta\dot{\omega}^T I \Delta\omega + \Delta\omega^T I \Delta\dot{\omega}\right) + \frac{1}{\gamma_1}\mathrm{tr}\left(\Delta I \Delta\dot{I}^T\right) + \frac{1}{\gamma_2}\sum_{i=1}^{3}\mathrm{tr}\left(\Delta C_i \Delta\dot{C}_i^T\right) + \frac{1}{\gamma_3}\Delta b^T \Delta\dot{b} \\
=& -a\Delta\omega^T I \Delta\omega + \frac{1}{2}\left(\omega^T \Delta I \mathcal{J}(\omega)\,\Delta\omega - \Delta\omega^T \mathcal{J}(\omega)\,\Delta I\omega - \psi_3^T \Delta I \Delta\omega - \Delta\omega^T \Delta I \psi_3\right) \\
&+ \frac{1}{\gamma_1}\mathrm{tr}\left(\Delta I \Delta\dot{I}^T\right) + \Delta\omega^T\left(\sum_{i=1}^{3}|\omega_i|\Delta C_i\right)\omega + \frac{1}{\gamma_2}\sum_{i=1}^{3}\mathrm{tr}\left(\Delta C_i \Delta\dot{C}_i^T\right) \\
&+ \Delta\omega^T \mathcal{J}(\Delta b)\, R^T e_3 + \frac{1}{\gamma_3}\Delta b^T \Delta\dot{b} \\
=& -a\Delta\omega^T I \Delta\omega + \frac{1}{2}\mathrm{tr}\left(\Delta I\left(\mathcal{J}(\omega)\,\Delta\omega\omega^T - \omega\Delta\omega^T \mathcal{J}(\omega) - \Delta\omega\psi_3^T - \psi_3\Delta\omega^T\right)\right) \\
&+ \frac{1}{\gamma_1}\mathrm{tr}\left(\Delta I \Delta\dot{I}^T\right) + \sum_{i=1}^{3}\mathrm{tr}\left(|\omega_i|\Delta C_i \omega \Delta\omega^T\right) + \frac{1}{\gamma_2}\sum_{i=1}^{3}\mathrm{tr}\left(\Delta C_i \Delta\dot{C}_i^T\right) \\
&+ \Delta b^T \mathcal{J}\left(R^T e_3\right)\Delta\omega + \frac{1}{\gamma_3}\Delta b^T \Delta\dot{b}
\end{aligned} \tag{4.16}$$

Note the actual plant parameters are constant, thus $\Delta\dot{I} = \dot{\hat{I}}$, $\Delta\dot{C}_i = \dot{\hat{C}}_i$, and $\Delta\dot{b} = \dot{\hat{b}}$. Using the fact that $\psi_4 = \mathcal{J}(\omega)\,\Delta\omega$ and substituting (4.11)-(4.13) into (4.16) yields

$$\dot{V}(t) = -a\Delta\omega^T I \Delta\omega, \tag{4.17}$$

which is negative definite in $\Delta\omega$ and negative semi-definite in the error coordinates ΔI, ΔC_i, and Δb. By Lyapunov's direct method, (4.15) and (4.17) imply that all error coordinates are bounded and stable. The structure of $\dot{V}(t)$ implies that $\Delta\omega \in \mathcal{L}_2$ or, equivalently, $\lim_{t\to\infty}\left(\int_{t_0}^{t}\Delta\omega^T\Delta\omega\right)^{1/2} < \infty$. We must ensure every signal in (4.10)-(4.13) is bounded.

With ω, τ, $\Delta\omega$, ΔI, ΔC_i, and Δb bounded, I, C_i, and b constant, and given (4.1)-(4.4) we can conclude that $\hat{\omega}$, $\hat{I}$, $\hat{C}_i$, and $\hat{b}$ are bounded. All that remains is showing that $\hat{I}^{-1}$ is bounded. Note for $\forall t > t_0$ the following hold:

- $\frac{1}{\gamma_2}\sum_{i=1}^{3} \operatorname{tr}\left(\Delta C_i(t)\Delta C_i^T(t)\right) \geq 0$
- $\frac{1}{\gamma_3}\Delta b^T(t)\Delta b(t) \geq 0$
- $0 \leq V(t) \leq V(t_0)$
- $\Delta\omega(t_0) = \vec{0}$
- $\Delta\omega^T(t) I \Delta\omega(t) \geq 0$
- $\frac{1}{\gamma_1}\operatorname{tr}\left(\Delta I(t)\Delta I^T(t)\right) = \frac{1}{\gamma_1}\sum_{i=1}^{3}|\Delta\lambda_i(t)|^2 = \frac{1}{\gamma_1}\|\Delta I(t)\|_F^2$

These facts can be used to show

$$\begin{aligned}
\frac{1}{\gamma_1}\|\Delta I(t)\|_F^2 \leq & \frac{1}{\gamma_1}\operatorname{tr}\left(\Delta I(t)\Delta I^T(t)\right) \\
\leq & \frac{1}{\gamma_1}\operatorname{tr}\left(\Delta I(t)\Delta I^T(t)\right) + \Delta\omega^T(t) I \Delta\omega(t) + \frac{1}{\gamma_2}\sum_{i=1}^{3}\operatorname{tr}\left(\Delta C_i(t)\Delta C_i^T(t)\right) \\
& + \frac{1}{\gamma_3}\Delta b^T(t)\Delta b(t) \\
\leq & 2V(t) \\
\leq & 2V(t_0) \\
\leq & \frac{1}{\gamma_1}\|\Delta I(t_0)\|_F^2 + \frac{1}{\gamma_2}\sum_{i=1}^{3}\|\Delta C_i(t_0)\|_F^2 + \frac{1}{\gamma_3}\|\Delta b(t_0)\|^2. \qquad (4.18)
\end{aligned}$$

or equivalently,

$$\|\Delta I(t)\|_F \leq \left(\|\Delta I(t_0)\|_F^2 + \frac{\gamma_1}{\gamma_2} \sum_{i=1}^{3} \|\Delta C_i(t_0)\|_F^2 + \frac{\gamma_1}{\gamma_3} \|\Delta b(t_0)\|^2 \right)^{1/2}. \tag{4.19}$$

By the Rayleigh-Ritz Theorem, $\min_{\|x\|=1} x^T \hat{I}(t) x = \hat{\lambda}_3(t)$. Additionally since $\hat{I}(t) = I + \Delta I(t)$ and by assumption $\left(\|\Delta I(t_0)\|_F^2 + \frac{\gamma_1}{\gamma_2} \sum_{i=1}^{3} \|\Delta C_i(t_0)\|_F^2 + \frac{\gamma_1}{\gamma_3} \|\Delta b(t_0)\|^2 \right)^{1/2} + \epsilon \leq \lambda_3$, the following inequalities hold:

$$\begin{aligned}
\hat{\lambda}_3(t) &= \min_{\|x\|=1} \left(x^T I x + x^T \Delta I(t) x \right) \\
&\geq \min_{\|x\|=1} \left(x^T I x \right) - \max_{\|x\|=1} |x^T \Delta I(t) x| \\
&\geq \lambda_3 - \|\Delta I(t)\|_2 \\
&\geq \lambda_3 - \left(\sum_{i=1}^{3} |\Delta \lambda_i(t)|^2 \right)^{1/2} \\
&\geq \lambda_3 - \|\Delta I(t)\|_F \\
&\geq \lambda_3 - \left(\|\Delta I(t_0)\|_F^2 + \frac{\gamma_1}{\gamma_2} \sum_{i=1}^{3} \|\Delta C_i(t_0)\|_F^2 + \frac{\gamma_1}{\gamma_3} \|\Delta b(t_0)\|^2 \right)^{1/2} \\
&\geq \lambda_3 - (\lambda_3 - \epsilon) \\
&\geq \epsilon
\end{aligned} \tag{4.20}$$

where ϵ is a finite positive scalar and we use the fact that $\|\Delta I(t)\|_2^2 = \max(|\Delta \lambda_1(t)|^2, |\Delta \lambda_3(t)|^2)$ because the singular values of a symmetric matrix are equal to the absolute values of its eigenvalues. The above inequality guarantees that all eigenvalues of $\hat{I}(t)$ are positive and bounded away from zero for all time. The fact that all signals in (2.40) and (4.10) are bounded implies that $\dot{\omega}$ and $\dot{\hat{\omega}}$ are bounded. These bounded signals

imply that $\Delta\dot{\omega}$ is bounded. Note that bounded $\Delta\dot{\omega}$ and $\Delta\omega \in \mathcal{L}_2$ implies

$$\lim_{t\to\infty} \Delta\omega = \vec{0}. \tag{4.21}$$

Since every signal in the parameter update equations (4.11)-(4.13) are bounded and $\lim_{t\to\infty} \Delta\omega = \vec{0}$ this implies

$$\begin{aligned} &\lim_{t\to\infty} \dot{\hat{I}} = 0_{3\times 3}, \\ &\lim_{t\to\infty} \dot{\hat{C}}_i = 0_{3\times 3} \ \ \forall i \in \{1,2,3\}, \\ &\lim_{t\to\infty} \dot{\hat{b}} = \vec{0}. \end{aligned} \tag{4.22}$$

The estimator's angular velocity asymptotically converge to the angular velocity of the actual plant, and the estimated parameters converge to constant values. Thus, the local stability of the reported AID algorithm for UV rotational dynamics is proven.

4.3 6-DOF UV AID

This Section reports a novel nonlinear AID algorithm for 6-DOF UV plant models of the form (2.44). A local stability analysis is also included. This proof of Theorem 4.3.1 is provided in two parts. First, in Section 4.2.1, the error system is developed. Then, in Section 4.2.2, we prove the result.

Theorem 4.3.1 *Consider the following AID algorithm for plants of the form (2.44):*

$$\dot{\hat{v}} = \hat{M}^{-1}\left(\mathrm{ad}_v^T(\hat{M}v) + \left(\sum_{i=1}^{6}|v_i|\hat{D}_i\right)v + \hat{\mathcal{G}}(R) + u\right) - a\Delta v \tag{4.23}$$

$$\dot{\hat{M}} = \frac{\gamma_1}{2}\left(-\psi_1 v^T - v\psi_1^T + \Delta v\psi_2^T + \psi_2\Delta v^T\right) \tag{4.24}$$

$$\dot{\hat{D}}_i = -\gamma_2|v_i|\Delta v v^T \tag{4.25}$$

$$\dot{\hat{g}} = -\gamma_3\Delta\nu^T R^T e_3 \tag{4.26}$$

$$\dot{\hat{b}} = \gamma_4\mathcal{J}(\Delta\omega)R^T e_3 \tag{4.27}$$

with the following definitions:

- $a, \gamma_1, \gamma_2, \gamma_3, \gamma_4 \in \mathbb{R}_+$
- $\hat{\mathcal{G}}(R) = \begin{bmatrix} \hat{g}R^T e_3 \\ \mathcal{J}(\hat{b})R^T e_3 \end{bmatrix}$
- $\psi_1 = \mathrm{ad}_v(\Delta v)$
- ψ_2 *such that*

$$\begin{aligned}\psi_2 =& \dot{\hat{v}} + a\Delta v \\ =& \hat{M}^{-1}\left(\mathrm{ad}_v^T(\hat{M}v) + \left(\sum_{i=1}^{6}|v_i|\hat{D}_i\right)v + \hat{\mathcal{G}}(R) + u\right)\end{aligned} \tag{4.28}$$

and the following assumptions:

- $u(t)$ *is bounded by assumption*
- $\hat{M}(t_0)$ *is PDS*

- $\hat{v}(t_0) = v(t_0)$

- $\exists \epsilon \in \mathbb{R}_+$ *such that* $\mathcal{T}(t_0)^{1/2} + \epsilon \leq \lambda_6$ *where*

$$\mathcal{T}(t_0) = \|\Delta M(t_0)\|_F^2 + \frac{\gamma_1}{\gamma_2}\sum_{i=1}^{6}\|\Delta D_i(t_0)\|_F^2 + \frac{\gamma_1}{\gamma_3}\Delta g(t_0)^2 + \frac{\gamma_1}{\gamma_4}\|\Delta b(t_0)\|^2. \quad (4.29)$$

Under these conditions the estimated angular and linear velocities will be asymptotically stable in the sense of Lyapunov, i.e., $\lim_{t\to\infty}\Delta v = \vec{0}$*, and the parameter estimates will converge to constant values, i.e.,* $\lim_{t\to\infty}\dot{\hat{M}}(t) = 0_{6\times 6}$*,* $\lim_{t\to\infty}\dot{\hat{D}}_i(t) = 0_{6\times 6}$*,* $\lim_{t\to\infty}\dot{\hat{g}}(t) = 0$*, and* $\lim_{t\to\infty}\dot{\hat{b}}(t) = \vec{0}$*.*

This local stability result implies that the plant parameter estimates converge to values that provide plant model input-output behavior identical to that of the actual experimental plant for the given input force and torque signals. Note that since the initial mass matrix estimate is PDS and the parameter estimate law is symmetric, both $\hat{M}(t)$ and $\Delta M(t)$ will be symmetric, and thus they will have strictly real eigenvalues.

4.3.1 UV AID Error System

Note the actual plant parameters are constant, thus $\Delta\dot{M} = \dot{\hat{M}}$, $\Delta\dot{D}_i = \dot{\hat{D}}_i$, $\Delta\dot{g} = \dot{\hat{g}}$, and $\Delta\dot{b} = \dot{\hat{b}}$. Using $M\hat{M}^{-1} = \mathbb{I} - \Delta M\hat{M}^{-1}$ (where $\mathbb{I}$ is the identity matrix) and $\Delta\mathcal{G}(R) = \begin{bmatrix} \Delta g R^T e_3 \\ \mathcal{J}(\Delta b)R^T e_3 \end{bmatrix}$ the expression for velocity error dynamics becomes

$$
\begin{aligned}
M\Delta\dot{v} =& M\left(\dot{\hat{v}} - \dot{v}\right) \\
=& -aM\Delta v + M\hat{M}^{-1}\left(\mathrm{ad}_v^T(\hat{M}v) + \left(\sum_{i=1}^{6}|v_i|\hat{D}_i\right)v + \hat{\mathcal{G}}(R) + u\right) \\
& - \left(\mathrm{ad}_v^T(Mv) + \left(\sum_{i=1}^{6}|v_i|D_i\right)v + \mathcal{G}(R) + u\right) \\
=& -aM\Delta v + \left(\mathrm{ad}_v^T(\hat{M}v) + \left(\sum_{i=1}^{6}|v_i|\hat{D}_i\right)v + \hat{\mathcal{G}}(R) + u\right) - \Delta M\psi_2 \\
& - \left(\mathrm{ad}_v^T(Mv) + \left(\sum_{i=1}^{6}|v_i|D_i\right)v + \mathcal{G}(R) + u\right) \\
=& -aM\Delta v - \Delta M\psi_2 + \mathrm{ad}_v^T(\Delta Mv) + \left(\sum_{i=1}^{6}|v_i|\Delta D_i\right)v + \Delta\mathcal{G}(R) \qquad (4.30)
\end{aligned}
$$

4.3.2 UV AID Convergence Proof

Consider the following Lyapunov function candidate

$$
V(t) = \frac{1}{2}\Delta v^T M\Delta v + \frac{1}{2\gamma_1}\,\mathrm{tr}\left(\Delta M\Delta M^T\right) + \frac{1}{2\gamma_2}\sum_{i=1}^{6}\mathrm{tr}\left(\Delta D_i\Delta D_i^T\right) + \frac{1}{2\gamma_3}\Delta g^2 + \frac{1}{2\gamma_4}\Delta b^T\Delta b \qquad (4.31)
$$

$V(t)$ is

- positive definite
- equal to zero if and only if $\Delta v = \vec{0}$, $\Delta M = 0_{6\times6}$,$\forall i$ $\Delta D_i = 0_{6\times6}$, $\Delta g = 0$, and $\Delta b = \vec{0}$.

From (4.30) and the facts that for any matrices A and B of appropriate dimension $\mathrm{tr}(AB) = \mathrm{tr}(BA)$ and for any $x_1, x_2, x_3 \in \mathbb{R}^3 \quad x_1^T\mathcal{J}(x_2)x_3 = -x_2^T\mathcal{J}(x_1)x_3$, the time derivative of

(4.31) is

$$
\begin{aligned}
\dot{V}(t) =& \frac{1}{2}\left(\Delta\dot{v}^T M\Delta v + \Delta v^T M\Delta\dot{v}\right) + \frac{1}{\gamma_1}\operatorname{tr}\left(\Delta M\Delta\dot{M}^T\right) \\
&+ \frac{1}{\gamma_2}\sum_{i=1}^{6}\operatorname{tr}\left(\Delta D_i\Delta\dot{D}_i^T\right) + \frac{1}{\gamma_3}\Delta g\Delta\dot{g} + \frac{1}{\gamma_4}\Delta b^T\Delta\dot{b} \\
=& -a\Delta v^T M\Delta v + \frac{1}{2}\left(\mathrm{ad}_v^T(\Delta M v) - \Delta M\psi_2\right)^T\Delta v + \frac{1}{2}\Delta v^T\left(\mathrm{ad}_v^T(\Delta M v) - \Delta M\psi_2\right) \\
&+ \frac{1}{\gamma_1}\operatorname{tr}\left(\Delta M\Delta\dot{M}^T\right) + \Delta v^T\left(\sum_{i=1}^{6}|v_i|\Delta D_i\right)v + \frac{1}{\gamma_2}\sum_{i=1}^{6}\operatorname{tr}\left(\Delta D_i\Delta\dot{D}_i^T\right) \\
&+ \Delta v^T\Delta\mathcal{G}(R) + \frac{1}{\gamma_3}\Delta g\Delta\dot{g} + \frac{1}{\gamma_4}\Delta b^T\Delta\dot{b} \\
=& -a\Delta v^T M\Delta v + \frac{1}{2}\left(\psi_1^T\Delta M v - \Delta v^T\Delta M\psi_2\right) + \frac{1}{2}\left(v^T\Delta M\psi_1 - \psi_2^T\Delta M\Delta v\right) \\
&+ \frac{1}{\gamma_1}\operatorname{tr}\left(\Delta M\Delta\dot{M}^T\right) + \frac{1}{\gamma_2}\sum_{i=1}^{6}\operatorname{tr}\left(\Delta D_i\Delta\dot{D}_i^T\right) + \sum_{i=1}^{6}\left(|v_i|\Delta v^T\Delta D_i v\right) \\
&+ \frac{1}{\gamma_3}\Delta g\Delta\dot{g} + \frac{1}{\gamma_4}\Delta b^T\Delta\dot{b} + \begin{bmatrix} \Delta\nu^T & \Delta\omega^T \end{bmatrix}\begin{bmatrix} \Delta g R^T e_3 \\ \mathcal{J}(\Delta b)R^T e_3 \end{bmatrix} \\
=& -a\Delta v^T M\Delta v + \frac{1}{\gamma_1}\operatorname{tr}\left(\Delta M\Delta\dot{M}^T\right) + \frac{1}{2}\operatorname{tr}\left(\Delta M\left(\psi_1 v^T - \Delta v\psi_2^T + v\psi_1^T - \psi_2\Delta v^T\right)\right) \\
&+ \frac{1}{\gamma_2}\sum_{i=1}^{6}\operatorname{tr}\left(\Delta D_i\Delta\dot{D}_i^T\right) + \sum_{i=1}^{6}\operatorname{tr}\left(|v_i|\Delta D_i v\Delta v^T\right) + \frac{1}{\gamma_3}\Delta g\Delta\dot{g} + \Delta\nu^T\Delta g R^T e_3 \\
&+ \frac{1}{\gamma_4}\Delta b^T\Delta\dot{b} + \Delta\omega^T\mathcal{J}(\Delta b)R^T e_3 \\
=& -a\Delta v^T M\Delta v + \frac{1}{\gamma_1}\operatorname{tr}\left(\Delta M\Delta\dot{M}^T\right) + \frac{1}{2}\operatorname{tr}\left(\Delta M\left(\psi_1 v^T - \Delta v\psi_2^T + v\psi_1^T - \psi_2\Delta v^T\right)^T\right) \\
&+ \frac{1}{\gamma_2}\sum_{i=1}^{6}\operatorname{tr}\left(\Delta D_i\Delta\dot{D}_i^T\right) + \sum_{i=1}^{6}\operatorname{tr}\left(\Delta D_i\left(|v_i|\Delta v v^T\right)^T\right) + \frac{1}{\gamma_3}\Delta g\Delta\dot{g} \\
&+ \Delta\nu^T\Delta g R^T e_3 + \frac{1}{\gamma_4}\Delta b^T\Delta\dot{b} - \Delta b^T\mathcal{J}(\Delta\omega)R^T e_3
\end{aligned}
\tag{4.32}
$$

The actual parameters are constant; thus substituting (4.24)-(4.27) into (4.32) yields

$$\dot{V}(t) = -a\Delta v^T M \Delta v, \tag{4.33}$$

which is negative definite in Δv and negative semi-definite in the error coordinates Δv, ΔM, ΔD_i, Δg, and Δb. By Lyapunov's direct method, (4.31) and (4.33) imply that all error coordinates are bounded and stable. The structure of $\dot{V}(t)$ implies that $\Delta v \in \mathcal{L}_2$ or, equivalently, $\lim_{t\to\infty} \left(\int_{t_0}^{t} \Delta v^T \Delta v \right)^{1/2} < \infty$. We must ensure every signal in (4.23)-(4.27) is bounded. With v, u, Δv, ΔM, ΔD_i, Δg, and Δb bounded and M, D_i, g, and b constant, and given (4.5)-(4.9) we can conclude that $\hat{v}$, $\hat{M}$, $\hat{D}_i$, $\hat{g}$, and $\hat{b}$ are bounded. All that remains is showing that $\hat{M}^{-1}$ is bounded. Note for $\forall t > t_0$ the following hold:

- $\frac{1}{\gamma_2} \sum_{i=1}^{6} \operatorname{tr}\left(\Delta D_i(t) \Delta D_i^T(t)\right) \geq 0$
- $\frac{1}{\gamma_3} \Delta g(t)^2 \geq 0$
- $\frac{1}{\gamma_4} \Delta b^T(t) \Delta b(t) \geq 0$
- $0 \leq V(t) \leq V(t_0)$
- $\Delta v(t_0) = \vec{0}$
- $\Delta v^T(t) M \Delta v(t) \geq 0$
- $\frac{1}{\gamma_1} \operatorname{tr}\left(\Delta M(t) \Delta M^T(t)\right) = \frac{1}{\gamma_1} \sum_{i=1}^{6} |\Delta \lambda_i(t)|^2 = \frac{1}{\gamma_1} \|\Delta M(t)\|_F^2$

These facts can be used to show

$$\begin{aligned}
\frac{1}{\gamma_1}\|\Delta M(t)\|_F^2 \leq & \frac{1}{\gamma_1}\operatorname{tr}\left(\Delta M(t)\Delta M^T(t)\right) \\
\leq & \frac{1}{\gamma_1}\operatorname{tr}\left(\Delta M(t)\Delta M^T(t)\right) + \Delta v^T(t) M \Delta v(t) + \frac{1}{\gamma_2}\sum_{i=1}^{6}\operatorname{tr}\left(\Delta D_i(t)\Delta D_i^T(t)\right) \\
& + \frac{1}{\gamma_3}\Delta g(t)^2 + \frac{1}{\gamma_4}\Delta b^T(t)\Delta b(t) \\
\leq & 2V(t) \\
\leq & 2V(t_0) \\
\leq & \frac{1}{\gamma_1}\|\Delta M(t_0)\|_F^2 + \frac{1}{\gamma_2}\sum_{i=1}^{6}\|\Delta D_i(t_0)\|_F^2 + \frac{1}{\gamma_3}\Delta g(t_0)^2 + \frac{1}{\gamma_4}\|\Delta b(t_0)\|^2,
\end{aligned} \tag{4.34}$$

or equivalently,

$$\|\Delta M(t)\|_F \leq \mathcal{T}(t_0)^{1/2}. \tag{4.35}$$

By the Rayleigh-Ritz Theorem, $\min_{\|x\|=1} x^T \hat{M}(t) x = \hat{\lambda}_6(t)$. Additionally since $\hat{M}(t) = M + \Delta M(t)$ and by assumption $\mathcal{T}(t_0)^{1/2} + \epsilon \leq \lambda_6$, the following inequalities hold:

$$\begin{aligned}
\hat{\lambda}_6(t) &= \min_{\|x\|=1} \left(x^T M x + x^T \Delta M(t) x \right) \\
&\geq \min_{\|x\|=1} \left(x^T M x \right) - \max_{\|x\|=1} |x^T \Delta M(t) x| \\
&\geq \lambda_6 - \|\Delta M(t)\|_2 \\
&\geq \lambda_6 - \left(\sum_{i=1}^{6} |\Delta \lambda_i(t)|^2 \right)^{1/2} \\
&\geq \lambda_6 - \|\Delta M(t)\|_F \\
&\geq \lambda_6 - \mathcal{T}(t_0)^{1/2} \\
&\geq \lambda_6 - (\lambda_6 - \epsilon) \\
&\geq \epsilon
\end{aligned} \tag{4.36}$$

where ϵ is a finite positive scalar and we use the fact that $\|\Delta M(t)\|_2^2 = \max(|\Delta \lambda_1(t)|^2, |\Delta \lambda_6(t)|^2)$ because the singular values of a symmetric matrix are equal to the absolute values of its eigenvalues. The above inequality guarantees that all eigenvalues of $\hat{M}(t)$ are positive and bounded away from zero for all time. The fact that all signals in (2.44) and (4.23) are bounded implies that $\dot{v}$ and $\dot{\hat{v}}$ are bounded. These bounded signals imply that $\Delta \dot{v}$ is bounded. Note that bounded $\Delta \dot{v}$ and $\Delta v \in \mathcal{L}_2$ implies

$$\lim_{t \to \infty} \Delta v = \vec{0}. \tag{4.37}$$

Since every signal in the parameter update equations (4.24)-(4.27) are bounded and $\lim_{t\to\infty} \Delta v = \vec{0}$ this implies

$$\begin{aligned}
&\lim_{t\to\infty} \dot{\hat{M}} = 0_{6\times 6}, \\
&\lim_{t\to\infty} \dot{\hat{D}}_i = 0_{6\times 6} \ \ \forall i \in \{1, \cdots, 6\}, \\
&\lim_{t\to\infty} \dot{\hat{g}} = 0, \text{ and} \\
&\lim_{t\to\infty} \dot{\hat{b}} = \vec{0}.
\end{aligned} \tag{4.38}$$

The estimator's angular and linear velocities asymptotically converge to the velocities of the actual plant, and the estimated parameters converge to constant values. Thus, the local stability of the reported AID algorithm for 6-DOF UV dynamics is proven.

4.4 UV Least Squares Parameter Identification

This Section reviews the method of least squares experimental identification of plant parameters for two UV models. As shown in Section 2.5.2, the underwater vehicle rotational dynamics plant model, (2.40), can be rewritten as

$$\tau(t) = \mathbb{W}_{UVR}(\omega, \dot{\omega}, R)\theta_{UVR} \tag{4.39}$$

where the UVR subscript denotes UV rotational dynamics, $\mathbb{W}_{UVR} : \mathbb{R}^3 \times \mathbb{R}^3 \times \mathrm{SO}(3) \to \mathbb{R}^{3\times 36}$ is a regressor matrix, and $\theta_{UVR} \in \mathbb{R}^{36}$ is a vector of the unique scalar parameter values in I, C, and b. As shown in Section 2.6, the underwater vehicle plant model, (2.44),

can be rewritten as

$$\tau(t) = \mathbb{W}_{UV}(v, \dot{v}, R)\theta_{UV} \tag{4.40}$$

where the UV subscript denotes 6-DOF UV dynamics, $\mathbb{W}_{UV} : \mathbb{R}^6 \times \mathbb{R}^6 \times \mathrm{SO}(3) \to \mathbb{R}^{6\times 241}$ is a regressor matrix, and $\theta_{UV} \in \mathbb{R}^{241}$ is a vector of the unique scalar parameter values in M, D, g, and b.

The linearity of (4.39) and (4.40) in their respective parameters allows the use of a number of methods to estimate these parameters. A common method is least squares identification (LS). LS for (4.39) requires the signals $\tau(t)$, $\omega(t)$, $\dot{\omega}(t)$, and $R(t)$ to be instrumented. Similarly, LS for (4.40) requires the signals $f(t)$, $\tau(t)$, $\nu(t)$, $\dot{\nu}(t)$, $\omega(t)$, $\dot{\omega}(t)$, and $R(t)$ to be instrumented. One method of formulating the LS using the regressor matrix $\mathbb{W}_{UV}$ is to employ sampled experimental data of the form $\{f(t_i),\ R(t_i),\ v(t_i),\ \dot{v}(t_i)\}$, $t_i \in \{1, 2, \cdots n\}$. From (4.40) we have $f(t_i) = \mathbb{W}_{UV}(v(t_i), \dot{v}(t_i), R(t_i))\theta_{UV} \quad \forall i \in \{1, 2, \cdots, n\}$. Thus if we define $F = [f(t_1)^T\ f(t_2)^T\ \cdots\ f(t_n)^T]^T$ and

$$\mathcal{W}_{UV} = \begin{bmatrix} \mathbb{W}_{UV}(v(t_1), \dot{v}(t_1), R(t_1)) \\ \mathbb{W}_{UV}(v(t_2), \dot{v}(t_2), R(t_2)) \\ \vdots \\ \mathbb{W}_{UV}(v(t_n), \dot{v}(t_n), R(t_n)) \end{bmatrix}, \tag{4.41}$$

then the following relation holds

$$F = \mathcal{W}_{UV}\theta_{UV} \tag{4.42}$$

where F and $\mathcal{W}_{UV}$ are know and θ_{UV} is unknown. The Moore-Penrose psudo inverse of

$\mathcal{W}_{UV}$ provides the best estimate of θ_{UV} in the least-squares sense through the formula

$$\theta_{UV} = \mathcal{W}_{UV}^{\dagger} F. \tag{4.43}$$

If $\mathcal{W}_{UV}$ is full rank, then the solution θ_{UV} will be unique. A similar relationship can be derived for θ_{UVR}.

In most plants angular acceleration, $\dot{\omega}(t)$, is not instrumented directly and must be estimated by differentiating the angular velocity signal, $\omega(t)$, or twice differentiating angular position signals. The LS algorithm was implemented using a single Moore-Penrose pseudo inverse for Sections 4.5 and 4.6. In the experiments reported herein, the JHU ROV experienced angular velocities on the order of 10°/s. Since the PHINS inertial navigation system (INS) measures the vehicle's angular velocity to within 0.01°/s, we found that numerical differentiation of the angular velocity signals provided angular acceleration signals adequate for LS. Inertial-grade angular acceleration sensors are not widely available; many UV are not equipped with angular velocity sensors accurate enough for precise numerical differentiation. AID might be a better option over LS for some UV in the field. The UV AID algorithm reported herein requires only the signals $u(t)$, $\tau(t)$, $R(t)$, $\nu(t)$, and $\omega(t)$.

4.5 Experimental Evaluation:

3-DOF UV Rotational Dynamics AID

This Section reports a comparative experimental evaluation of AID and LS for the estimation of plant parameters for the rotational dynamics of a UV. We employed the Johns Hopkins University Hydrodynamic Test Facility to evaluate each parameter identification method's capacity to identify parameter sets which accurately model UV dynamics. The error between the predicted model performance and the experimentally observed performance is reported as the mean absolute error (MAE) between the simulated plant roll, pitch, and velocities and the actual experimental plant roll, pitch, and velocities. Appendices A.1 and A.2 provide further details about our experimental setup and parameter evaluation method.

At the beginning of each experiment, the vehicle was positioned in the center of the tank with the vehicle's depth under closed loop control at about a $1\ \mathrm{m}$ depth with the x and y DOF unactuated. During the experiment three sinusoidal torque commands (one in the direction of each axis of the vehicle's coordinate frame) actuated the angular position of the JHU ROV. Table 4.5 shows the details of two exogenous inputs, one for system identification and one for cross validation. Hereafter we will refer to these experiments as the experiment for parameter identification (IDDAT) and the experiment for cross-validation (CROSS) respectively.

AID was implemented as a discrete time approximation of the continuous time algo-

Table 4.1: Exogenous Inputs for UV Rotational Dynamics Parameter Identification Experiments

Experiment		IDDAT	CROSS
Experiment Purpose		Parameter Identification	Parameter Cross-Validation
Experiment Date		2012-04-14	2012-04-09
Experiment Run Time		22.0 min	21.7 min
Torque about X Vector	Cos Freq	0.503 rad/sec	0.583 rad/sec
	Cos Amp	40 N m	40 N m
Torque about Y Vector	Cos Freq	0.663 rad/sec	1.012 rad/sec
	Cos Amp	55 N m	55 N m
Torque about Z Vector	Cos Freq	1.043 rad/sec	0.733 rad/sec
	Cos Amp	70 N m	70 N m

Table 4.2: Numerical Values of the INITP used to initialize UV rotational dynamics AID.

Parameter Symbol	initialization parameter set (INITP)
$\hat{I}(t_0)$	$\begin{bmatrix} 100.0 & 0 & 0 \\ 0 & 100.0 & 0 \\ 0 & 0 & 100.0 \end{bmatrix}$
$\hat{C}_1(t_0)$	$\begin{bmatrix} -100.0 & 0 & 0 \\ 0 & -100.0 & 0 \\ 0 & 0 & -100.0 \end{bmatrix}$
$\hat{C}_2(t_0)$	$\begin{bmatrix} -100.0 & 0 & 0 \\ 0 & -100.0 & 0 \\ 0 & 0 & -100.0 \end{bmatrix}$
$\hat{C}_3(t_0)$	$\begin{bmatrix} -100.0 & 0 & 0 \\ 0 & -100.0 & 0 \\ 0 & 0 & -100.0 \end{bmatrix}$
$\hat{b}(t_0)$	$\begin{bmatrix} 0 \\ 0 \\ 100.0 \end{bmatrix}$

rithm. Euler integration of (4.10)—(4.13) for 100ms time steps provided the time series of parameter and angular velocity estimates. 100ms is one to two orders-of-magnitude smaller than the state signal variation rates of 1 second or greater observed during quasi-periodic JHU ROV operations. The experiments were designed to generate thruster commands varying slowly enough to admit the use of steady state thruster models. In practice, first-order Euler integration provided performance similar to the 4th-order integration implemented in simulation.

The AID algorithm was initialized with the measured angular position, measured angular velocity, and initialization parameter set (INITP) in Table 4.2. Note that the INITP was chosen such that each scalar parameter was within an order-of-magnitude of the value to be identified. The choice of optimal adaptation gains is a long-standing open problem in adaptive systems theory [51, 52]. From simulations of this AID algorithm which sparsely covered a roughly logarithmic scaling for a range of possible gains, we empirically chose angular velocity, inertia tensor, quadratic drag, and buoyancy torque adaption gains of $a = 10$, $\gamma_1 = 5000$, $\gamma_2 = 10000$, and $\gamma_3 = 1000$ respectively. Many of the gain combinations considered provided parameter convergence rates comparable to the gains used herein. Our simulation studies suggest similar results would be obtained for initial condition and gain choices within an order-of-magnitude of the choices made.

4.5.1 Experimental Results

The state measurements from the IDDAT dataset were used to identify the plant parameters of the plant model (2.40) with both the adaptive identification and least squares methods. Table 4.4 reports two identified parameter sets: the adaptively identified parameter set (AIDP) estimated with AID (as per Section 4.2) and the least squares identified parameter set (LSP) estimated with LS (as per Section 4.4).

The parameter sets AIDP, LSP, and INITP were used as parameter sets for three UV rotational dynamics models; the adaptively identified plant model (AIDPM), the least squares identified plant model (LSPM), and the initialization parameter set plant model (INITPM). Using the torque input commands from the IDDAT and CROSS datasets, we compare simulated JHU ROV performance from numerical simulations of AIDPM, LSPM, and INITPM to the measured JHU ROV states for each experiment respectively.

Using the torque inputs from the CROSS dataset, Figures 4.1 — 4.4 compare the state measurements from simulations of AIDPM, LSPM, and INITPM to the measured JHU ROV states from the CROSS dataset. Each of these four Figures display three minute subsets of the 20 minutes of state data generated by driving simulations of AIDPM, LSPM, and INITPM using the torque data from the CROSS dataset. Similar simulations of AIDPM, LSPM, and INITPM were created using the torque commands from the IDDAT dataset. Table 4.3 summarizes the MAE between measured and simulated vehicle state for each experimental dataset, UV vehicle model, and open-loop-stable DOF.

Table 4.3: mean absolute errors (MAEs) between measured and simulated vehicle states for all pairs of UV rotational dynamics experiments and UV rotational dynamics models.

UV		Angular Pose		Angular Velocity		
Model	Experiment	Roll	Pitch	x DOF	y DOF	z DOF
AIDPM	CROSS	4.11°	2.88°	6.16°/s	2.83°/s	3.44°/s
LSPM	CROSS	2.50°	2.65°	3.36°/s	3.69°/s	5.46°/s
INITPM	CROSS	13.3°	14.6°	8.86°/s	12.9°/s	7.00°/s
AIDPM	IDDAT	3.44°	2.06°	4.80°/s	1.99°/s	4.03°/s
LSPM	IDDAT	2.08°	1.76°	2.45°/s	2.19°/s	5.05°/s
INITPM	IDDAT	14.8°	17.1°	8.83°/s	10.7°/s	6.32°/s

Table 4.4: The UV rotational dynamics parameter sets identified using the IDDAT dataset.

Parameter Symbol	AIDP	LSP
$\hat{I}(t_f)$	$\begin{bmatrix} 136.0 & -12.7 & 2.89 \\ -12.7 & 175.0 & -1.06 \\ 2.89 & -1.06 & 160.0 \end{bmatrix}$	$\begin{bmatrix} 31.9 & -5.04 & 1.53 \\ -5.04 & 55.9 & -6.19 \\ 1.53 & -6.19 & 96.3 \end{bmatrix}$
$\hat{C}_1(t_f)$	$\begin{bmatrix} -215.0 & 19.1 & 21.3 \\ -23.0 & -243.0 & -10.1 \\ 7.16 & -80.9 & -129.0 \end{bmatrix}$	$\begin{bmatrix} -297.0 & 4.14 & 1.32 \\ 7.6 & -414.0 & -28.1 \\ 150.0 & -165.0 & 52.3 \end{bmatrix}$
$\hat{C}_2(t_f)$	$\begin{bmatrix} -137.0 & 39.8 & 46.5 \\ -14.0 & -367.0 & -39.2 \\ 15.0 & -117.0 & -186.0 \end{bmatrix}$	$\begin{bmatrix} -358.0 & 13.7 & 13.0 \\ 91.8 & -266.0 & -20.5 \\ 107.0 & -181.0 & -80.2 \end{bmatrix}$
$\hat{C}_3(t_f)$	$\begin{bmatrix} -80.6 & 38.4 & -17.3 \\ -2.0 & -287.0 & 19.6 \\ 37.0 & -52.1 & -214.0 \end{bmatrix}$	$\begin{bmatrix} 3.4 & 18.9 & -9.58 \\ -9.27 & -262.0 & 18.2 \\ -70.0 & 34.8 & -252.0 \end{bmatrix}$
$\hat{b}(t_f)$	$\begin{bmatrix} 1.57 \\ -1.5 \\ 277.0 \end{bmatrix}$	$\begin{bmatrix} 1.38 \\ 1.11 \\ 235.0 \end{bmatrix}$

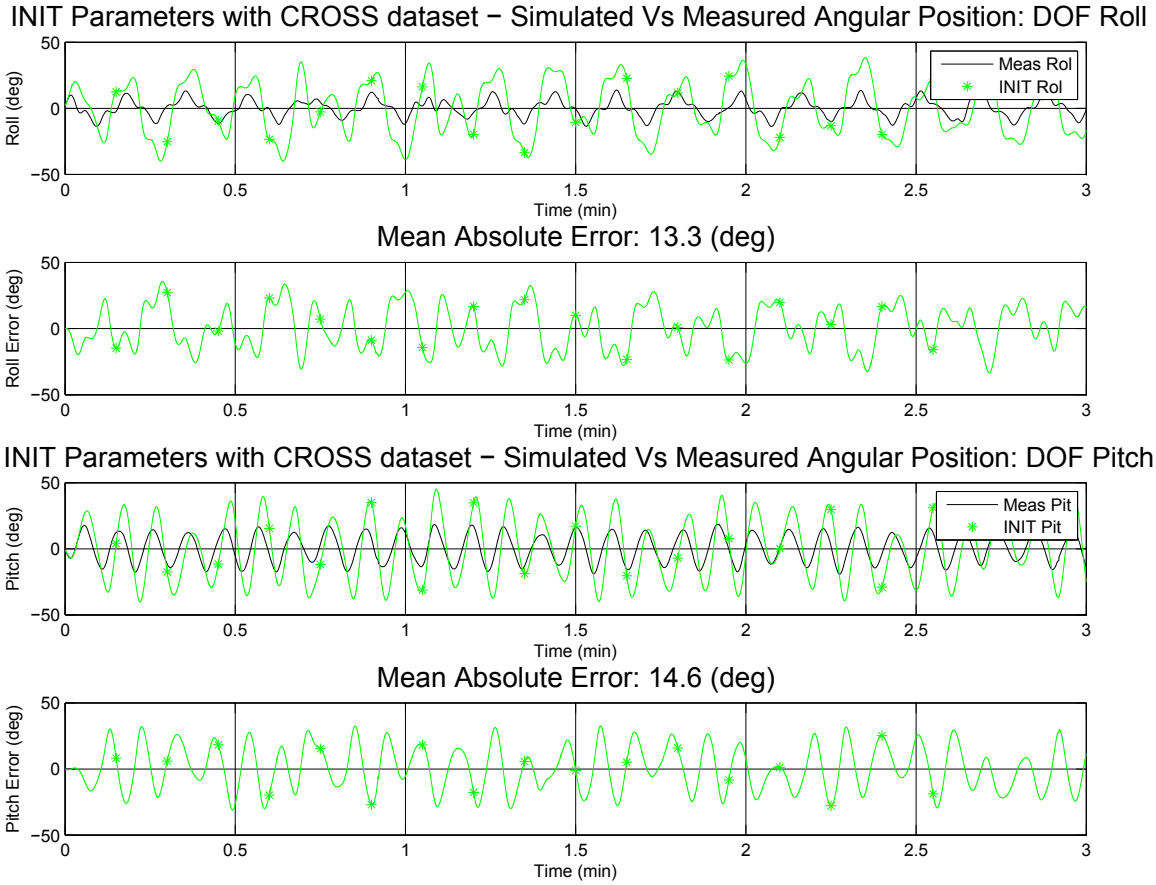

Figure 4.1: Representative data of experimental and simulated JHU ROV angular position for the CROSS dataset. In the roll and pitch plots, the measured states are plotted together with the states from simulating INITPM. For each DOF, the difference between the measured position and simulated position is shown.

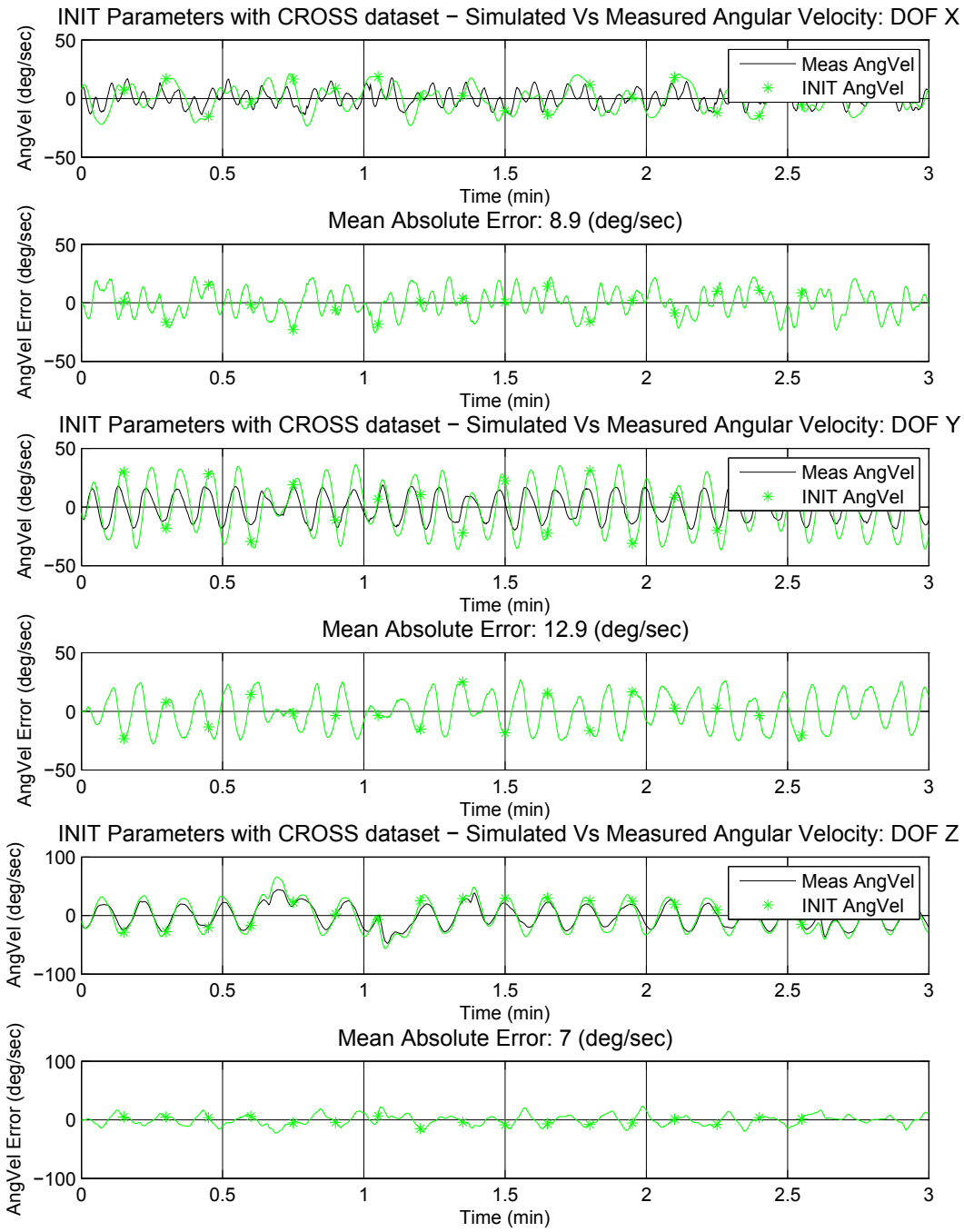

Figure 4.2: Representative data of experimental and simulated JHU ROV angular velocity for the CROSS dataset. In the individual angular velocity plots, each measured velocity is plotted together with the states from simulating INITPM. For each DOF error plots are also included.

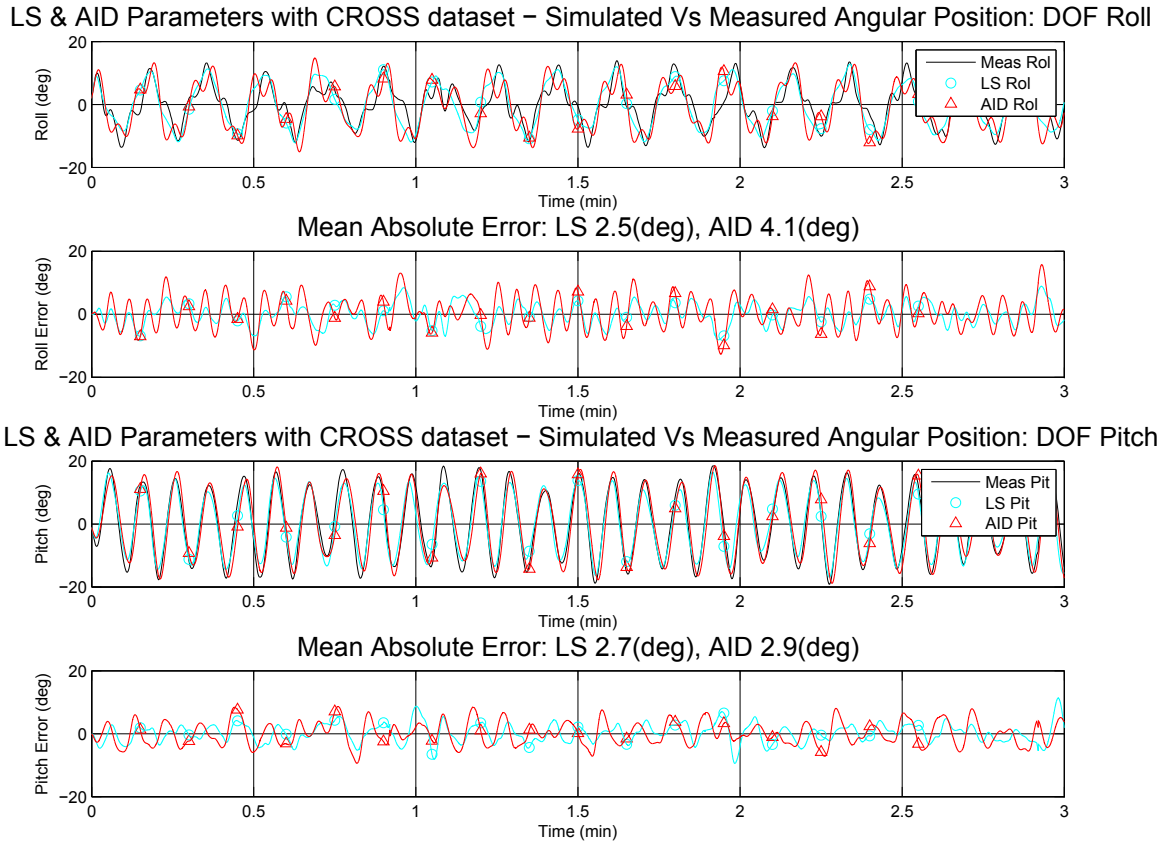

Figure 4.3: Representative data of experimental and simulated JHU ROV angular position for the CROSS dataset. In the roll and pitch plots, the measured position is plotted together with the simulated position from two model simulations. The states from a simulation of AIDPM are plotted in blue and marked with circles. The states from LSPM are plotted in red and marked with triangles. For each DOF, the difference between the measured positions from the CROSS dataset and the states from each model simulation is shown. For each DOF, the difference between the measured position and simulated position is shown.

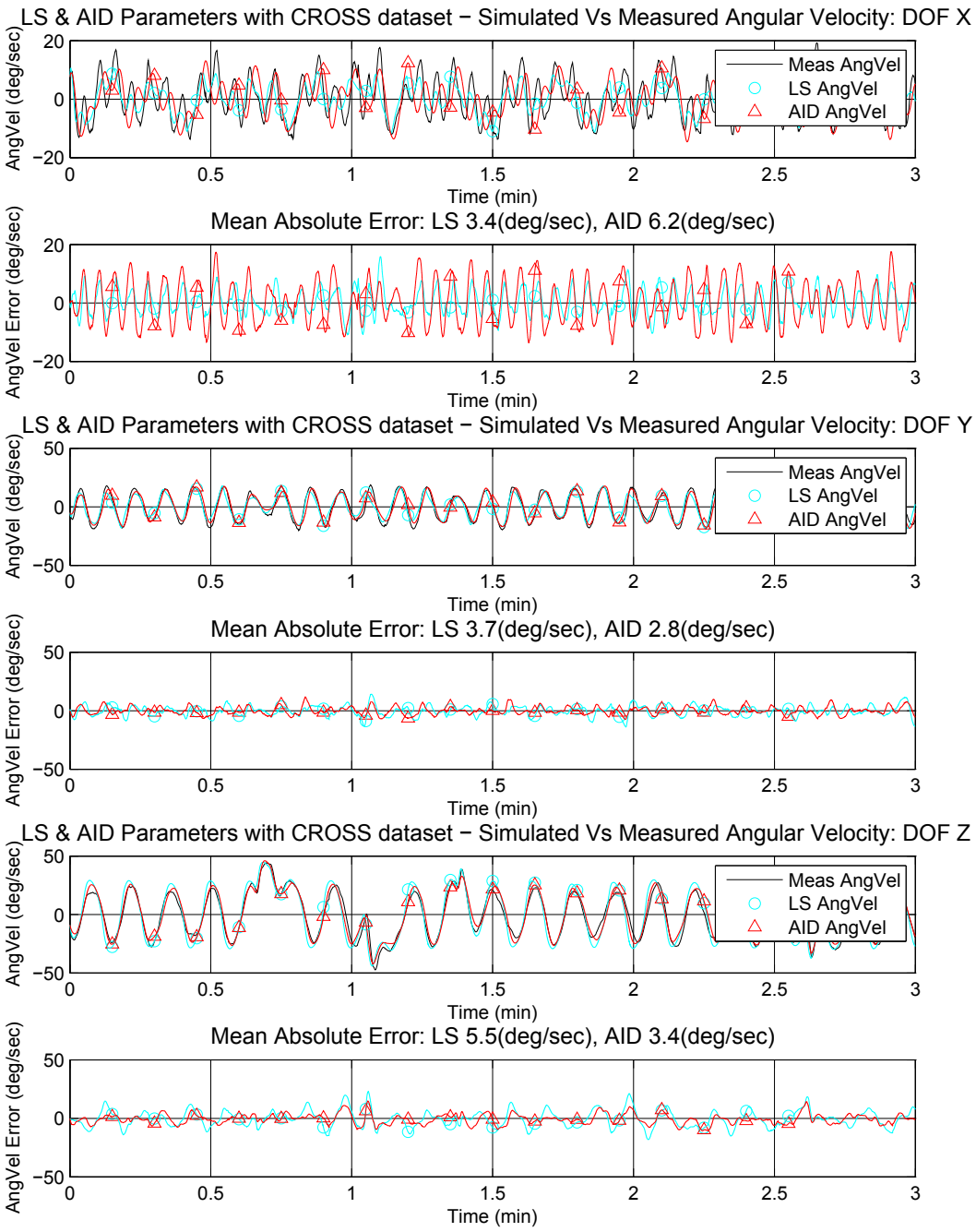

Figure 4.4: Representative data of experimental and simulated JHU ROV angular velocity for the CROSS dataset. In the individual angular velocity plots, each measured velocity is plotted together with velocities from AIDPM and LSPM simulations. For each DOF error plots are also included. See the caption of Figure 4.3 for further information.

4.5.2 Analysis of Experimental Results

Compare the state estimate capacity of INITPM in Figures 4.1 and 4.2 to the state estimate capacity of AIDPM and LSPM Figures 4.3 and 4.4. Clearly the simulated plant model's capacity to match experimentally observed plant performance is dependent on the model's plant parameters. Comparing the states produced by simulating AIDPM and LSPM with those from INITPM (a model which uses the arbitrarily chosen INITP parameter set), we see that both experimentally identified models are better at matching experimentally observed dynamic plant behavior. Table 4.3 confirms that the AIDPM and LSPM are better than the INITPM at modeling JHU ROV performance. In the case of both the IDDAT and CROSS datasets, the performance of the AIDPM and LSPM were similar, i.e. for some DOF the AIDPM states were on average closer to the experimentally measured state values (as shown by smaller MAE values) and for other DOF the LSPM states were on average closer to the experimentally measured values. Figures 4.3 and 4.4 show the dynamic behavior of the two identified models match the experimentally observed JHU ROV performance, though the data in Figure 4.3 suggests that the LSPM is slightly better at matching the JHU ROV's roll and pitch states. For some AIDPM and LSPM DOFs, each model's capacity to match measured states from the CROSS dataset is worse than their capacity to match states from the IDDAT dataset; in Table 4.3 CROSS MAE values can be up to 60% larger that the IDDAT MAE values for the equivalent DOF and UV model. However, the representative sample of data plotted in Figures 4.3 and 4.4 indicate that both AIDPM and LSPM capture the character character of JHU ROV performance during

cross-validation.

From Figures 4.3 and 4.4 note that roll (motion about the x-axis) and the x-axis angular velocity have a more complex motion than the other DOF. This is due to the coupling between the DOF; for the JHU ROV we have observed that when considering angular motion about the x, y, and z axes, x-axis motion is the most sensitive to angular motions about the other axes. Figures 4.3, 4.4, and Table 4.3 show that angular motion about the x-axis are the motions least accurately modeled by the AIDPM. There are several factors we feel contribute to these larger errors. The first is that both thrusters used to achieve torque about the x-axis are positioned within the frame of the vehicle whereas all other thrusters are outside the frame of the vehicle. The internal structures of the vehicle may impede the flow path of these thrusters and, in consequence, degrade their performance. Additionally, vehicle rotation about the x-axis is the DOF with the least damping and least control authority. Thus the lower energy dissipation for rotational motion about the x-axis could lead to higher MAE values for this DOF.

4.6 Experimental Evaluation: 6-DOF UV AID

This Section reports a comparative experimental evaluation of AID and LS for the estimation of plant parameters for the dynamics of a 6-DOF UV. We employed the Johns Hopkins University Hydrodynamic Test Facility to evaluate each parameter identification method's capacity to identify parameter sets which accurately model UV dynamics. The

error between the predicted model performance and the experimentally observed performance is reported as the MAE between the simulated plant roll, pitch, and velocity and the actual experimental plant roll, pitch, and velocity. Appendices A.1 and A.2 provide further details about our experimental setup and parameter evaluation method.

During an experiment, each of the six JHU ROV degree-of-freedom were independently excited with either closed-loop control or open-loop sinusoidal commands. For those DOF using closed-loop control, a sinusoidal reference trajectory was specified to the JHU ROV control system. The reference signals for both experiments are given in Table 4.5.

Table 4.5: Input Specifications for 6-DOF UV Parameter Identification Experiments

Experiment		IDDAT	CROSS
Experiment Purpose		Parameter Identification	Parameter Cross-Validation
Experiment Run Time		31.9 min	34.8 min
DOF world x	*Excitation Type*	*Closed Loop Trajectory-Tracking*	
	Cos Frequency	0.185 rad/sec	0.242 rad/sec
	Cos Amplitude	0.60 m	0.60 m
DOF world y	*Excitation Type*	*Closed Loop Trajectory-Tracking*	
	Cos Frequency	0.286 rad/sec	0.210 rad/sec
	Cos Amplitude	0.60 m	0.60 m
DOF world z	*Excitation Type*	*Closed Loop Trajectory-Tracking*	
	Cos Frequency	0.242 rad/sec	0.185 rad/sec
	Cos Amplitude	0.50 m	0.50 m
Torque about DOF body x	*Excitation Type*	*Open Loop Torque Input*	
	Cos Frequency	0.262 rad/sec	0.224 rad/sec
	Cos Amplitude	40 N m	40 N m
Torque about DOF body y	*Excitation Type*	*Open Loop Torque Input*	
	Cos Frequency	0.449 rad/sec	0.331 rad/sec
	Cos Amplitude	55 N m	55 N m
DOF heading	*Excitation Type*	*Closed Loop Trajectory-Tracking*	
	Cos Frequency	0.210 rad/sec	0.286 rad/sec
	Cos Amplitude	45°	45°

AID was implemented as a discrete time approximation of the continuous time algorithm. Euler integration of (4.23)-(4.27) for 100ms time steps provided the time series of parameter and angular velocity estimates. 100ms is one to two orders-of-magnitude smaller than the state signal variation rates of 1 second or greater observed during quasi-periodic JHU ROV operations. The experiments were designed to generate thruster commands varying slowly enough to admit the use of steady state thruster models. In practice, first-order Euler integration provided performance similar to the 4th-order integration implemented in simulation.

The AID algorithm was initialized with the measured angular position, measured angular velocity, measured translational velocity, and initialization parameter set (INITP) in Tables 4.6 and 4.7. Based on our previous studies with second-order rigid body adaptive identification algorithms (Sections 3.3.4 and 4.5), we chose adaption gains of $a = 10$, $\gamma_1 = 5000$, $\gamma_2 = 20000$, $\gamma_3 = 2000$, and $\gamma_4 = 2000$.

Table 4.6: UV mass and gravitational parameter values used to initialize AID.

Parameter Symbol	INITP Values
$\hat{M}(t_0)$	$\begin{bmatrix} 100.0 & 0 & 0 & 0 & 0 & 0 \\ 0 & 100.0 & 0 & 0 & 0 & 0 \\ 0 & 0 & 100.0 & 0 & 0 & 0 \\ 0 & 0 & 0 & 100.0 & 0 & 0 \\ 0 & 0 & 0 & 0 & 100.0 & 0 \\ 0 & 0 & 0 & 0 & 0 & 100.0 \end{bmatrix}$
$\hat{g}(t_0)$	0.0
$\hat{b}(t_0)$	$\begin{bmatrix} 0 \\ 0 \\ 100.0 \end{bmatrix}$

Table 4.7: The UV drag parameter values used to initialize AID.

Parameter Symbol	INITP Values
$\hat{D}_1(t_0)$	$\begin{bmatrix} -100.0 & 0 & 0 & 0 & 0 & 0 \\ 0 & -100.0 & 0 & 0 & 0 & 0 \\ 0 & 0 & -100.0 & 0 & 0 & 0 \\ 0 & 0 & 0 & -100.0 & 0 & 0 \\ 0 & 0 & 0 & 0 & -100.0 & 0 \\ 0 & 0 & 0 & 0 & 0 & -100.0 \end{bmatrix}$
$\hat{D}_2(t_0)$	$\begin{bmatrix} -100.0 & 0 & 0 & 0 & 0 & 0 \\ 0 & -100.0 & 0 & 0 & 0 & 0 \\ 0 & 0 & -100.0 & 0 & 0 & 0 \\ 0 & 0 & 0 & -100.0 & 0 & 0 \\ 0 & 0 & 0 & 0 & -100.0 & 0 \\ 0 & 0 & 0 & 0 & 0 & -100.0 \end{bmatrix}$
$\hat{D}_3(t_0)$	$\begin{bmatrix} -100.0 & 0 & 0 & 0 & 0 & 0 \\ 0 & -100.0 & 0 & 0 & 0 & 0 \\ 0 & 0 & -100.0 & 0 & 0 & 0 \\ 0 & 0 & 0 & -100.0 & 0 & 0 \\ 0 & 0 & 0 & 0 & -100.0 & 0 \\ 0 & 0 & 0 & 0 & 0 & -100.0 \end{bmatrix}$
$\hat{D}_4(t_0)$	$\begin{bmatrix} -100.0 & 0 & 0 & 0 & 0 & 0 \\ 0 & -100.0 & 0 & 0 & 0 & 0 \\ 0 & 0 & -100.0 & 0 & 0 & 0 \\ 0 & 0 & 0 & -100.0 & 0 & 0 \\ 0 & 0 & 0 & 0 & -100.0 & 0 \\ 0 & 0 & 0 & 0 & 0 & -100.0 \end{bmatrix}$
$\hat{D}_5(t_0)$	$\begin{bmatrix} -100.0 & 0 & 0 & 0 & 0 & 0 \\ 0 & -100.0 & 0 & 0 & 0 & 0 \\ 0 & 0 & -100.0 & 0 & 0 & 0 \\ 0 & 0 & 0 & -100.0 & 0 & 0 \\ 0 & 0 & 0 & 0 & -100.0 & 0 \\ 0 & 0 & 0 & 0 & 0 & -100.0 \end{bmatrix}$
$\hat{D}_6(t_0)$	$\begin{bmatrix} -100.0 & 0 & 0 & 0 & 0 & 0 \\ 0 & -100.0 & 0 & 0 & 0 & 0 \\ 0 & 0 & -100.0 & 0 & 0 & 0 \\ 0 & 0 & 0 & -100.0 & 0 & 0 \\ 0 & 0 & 0 & 0 & -100.0 & 0 \\ 0 & 0 & 0 & 0 & 0 & -100.0 \end{bmatrix}$

4.6.1 Experimental Results

Table 4.8: The UV mass and gravitational parameters identified using AID and the IDDAT dataset.

Parameter Symbol	AIDP Values
$\hat{M}(t_f)$	$\begin{bmatrix} 996.9 & -6.166 & 9.118 & 53.64 & -76.78 & 111.7 \\ -6.166 & 1275.0 & 14.23 & -56.45 & 41.07 & -43.3 \\ 9.118 & 14.23 & 1378.0 & -17.57 & 69.42 & 43.95 \\ 53.64 & -56.45 & -17.57 & 308.7 & 21.87 & 39.99 \\ -76.78 & 41.07 & 69.42 & 21.87 & 322.3 & -48.32 \\ 111.7 & -43.3 & 43.95 & 39.99 & -48.32 & 467.4 \end{bmatrix}$
$\hat{g}(t_f)$	-21.77
$\hat{b}(t_f)$	$\begin{bmatrix} 5.966 \\ -0.9802 \\ 342.8 \end{bmatrix}$

The IDDAT dataset was used to identify plant parameters of the 6-DOF plant model (2.44) with both the adaptive identification and least squares algorithms. Tables 4.8 and 4.9 report the adaptively identified parameter set (AIDP) estimated using 6-DOF UV AID (as per Section 4.3). Tables 4.10 and 4.11 report the least squares identified parameter set (LSP) estimated using 6-DOF UV LS (as per Section 4.4). The parameter sets AIDP, LSP, and INITP were used as parameter sets for three 6-DOF UV models; the adaptively identified plant model (AIDPM), the least squares identified plant model (LSPM), and the initialization parameter set plant model (INITPM).

Using the force and torque inputs from the CROSS dataset, Figures 4.5 to 4.7 compare the states from simulations of AIDPM, LSPM, and INITPM to the measured JHU ROV states from the CROSS dataset. Each of these Figures display three minute subsets of 30 minutes of state data generated by driving simulations of AIDPM, LSPM, and INITPM

Table 4.9: The UV drag parameters identified using AID and the IDDAT data.

Parameter Symbol	AIDP Values
$\hat{D}_1(t_f)$	$\begin{bmatrix} -466.7 & 4.902 & -14.54 & -19.92 & -0.3734 & -3.236 \\ 71.43 & -331.6 & -27.36 & 119.8 & -13.05 & 12.08 \\ -67.64 & -1.584 & -528.8 & -11.23 & 42.6 & -22.18 \\ 0.03723 & -12.6 & 97.29 & -270.7 & 19.31 & -56.57 \\ 17.39 & -14.41 & -47.56 & -19.17 & -51.29 & 6.865 \\ -36.24 & 5.508 & -3.391 & 44.59 & -13.47 & -155.7 \end{bmatrix}$
$\hat{D}_2(t_f)$	$\begin{bmatrix} -342.9 & 15.59 & 35.52 & -19.45 & -30.78 & -27.73 \\ -16.96 & -618.6 & 68.14 & 107.7 & -37.52 & 42.93 \\ 7.135 & 19.27 & -578.9 & 19.15 & 49.08 & -21.97 \\ -11.15 & 49.91 & 69.85 & -279.2 & 30.13 & -19.8 \\ 52.72 & -63.28 & -11.81 & -22.2 & -42.57 & 38.04 \\ -31.44 & 43.94 & -40.48 & 77.72 & -16.38 & -150.4 \end{bmatrix}$
$\hat{D}_3(t_f)$	$\begin{bmatrix} -373.0 & 9.072 & 43.92 & -9.852 & -26.69 & 7.863 \\ -12.09 & -466.7 & 6.452 & 138.2 & -11.46 & 67.43 \\ -31.76 & 52.37 & -685.6 & -1.646 & 20.42 & -2.191 \\ -21.4 & 3.283 & 146.3 & -261.8 & 32.96 & -33.43 \\ 4.241 & -32.42 & -17.53 & -30.22 & -56.54 & -11.55 \\ -45.66 & 24.02 & -38.2 & 40.72 & -28.91 & -241.1 \end{bmatrix}$
$\hat{D}_4(t_f)$	$\begin{bmatrix} -292.8 & -10.59 & 35.93 & -8.17 & -18.11 & -25.44 \\ 4.436 & -342.0 & 13.63 & 190.4 & -3.024 & 45.74 \\ 9.531 & -6.416 & -362.0 & -19.08 & 23.41 & -14.81 \\ 2.579 & 32.18 & 62.65 & -207.2 & 16.85 & 2.63 \\ 4.186 & -6.082 & -7.507 & -22.97 & -73.4 & 5.957 \\ 3.196 & 20.58 & 1.016 & 62.8 & -19.93 & -142.3 \end{bmatrix}$
$\hat{D}_5(t_f)$	$\begin{bmatrix} -212.3 & -16.1 & 7.133 & -15.9 & -21.23 & -4.932 \\ 19.71 & -242.1 & -6.173 & 44.77 & -7.459 & 19.94 \\ -9.7 & -17.81 & -248.4 & 0.08174 & 32.39 & -5.403 \\ -2.604 & 11.03 & 39.88 & -162.8 & 24.41 & -9.847 \\ 4.528 & -3.59 & -16.11 & -10.59 & -66.71 & 17.56 \\ -11.06 & -4.563 & 0.2745 & 19.88 & -14.07 & -148.7 \end{bmatrix}$
$\hat{D}_6(t_f)$	$\begin{bmatrix} -398.9 & -8.592 & -25.27 & -11.01 & -43.3 & -25.29 \\ -53.06 & -602.1 & 24.9 & 133.0 & -28.92 & 70.24 \\ 4.612 & -16.02 & -582.0 & -0.02913 & 77.21 & -53.36 \\ -3.501 & 13.71 & 115.5 & -283.3 & 25.63 & -153.0 \\ 11.5 & -44.13 & -35.11 & -25.37 & -41.52 & -18.43 \\ -57.68 & 33.12 & -49.59 & 76.05 & -17.43 & -109.2 \end{bmatrix}$

Table 4.10: The UV mass and gravitational parameters identified using LS and the IDDAT dataset.

Parameter Symbol	LSP Values
$\hat{M}(t_f)$	$\begin{bmatrix} 446.7 & 13.29 & 35.18 & 20.74 & -27.2 & 37.66 \\ 13.29 & 669.5 & -0.2402 & -14.65 & 2.878 & -21.9 \\ 35.18 & -0.2402 & 896.2 & -16.36 & 11.14 & 35.23 \\ 20.74 & -14.65 & -16.36 & 39.53 & -7.008 & 17.43 \\ -27.2 & 2.878 & 11.14 & -7.008 & 65.47 & -2.574 \\ 37.66 & -21.9 & 35.23 & 17.43 & -2.574 & 116.8 \end{bmatrix}$
$\hat{g}(t_f)$	-19.7
$\hat{b}(t_f)$	$\begin{bmatrix} 0.7842 \\ 6.807 \\ 279.8 \end{bmatrix}$

using the torque data from the CROSS dataset. Similar simulations of AIDPM, LSPM, and INITPM were created using the force and torque commands from the IDDAT dataset. Tables 4.12 and 4.13 summarize the MAE between measured and simulated vehicle state for each experimental dataset, 6-DOF UV model, and open-loop-stable DOF.

4.6.2 Analysis of Experimental Results

Figures 4.5 to 4.7 reveal that the ability of a simulated plant model to match experimentally observed plant performance is dependent on the model's plant parameters. Comparing the states produced by simulating AIDPM and LSPM with those from INITPM (a model which uses the arbitrarily chosen INITP parameter set), we see that both experimentally identified models are better at matching experimentally observed dynamic plant behavior.

Table 4.11: The UV drag parameters identified using LS and the IDDAT dataset.

Parameter Symbol	LSP Values
$\hat{D}_1(t_f)$	$\begin{bmatrix} -640.7 & 29.14 & -77.14 & -206.0 & 399.7 & -57.4 \\ 426.7 & -146.6 & -191.1 & -53.18 & 310.4 & -242.6 \\ 50.05 & -65.4 & -1078.0 & 216.5 & 32.88 & -108.7 \\ -2.037 & 35.94 & 4.818 & -557.7 & -19.11 & 58.69 \\ 60.09 & 65.24 & -2.878 & 78.19 & -108.7 & 74.52 \\ -32.74 & 15.27 & -19.89 & -77.99 & 81.52 & -82.61 \end{bmatrix}$
$\hat{D}_2(t_f)$	$\begin{bmatrix} -416.7 & -54.12 & 88.38 & -53.97 & -79.78 & -63.98 \\ -20.42 & -575.1 & 101.8 & -75.27 & -260.0 & 67.67 \\ -25.36 & -75.01 & -979.1 & 429.8 & -130.5 & -45.88 \\ -37.62 & 69.31 & 0.004228 & -318.2 & 73.01 & 16.12 \\ 52.75 & -31.51 & -40.18 & -32.51 & -183.8 & 10.49 \\ -62.16 & -15.68 & -89.55 & 33.62 & 243.3 & -220.9 \end{bmatrix}$
$\hat{D}_3(t_f)$	$\begin{bmatrix} -894.2 & 293.0 & 42.96 & -203.4 & -424.3 & 15.49 \\ -115.2 & -1247.0 & -215.0 & 164.9 & 283.9 & 131.6 \\ -120.7 & 165.4 & -901.3 & 72.91 & -150.7 & 168.2 \\ -25.58 & 84.36 & 195.6 & -318.2 & -40.94 & 26.2 \\ 145.6 & -164.2 & -46.79 & 73.39 & -321.2 & 27.31 \\ -115.2 & 164.7 & -143.7 & -67.74 & -72.01 & -514.8 \end{bmatrix}$
$\hat{D}_4(t_f)$	$\begin{bmatrix} -22.32 & -55.78 & 266.5 & 233.5 & -737.6 & 258.0 \\ -445.6 & -242.8 & 463.0 & 1680.0 & 255.3 & -128.4 \\ 61.74 & -83.5 & -454.2 & -943.5 & -53.48 & -144.2 \\ 45.38 & 149.0 & -167.4 & 235.8 & -10.58 & 40.72 \\ 89.95 & -16.57 & -114.2 & -32.4 & -58.5 & -80.68 \\ -39.36 & -14.35 & 135.3 & 278.7 & -508.8 & -114.7 \end{bmatrix}$
$\hat{D}_5(t_f)$	$\begin{bmatrix} -541.9 & -201.2 & -218.5 & -4.108 & -1155.0 & 338.4 \\ 802.6 & -1098.0 & -648.5 & -353.1 & -46.14 & -232.1 \\ 123.8 & -116.6 & -1045.0 & 209.3 & -203.8 & -111.9 \\ -81.21 & 59.62 & 6.686 & -450.4 & 90.86 & 44.2 \\ 11.35 & 45.01 & 96.38 & -126.6 & 216.3 & 41.87 \\ -41.39 & -1.279 & 223.2 & -8.406 & -221.2 & -42.09 \end{bmatrix}$
$\hat{D}_6(t_f)$	$\begin{bmatrix} -310.2 & 98.97 & -39.83 & 86.85 & 22.8 & -142.3 \\ -172.0 & -730.8 & 113.5 & 166.2 & -560.2 & 266.3 \\ 1.31 & -43.02 & -536.0 & 166.4 & 370.4 & 68.14 \\ -22.85 & 1.085 & 16.88 & -247.2 & -57.23 & -76.39 \\ -28.74 & -68.49 & -109.2 & 28.06 & -310.4 & 17.32 \\ -155.9 & 21.63 & -77.06 & -27.19 & 40.62 & -24.28 \end{bmatrix}$

Table 4.12: mean absolute errors (MAEs) between measured and simulated angular position states for all pairs of 6-DOF UV experiments and 6-DOF UV models.

UV Model	Experiment	Rol	Pit
AIDPM	CROSS	2°	2.1°
LSPM	CROSS	1.38°	1.65°
INITPM	CROSS	9.9°	15.0°
AIDPM	IDDAT	1.96°	2.3°
LSPM	IDDAT	1.30°	1.50°
INITPM	IDDAT	10.0°	15.2°

Table 4.13: mean absolute errors (MAEs) between simulated and measured velocity states for all pairs of 6-DOF UV experiments and 6-DOF UV models.

UV		Translational Velocity			Angular Velocity		
Model	Exp	BodVelX	BodVelY	BodVelZ	AngVelX	AngVelY	AngVelZ
AIDPM	CROSS	0.062m/s	0.058m/s	0.037m/s	1.39°/s	1.35°/s	5.0°/s
LSPM	CROSS	0.050m/s	0.052m/s	0.024m/s	1.38°/s	1.39°/s	6.3°/s
INITPM	CROSS	0.165m/s	0.26m/s	0.25m/s	5.1°/s	3.3°/s	3.9°/s
AIDPM	IDDAT	0.061m/s	0.06m/s	0.039m/s	1.62°/s	1.43°/s	3.4°/s
LSPM	IDDAT	0.045m/s	0.048m/s	0.026m/s	1.58°/s	1.25°/s	4.1°/s
INITPM	IDDAT	0.156m/s	0.27m/s	0.29m/s	6.8°/s	3.4°/s	3.8°/s

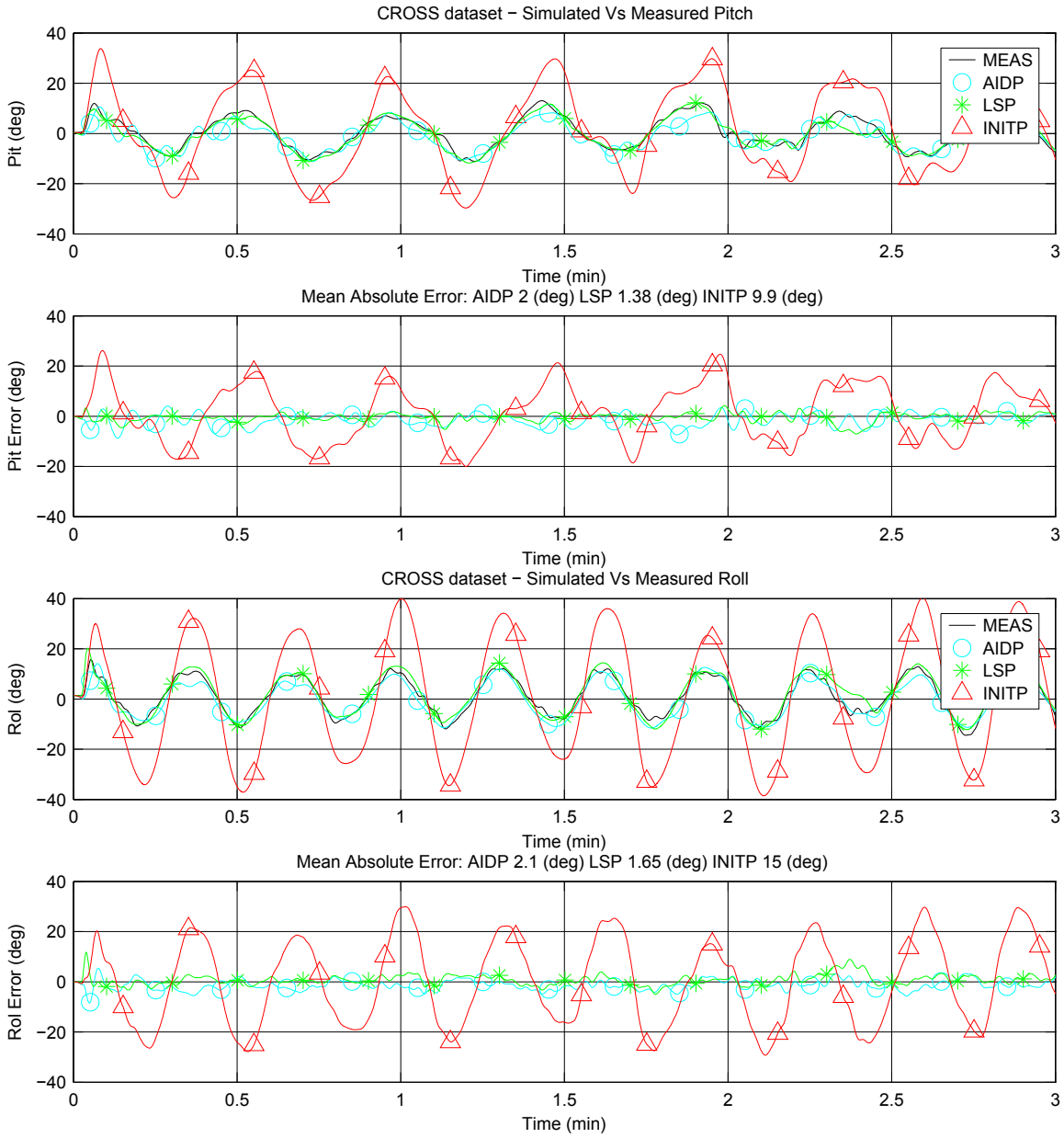

Figure 4.5: Representative data of experimental and simulated JHU ROV states for the CROSS dataset. In the pitch and roll plots, the measured state is plotted together with the simulation state from three model simulations. The states from AIDPM are plotted in blue and marked with circles. The states from LSPM are plotted in green and marked with stars. The states from INITPM are plotted in red and marked with triangles. For each DOF, the error between the measured positions and their estimates is shown.

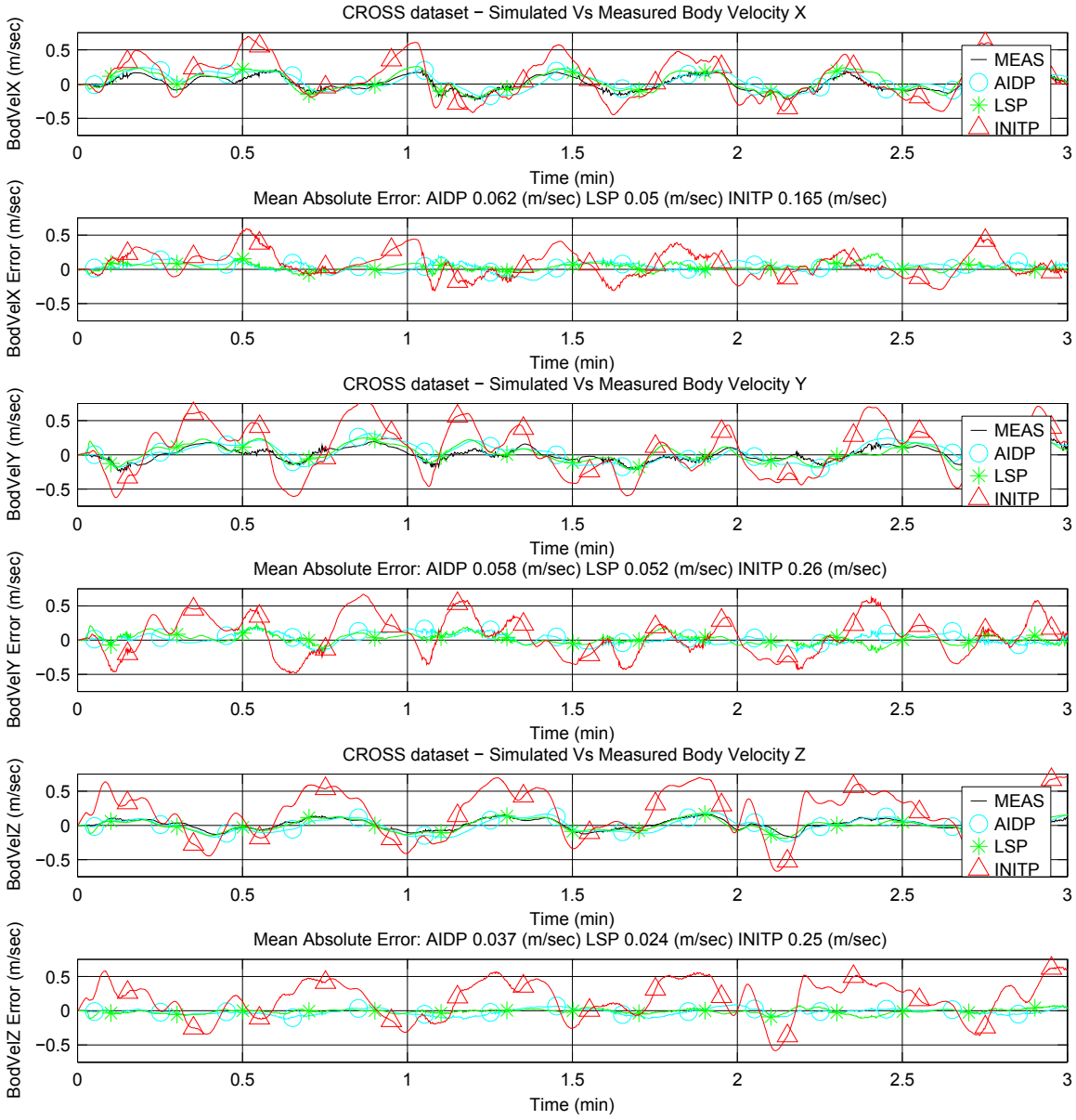

Figure 4.6: Representative data of experimental and simulated JHU ROV states for the CROSS dataset. In the x, y and z body velocity, the measured state is plotted together with the simulation state from three model simulations. The states from AIDPM are plotted in blue and marked with circles. The states from LSPM are plotted in green and marked with stars. The states from INITPM are plotted in red and marked with triangles. For each DOF, the error between the measured positions and their estimates is shown.

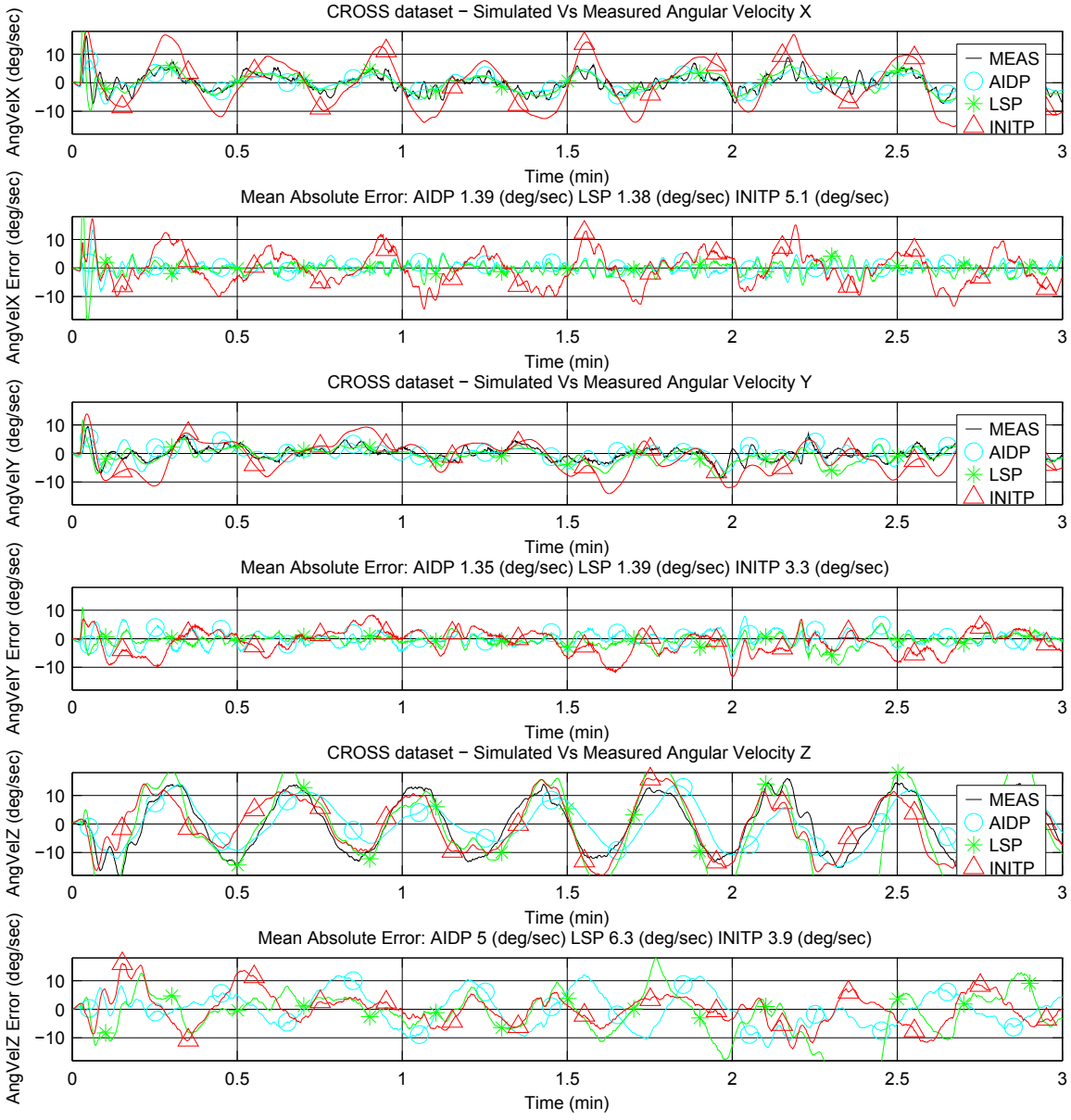

Figure 4.7: Representative data of experimental and simulated JHU ROV states for the CROSS dataset. In the x, y and z angular velocity plots, the measured state is plotted together with the simulation state from three model simulations. The states from AIDPM are plotted in blue and marked with circles. The states from LSPM are plotted in green and marked with stars. The states from INITPM are plotted in red and marked with triangles. For each DOF, the error between the measured positions and their estimates is shown.

Tables 4.12 and 4.13 confirm that the AIDPM and LSPM match JHU ROV performance better than the INITPM.

Tables 4.12 and 4.13 suggest that both identified models provide similar MAE values for the IDDAT dataset. However, since this experiment was used to identify both models, the question arises "How will each model reproduce vehicle performance for experiments not used for model identification?" The rest of this discussion addresses this important question, focusing on which (if any) of the identified models are better at matching JHU ROV performance in cross-validation (as per Appendix A.2). MAE values from comparing simulated and measured states for the CROSS dataset show that modeling the JHU ROV using the least squares identified plant model (LSPM) is marginally better than modeling the JHU ROV using the adaptively identified plant model (AIDPM), as seen in the angular position MAEs in Table 4.12 and translational velocity MAEs in Table 4.13. Both Figure 4.7 and Table 4.13 indicate that the AIDPM and LSPM provide a similar capacity to estimate the JHU ROV's angular velocity. In Figures 4.5 to 4.7 the LSPM and AIDPM accurately reproduce the experimentally observed states, failing only to reproduce the very highest frequency fluctuations observed experimentally (such as those seen in the x angular velocity subplots of Figure 4.7). Taken together Figures 4.5 to 4.7 and Tables 4.12 and 4.13 indicate that the character of JHU ROV performance is captured well by both the LSPM and AIDPM.

4.7 Summary

This Chapter reported two adaptive identification (AID) algorithms for the dynamic estimation of underwater vehicle (UV) plant parameters. The adaptive identification algorithms require the signals of the plant's velocity, position, and external inputs force, but it does not require any specific controller, in contrast to previously reported model-based adaptive tracking controllers. Many underwater vehicle systems do not allow for adaptive tracking controllers because they are under-actuated or have other control constraints. Sections 4.5 and 4.6 report comparative experimental evaluations of the adaptive identification algorithms. Both the least squares identified plant model and adaptively identified plant model were shown to match closely the experimentally observed underwater vehicle input-output behavior. Future work could address less conservative bounds for the initial error in the parameter estimates, characterize more precisely conditions for asymptotic parameter convergence, and compare the relative strengths and weaknesses of adaptive and least squares parameter identification methods.

Chapter 5

Adaptive Model-Based Control of Underwater Vehicles

This Chapter addresses the problem of adaptive model-based trajectory tracking control of underwater vehicles (UVs) for dynamic 6-degree-of-freedom (DOF) motion. The approach employed herein, adaptive model-based control (AMBC), estimates plant parameters during the trajectory-tracking control process. The adaptive controller estimates parameters for a rigid-body plant such as vehicle mass and added hydrodynamic mass parameters; quadratic drag parameters; and gravitational force and buoyancy parameters that arise in the dynamic models of rigid-body UVs. We report a non-adaptive model-based control algorithm for trajectory-tracking control of fully-actuated rigid-body underwater vehicles, its adaptive extension, and mathematical analysis of the stability of the resulting closed-loop systems. We report a comparative experimental evaluation of AMBC and

proportional derivative control (PDC) in full scale vehicle trials utilizing the Johns Hopkins University Hydrodynamic Test Facility and Johns Hopkins University Remotely Controlled Vehicle (JHU ROV) (Appendix A.1). The experimental evaluation shows that AMBC provides better position tracking performance (30%) and marginally worse velocity tracking performance (8%) over PDC. To the best of the authors' knowledge, this is the first experimental comparison of AMBC and PDC UVs during simultaneous motion in all six DOF.

This Chapter is in two parts. Section 5.2 reports a non-adaptive model-based control (MBC) algorithm and an AMBC algorithm for UVs. Section 5.3 reports results indicating that unmodeled thruster dynamics can destabilize parameter adaptation and a two-step AMBC algorithm which is robust to unmodeled thruster dynamics.

The results from Sections 5.2.6 and 5.3 are reported in a paper submitted to the 2014 International Conference on Robotics and Automation [49].

5.1 Literature Review

Adaptive controllers for linear plants are well understood [51]. Adaptive reference trajectory-tracking is well understood for several types of second-order holonomic nonlinear plants whose parameters enter linearly into the plant equations of motion, e.g. robot manipulator arms [17, 59, 63], spacecraft [36, 62], and rigid-body rotational plants [15]. Comparative experimental evaluations of AMBC for robot manipulator arms have been reported, e.g. [53, 69].

The structure of the MBC algorithm reported herein was inspired by the proportional derivative tracking control algorithm for rigid-body motion in free space reported by Bullo and Murray [13]. Our controller can be seen as a specialization of this result for UV control; we use their error coordinate structure with a fully-coupled lumped-parameter plant model of UV dynamics, (2.44). Fully-coupled lumped-parameter plant models for UVs use a finite set of plant parameters which have been shown empirically to be a good approximation for the complex dynamics of a rigid-body and associated fluid-vehicle interaction. Lumped-parameter models of UV dynamics are used in previously reported MBC algorithms. In [18], Fossen summarizes lumped-parameter modeling of UV dynamics and UV MBC using a lumped-parameter modeling and traditional error coordinates. [65] reports and experimentally evaluates single DOF UV MBC algorithms for control of the x, y, depth, and heading DOF. [46] reports and experimentally evaluates a UV MBC algorithm assuming a fully-coupled lumped-parameter model; this comparative experimental evaluation of MBC and PDC included reference trajectories requiring simultaneous motion in all DOF and was conducted using the Johns Hopkins University Hydrodynamic Test Facility (Appendix A).

Previous studies have utilized a lumped-parameter UV models in the development of tracking control algorithms which are robust to model parameter uncertainty. In [72] a sliding mode controller and numerical simulations of performance in X, Y, and heading is reported. In [73] a discrete time parameter adaptation algorithm is reported with a numerical simulation study. In [19] the authors report a hybrid (adaptive and sliding) nonlinear

UV controller which explicitly handles multiplicative uncertainty in the input mapping.

Experimental evaluations of AMBC algorithms have also been reported. Yoerger et al. reported the first experimental evaluation of nonlinear adaptive sliding-mode control on an UV [71]. In [74] an experimental evaluation of UV AMBC performance in the presence of noisy position readings is reported. In [5] an experimental evaluation of an AMBC is reported for simultaneous motion in the translational DOFs. Comparative experimental evaluations of linear controllers, model-based controllers, and their adaptive extensions for UV single DOF motion have been reported [40, 65]. In [75] a comparative experimental evaluation in the presence of a common external disturbance for proportional integral derivative control, disturbance observer control and the adaptive extensions of both is reported. In each of these previously reported experimental evaluations at most two DOF had a non-zero reference velocity at a given moment, and in all cases at most set-point regulation was reported in the pitch and roll DOF.

5.2 Adaptive Model-Based Tracking Control of Underwater Vehicles

Recent advances in enabling technologies for UVs including *in-situ* sensing, power storage, and communication modalities have enabled the development of UVs which can accomplish missions previously thought impractical or impossible. Many of these missions, such as seafloor surveying and environmental monitoring, can depend on tracking a

specified trajectory as closely as possible. To facilitate these missions, novel UV control algorithms may provide improved trajectory-tracking precision. UV MBC has been shown experimentally to provide significant performance gains over PDC [46], however MBC requires model parameters to be known *a priori*. UV adaptive model-based control (AMBC) removes the need for a previously identified model. In this Section we report novel MBC and AMBC algorithms for a fully-coupled UV plant model.

This Section is organized as follows: Sections 5.2.1, 5.2.2, and 5.2.3 present the state representations, UV plant model, and error coordinates used through the rest of this Section. Section 5.2.4 reports a UV MBC algorithm. Section 5.2.5 reports a novel UV AMBC algorithm. Both assume a model of rigid-body UV dynamics parametrized by hydrodynamic mass parameters; quadratic drag parameters; gravitational force and buoyancy parameters. For both results, a local stability proof is reported showing that the vehicle position and velocity states asymptotically converge to the desired reference trajectory. For the AMBC algorithm reported, the parameter estimates are shown to be stable and converge asymptotically to values that provide input-output model behavior identical to that of the actual plant. Section 5.2.6 reports how the MBC and AMBC algorithms reported herein can be used to identify subsets of plant parameters if other parameters are known. This Section also reports a two-step AMBC algorithm shown experimentally in Section 5.3.5 to be robust to actuator modeling errors observed in our experimental vehicle.

This Section omits explicit notation of variable dependence on time except where such dependence is required to discuss the initial condition of a controller.

5.2.1 UV States: Actual and Desired

Throughout this Section we will be concerned with two state trajectories in SE(3): the actual state trajectory of the vehicle and the desired or reference state trajectory of the vehicle. We denote the actual state (i.e. 6-DOF pose and velocity) with the subscript a and denote the desired reference state of the vehicle with d. These states will be represented in three reference frames: states represented in the (assumed inertial) world-frame will be indicated using a leading superscript w, states represented in the actual body-frame will be indicated using a leading superscript a, and states represented in the desired body-frame will be indicated using a leading superscript d. Homogeneous transforms between these different reference frames will use leading superscripts and subscripts to indicate the transform being preformed, for instance the homogeneous matrix ${}^w_a H$, when multiplied by a vector represented in the actual vehicle reference frame, would provide that vector's world reference frame coordinates, e.g. ${}^w x = {}^w_a H {}^a x$. We represent the actual pose of the vehicle in exponential coordinates as $\psi_a \in \mathbb{R}^6$ and the actual velocity of the vehicle as ${}^a v_a \in \mathbb{R}^6$. Note that for ${}^w_a R \in \mathrm{SO}(3)$, the rotation matrix from the actual body-frame to the world-frame, and $p_a \in \mathbb{R}^3$, the position of the vehicle, we have ${}^w_a H = \begin{bmatrix} {}^w_a R & p_a \\ 0_{1\times 3} & 1 \end{bmatrix} = e^{\widehat{\psi_a}}$. Note that for ${}^a \nu_a \in \mathbb{R}^3$, the vehicle's body-frame translational velocity, and ${}^a \omega_a \in \mathbb{R}^3$, the vehicle's body-frame angular velocity, we have the equality ${}^a v_a = \begin{bmatrix} {}^a \nu_a^T & {}^a \omega_a^T \end{bmatrix}^T$. We similarly represent the desired pose and velocity of the vehicle as $\psi_d \in \mathbb{R}^6$ and ${}^d v_d \in \mathbb{R}^6$ with the desired-frame homogeneous matrix, rotation matrix, position, translational

velocity, and angular velocity represented as ${}^w_d H$, ${}^w_d R$, p_d, ${}^d\nu_d$, and ${}^d\omega_d$, respectively.

5.2.2 UV Dynamics

We make the common assumption of modeling a UV as a rigid-body with added hydrodynamic mass, quadratic drag, gravitational force, and buoyancy moving under the influence of external control torques $\tau \in \mathbb{R}^3$ and control forces $f \in \mathbb{R}^3$ applied by the vehicle's thrusters. Section 2.6 presents this second-order finite-dimensional lumped-parameter dynamic model for a fully submerged rigid-body UV, written in the body-frame (2.44). Using the state representation conventions from Section 5.2.1, the model (2.44) can be written as

$$\begin{aligned} {}^w_a \dot{H} &= {}^w_a H \widehat{{}^a v_a} \\ M^a \dot{v}_a &= \mathrm{ad}^T_{{}^a v_a} M^a v_a + \mathcal{D}({}^a v_a) + \mathcal{G}({}^w_a H) + u. \end{aligned} \tag{5.1}$$

where $\mathcal{D}(v) = \sum_{i=1}^{6} |v_i| D_i v$. Note (5.1) is linear in $\{M,\ D,\ g,\ b\}$ and be parametrized by θ_{UV} as defined in (2.48). Further information on the functions, parameters, and state representations of (5.1) are described in Sections 2.2.1 and 2.6.

5.2.3 Error Coordinates

The tracking control algorithms presented herein use the error coordinates ΔH, $\Delta\psi$, Δv, and $\Delta\theta$. We define ΔH as

$$\Delta H = {}^w_d H^{-1} {}^w_a H. \tag{5.2}$$

Note that ΔH is the transform from the actual to desired vehicle frame since $\Delta H = {}^{d}_{w}H {}^{w}_{a}H = {}^{d}_{a}H$. We define the position tracking error ($\Delta\psi$), velocity tracking error (Δv), and parameter error vector ($\Delta\theta$) as, respectively,

$$\Delta\psi = \log_{\mathrm{SE(3)}}(\Delta H), \tag{5.3}$$

$$\Delta v = {}^{a}v_a - {}^{a}v_d, \tag{5.4}$$

$$x = \begin{bmatrix} \Delta\psi \\ \Delta v \end{bmatrix}, \text{ and} \tag{5.5}$$

$$\Delta\theta = \hat{\theta}_{UV} - \theta_{UV} \tag{5.6}$$

where ${}^{a}v_d = \mathrm{Ad}_{\Delta H^{-1}} {}^{d}v_d$ is defined using the adjoint map, $Ad : \mathrm{SE}(3) \to \mathbb{R}^{6\times 6}$ defined in (2.5), which transforms SE(3) velocity vectors between reference frames. Using the fact that $\forall v \in \mathbb{R}^6$ and $\forall H \in \mathrm{SE}(3) \quad H\widehat{v}H^{-1} = \widehat{\mathrm{Ad}_H v}$ the time derivative of ΔH is

$$\begin{aligned}
\Delta\dot{H} =& {}^{w}_{d}H^{-1} {}^{w}_{a}\dot{H} + {}^{w}_{d}\dot{H}^{-1} {}^{w}_{a}H \\
=& \Delta H \widehat{{}^{a}v_a} - \widehat{{}^{d}v_d}\Delta H \\
=& \Delta H \widehat{{}^{a}v_a} - \Delta H \Delta H^{-1} \widehat{{}^{d}v_d} \Delta H \\
=& \Delta H \left({}^{a}v_a - \mathrm{Ad}_{\Delta H^{-1}} {}^{d}v_d \right)\widehat{\ } \\
=& \Delta H \widehat{\Delta v}.
\end{aligned} \tag{5.7}$$

The equality (5.7) implies that

$$\Delta\dot{\psi} = \hat{\mathcal{A}}^{-1}(\Delta\psi)\Delta v \tag{5.8}$$

where $\hat{\mathcal{A}}^{-1} : \mathbb{R}^6 \to \mathbb{R}^{6\times 6}$ is the inverse SE(3) velocity Jacobian. The reader is directed to Appendix B for further information about this Jacobian.

We now develop a useful expression for $\Delta\dot{v}$. Note from (5.4) that $\widehat{\Delta v} = \widehat{{}^a v_a} - \Delta H^{-1}\widehat{{}^d v_d}\Delta H$. Consider the following expression for $\Delta\dot{v}$,

$$\begin{aligned}
\widehat{\Delta\dot{v}} =& \widehat{{}^a\dot{v}_a} - \Delta H^{-1}\widehat{{}^d\dot{v}_d}\Delta H - \Delta\dot{H}^{-1}\widehat{{}^d v_d}\Delta H - \Delta H^{-1}\widehat{{}^d v_d}\Delta\dot{H} \\
=& \widehat{{}^a\dot{v}_a} - \Delta H^{-1}\widehat{{}^d\dot{v}_d}\Delta H + \widehat{\Delta v}\Delta H^{-1}\widehat{{}^d v_d}\Delta H - \Delta H^{-1}\widehat{{}^d v_d}\Delta H\widehat{\Delta v} \\
=& \widehat{{}^a\dot{v}_a} - \widehat{\left(\mathrm{Ad}_{\Delta H^{-1}}\,{}^d\dot{v}_d\right)} + \widehat{\Delta v}\,\widehat{\left(\mathrm{Ad}_{\Delta H^{-1}}\,{}^d v_d\right)} - \widehat{\left(\mathrm{Ad}_{\Delta H^{-1}}\,{}^d v_d\right)}\,\widehat{\Delta v}.
\end{aligned} \tag{5.9}$$

Note that the last two terms (5.9) are the Lie bracket of Δv and ${}^a v_d$. Using the se(3) adjoint operator, $\mathrm{ad} : \mathbb{R}^6 \to \mathbb{R}^{6\times 6}$ defined in (2.4), with $\mathbb{R}^6$ representation of velocities is analytically equivalent to the Lie bracket operation on their $\mathrm{se}(3)$ representations, i.e. $\forall x, y \in \mathbb{R}^6$ we know $\widehat{\mathrm{ad}_x\, y} = \widehat{x}\widehat{y} - \widehat{y}\widehat{x}$. Thus, from (5.9), we have

$$\Delta\dot{v} = {}^a\dot{v}_a - {}^a\dot{v}_d + \mathrm{ad}_{\Delta v}\,{}^a v_d. \tag{5.10}$$

5.2.4 UV MBC

This Section reports a linearizing tracking controller for mechanical plants of the form (5.1). Note that this controller requires exact *a priori* parameter knowledge. A local stability analysis is also included. Section 5.2.4.1 explicitly states the goal for UV MBC. The proof that Theorem 5.2.1 satisfies these conditions is provided in two parts. First, in Section 5.2.4.3, the dynamics of the controlled plant is developed. Then, in Section 5.2.4.4, we

prove the result. Section 5.2.5 reports an adaptive extension to the MBC algorithm reported in this Section.

5.2.4.1 UV MBC Goal

Given a desired reference trajectory $\{{}^{w}_{d}H,\ {}^{d}v_{d},\ {}^{d}\dot{v}_{d}\}$ for a plant of the form (5.1), where the signals $\{{}^{w}_{a}H,\ {}^{a}v_{a},\ u\}$ are accessible and the parameters $\{M,\ D,\ g,\ b\}$ are known, our goal is to develop a control law $u\ :\ \mathrm{SE}(3)\times\mathbb{R}^6\times\mathrm{SE}(3)\times\mathbb{R}^6\times\mathbb{R}^6\ \rightarrow\ \mathbb{R}^6$ which guarantees that all signals remain bounded and provides asymptotically exact reference trajectory tracking, i.e. $\lim_{t\to\infty}\Delta\psi(t)=\vec{0}$ and $\lim_{t\to\infty}\Delta v(t)=\vec{0}$.

5.2.4.2 UV MBC Theorem

Theorem 5.2.1 *For plants of the form (5.1), when the plant parameters $\{M,D,g,b\}$ are known, the control law*

$$u\left({}^{w}_{a}H,{}^{a}v_{a},{}^{w}_{d}H,{}^{d}v_{d},{}^{d}\dot{v}_{d}\right)=-(k_p\hat{\mathcal{A}}^{-T}(\Delta\psi)+k_d\Delta v)+\mathbb{W}_{MBC}({}^{a}\dot{v}_{d},\Delta v,{}^{a}v_{d},{}^{w}_{a}H)\theta_{UV},\tag{5.11}$$

where the regressor matrix $\mathbb{W}_{MBC}:\mathbb{R}^6\times\mathbb{R}^6\times\mathbb{R}^6\times\mathrm{SE}(3)\rightarrow\mathbb{R}^{6\times 241}$ is defined such that

$$\mathbb{W}_{MBC}({}^{a}\dot{v}_{d},\Delta v,{}^{a}v_{d},{}^{w}_{a}H)\theta_{UV}=M{}^{a}\dot{v}_{d}-M\,\mathrm{ad}_{\Delta v}\,{}^{a}v_{d}-\mathrm{ad}^{T}_{{}^{a}v_{a}}M{}^{a}v_{a}-\mathcal{D}({}^{a}v_{a})-\mathcal{G}({}^{w}_{a}H),\tag{5.12}$$

provides asymptotically stable trajectory tracking in the sense of Lyapunov, i.e. $\lim_{t\to\infty}\Delta\psi(t)=\vec{0}$ and $\lim_{t\to\infty}\Delta v(t)=\vec{0}$, if the following conditions are met:

- *the signals* $\{{}^{w}_{d}H, {}^{d}v_d, {}^{d}\dot{v}_d\} \in \{\mathrm{SE}(3), \mathbb{R}^6, \mathbb{R}^6\}$ *are continuous and bounded*
- $k_d,\ k_p \in \mathbb{R}_+$
- $\|x(t_0)\| < \sqrt{\frac{\epsilon\lambda_{12}}{\epsilon\lambda_1}}\pi$ *for the state error vector* x *defined in (5.5)*

where, as per the eigenvalue ordering conventions from Section 2.2.2, ${}_{\epsilon}\lambda_i$ *are the eigenvalues of* $\mathcal{M}_\epsilon$ *from (5.19).*

5.2.4.3 UV MBC Controlled Plant

The controlled plant is of the form

$$\begin{aligned} M^a\dot{v}_a =& \operatorname{ad}^T_{{}^a v_a} M^a v_a + \mathcal{D}({}^a v_a) + \mathcal{G}({}^w_a H) - (k_p\hat{\mathcal{A}}^{-T}(\Delta\psi) + k_d\Delta v) \\ &+ \mathbb{W}_{MBC}({}^a\dot{v}_d, \Delta v, {}^a v_d, {}^w_a H)\theta_{UV} \\ =& M^a\dot{v}_d - M\operatorname{ad}_{\Delta v}{}^a v_d - (k_p\hat{\mathcal{A}}^{-T}(\Delta\psi) + k_d\Delta v) \end{aligned} \tag{5.13}$$

From (5.10) we get

$$M\Delta\dot{v} = -(k_p\hat{\mathcal{A}}^{-T}(\Delta\psi) + k_d\Delta v). \tag{5.14}$$

Using the system error vector $x \in \mathbb{R}^{12}$ defined in (5.5) as

$$x = \begin{bmatrix} \Delta\psi \\ \\ \Delta v \end{bmatrix} \tag{5.15}$$

and the matrix valued function $\hat{\mathbb{A}} : \mathbb{R}^6 \to \mathbb{R}^{12} \times \mathbb{R}^{12}$ defined as

$$\hat{\mathbb{A}}(\Delta\psi) = \begin{bmatrix} 0_{6\times 6} & \hat{\mathcal{A}}^{-1}(\Delta\psi) \\ \\ -k_p M^{-1}\hat{\mathcal{A}}^{-T}(\Delta\psi) & -k_d M^{-1} \end{bmatrix} \tag{5.16}$$

then from (5.8), (5.14), (5.5), and (5.16) we see that the equation for the error dynamics of the system is

$$\dot{x} = \hat{\mathbb{A}}(\Delta\psi)x. \tag{5.17}$$

5.2.4.4 UV MBC Stability Proof

Consider the following Lyapunov function candidate

$$V_1(t) = \frac{1}{2}x^T \mathcal{M}_\epsilon x \tag{5.18}$$

where

$$\mathcal{M}_\epsilon = \begin{bmatrix} k_p\mathbb{I}_{6\times 6} & \epsilon M \\ \epsilon M & M \end{bmatrix}. \tag{5.19}$$

Consider that $\forall x$

$$V_1(t) \geq \frac{1}{2}\begin{bmatrix} \|\Delta\psi\| & \|\Delta v\| \end{bmatrix}\begin{bmatrix} k_p & -\epsilon\lambda_1 \\ -\epsilon\lambda_1 & \lambda_6 \end{bmatrix}\begin{bmatrix} \|\Delta\psi\| \\ \|\Delta v\| \end{bmatrix} \tag{5.20}$$

where $\begin{bmatrix} k_p & -\epsilon\lambda_1 \\ -\epsilon\lambda_1 & \lambda_6 \end{bmatrix}$ is positive definite symmetric (PDS) if

$$\epsilon \leq \sqrt{\frac{k_p\lambda_6}{\lambda_1^2}}. \tag{5.21}$$

Thus

- $V_1(t)$ is positive definite and
- $V_1(t)$ is equal to zero if and only if $x = \vec{0}$.

The time derivative of (5.18) is

$$\dot{V}_1(t) = \frac{1}{2}x^T \left(\hat{\mathbb{A}}^T(\Delta\psi)\mathcal{M}_\epsilon + \mathcal{M}_\epsilon \hat{\mathbb{A}}(\Delta\psi) \right) x. \tag{5.22}$$

Note that $\exists c \in \mathbb{R}_+$ for which $\|\hat{\mathcal{A}}^{-1}(\psi)x\| \leq c\|x\| \quad \forall \psi \in \mathbb{R}^6$ such that $\|\psi\| < \pi$ (See Appendix B.2). Therefore $\forall \Delta\psi$ such that $\|\Delta\psi\| < \pi$ we have

$$\Delta v^T \left(\hat{\mathcal{A}}^{-T}(\Delta\psi)M + M\hat{\mathcal{A}}^{-1}(\Delta\psi) \right) \Delta v \leq 2\lambda_1 c \|\Delta v\|^2. \tag{5.23}$$

Using this bound and the equality $\Delta\psi^T \left(\hat{\mathcal{A}}^{-T} + \hat{\mathcal{A}}^{-1} \right) \Delta\psi = \Delta\psi^T \Delta\psi$ (shown in Appendix B.1), we have

$$\begin{aligned}
\dot{V}_1(t) =& \frac{1}{2}x^T \begin{bmatrix} -\epsilon k_p \left(\hat{\mathcal{A}}^{-T} + \hat{\mathcal{A}}^{-1} \right) & -\epsilon k_d \mathbb{I}_{6\times 6} \\ -\epsilon k_d \mathbb{I}_{6\times 6} & \left(\hat{\mathcal{A}}^{-T}M + M\hat{\mathcal{A}}^{-1} \right) - 2k_d \mathbb{I}_{6\times 6} \end{bmatrix} x \\
=& \frac{1}{2}x^T \begin{bmatrix} -\epsilon 2k_p \mathbb{I}_{6\times 6} & -\epsilon k_d \mathbb{I}_{6\times 6} \\ -\epsilon k_d \mathbb{I}_{6\times 6} & \left(\hat{\mathcal{A}}^{-T}M + M\hat{\mathcal{A}}^{-1} \right) - 2k_d \mathbb{I}_{6\times 6} \end{bmatrix} x \\
\leq & -\epsilon k_p \|\Delta\psi\|^2 + \epsilon k_d \|\Delta\psi\| \|\Delta v\| + \frac{\epsilon}{2}\lambda_1 c \|\Delta v\|^2 - k_d \|\Delta v\|^2 \\
\leq & \frac{1}{2} \begin{bmatrix} \|\Delta\psi\| & \|\Delta v\| \end{bmatrix} \begin{bmatrix} -\epsilon 2k_p & \epsilon k_d \\ \epsilon k_d & \epsilon\lambda_1 c - 2k_d \end{bmatrix} \begin{bmatrix} \|\Delta\psi\| \\ \|\Delta v\| \end{bmatrix}.
\end{aligned} \tag{5.24}$$

$\forall \Delta\psi$ such that $\|\Delta\psi\| < \pi$. Since $\begin{bmatrix} -\epsilon 2k_p & \epsilon k_d \\ \epsilon k_d & \epsilon\lambda_1 c - 2k_d \end{bmatrix}$ is negative definite symmetric if

$$\epsilon \leq \frac{4k_p k_d}{2\lambda_1 k_p c + k_d^2}, \tag{5.25}$$

and $\dot{V}_1(t)$ is negative definite if this condition on ϵ. We are free to choose ϵ such that $\epsilon \leq \min\left(\frac{4k_p k_d}{2\lambda_1 k_p c + k_d^2}, \sqrt{\frac{k_p \lambda_6}{\lambda_1^2}} \right)$, thus we conclude that the system is locally asymptotically

stable, i.e. $\lim_{t\to\infty} \Delta\psi(t) = \vec{0}$ and $\lim_{t\to\infty} \Delta v(t) = \vec{0}$.

This result is local because we require $\|\Delta\psi(t)\| < \pi \quad \forall t \geq t_0$. To justify this assumption note that $\forall t \in \mathbb{R}$ we know $\|\Delta\psi(t)\| \leq \|x(t)\|$ and consider the condition $\|x(t_0)\| < \sqrt{\frac{{}_\epsilon\lambda_{12}}{{}_\epsilon\lambda_1}}\pi$. Since ${}_\epsilon\lambda_{12} \leq {}_\epsilon\lambda_1$, this condition implies $\|x(t_0)\| < \pi$. By the Lyapunov stability proof above, $V_1(t) \leq V_1(t_0)$ for all $t \geq t_0$, thus

$$\begin{aligned}
{}_\epsilon\lambda_{12}\|x(t)\|^2 \leq & x(t)^T \mathcal{M}_\epsilon x(t) \\
\leq & V_1(t) \\
\leq & V_1(t_0) \\
\leq & x(t_0)^T \mathcal{M}_\epsilon x(t_0) \\
\leq & {}_\epsilon\lambda_1 \|x(t_0)\|^2 \\
< & {}_\epsilon\lambda_1 \left(\sqrt{\frac{{}_\epsilon\lambda_{12}}{{}_\epsilon\lambda_1}}\pi \right)^2 .
\end{aligned} \tag{5.26}$$

This inequality implies $\|\Delta\psi(t)\| \leq \|x(t)\| < \pi$ for all $t \geq t_0$. The assumption is justified and local asymptotic stability is proven.

5.2.5 UV AMBC

This Section reports a nonlinear novel linearizing tracking controller for mechanical plants of the form (5.1) without requiring perfect knowledge of the plant parameters. A local stability analysis is also included. Section 5.2.5.1 explicitly states the goal for UV MBC. The proof that Theorem 5.2.2 satisfies these conditions is presented in Section 5.2.5.3. This result is an adaptive extension of the MBC algorithm reported in Section

5.2.4.

5.2.5.1 UV AMBC Goal

Given a desired reference trajectory $\{{}^{w}_{d}H,\ {}^{d}v_d,\ {}^{d}\dot{v}_d\}$ for a plant of the form (5.1), where the signals $\{{}^{w}_{a}H,\ {}^{a}v_a,\ u\}$ are accessible and the parameters $\{M,\ D,\ g,\ b\}$ are constant but unknown, our goal is to develop a control law $u : \mathrm{SE}(3) \times \mathbb{R}^6 \times \mathrm{SE}(3) \times \mathbb{R}^6 \times \mathbb{R}^6 \times \mathbb{R}^{241} \to \mathbb{R}^6$ and parameter update law $\dot{\hat{\theta}}_{UV} : \mathrm{SE}(3) \times \mathbb{R}^6 \times \mathrm{SE}(3) \times \mathbb{R}^6 \times \mathbb{R}^6 \to \times \mathbb{R}^{241}$ which guarantee that all signals remain bounded and provide asymptotically exact reference trajectory-tracking, i.e. $\lim_{t\to\infty} \Delta\psi(t) = \vec{0}$ and $\lim_{t\to\infty} \Delta v(t) = \vec{0}$.

5.2.5.2 UV AMBC Theorem

Theorem 5.2.2 *For plants of the form (5.1) where the plant parameters, $\theta_{UV} \in \mathbb{R}^{241}$, are unknown and the regressor matrix, $\mathbb{W}_{MBC} : \mathbb{R}^6 \times \mathbb{R}^6 \times \mathbb{R}^6 \times \mathrm{SE}(3) \to \mathbb{R}^{6\times 241}$, is defined in (5.12), the control and parameter update laws*

$$u({}^{w}_{a}H, {}^{a}v_a, {}^{w}_{d}H, {}^{d}v_d, {}^{d}\dot{v}_d, \hat{\theta}_{UV}) = -\left(k_p \hat{\mathcal{A}}^{-T}(\Delta\psi) + k_d \Delta v\right) + \mathbb{W}_{MBC}({}^{a}\dot{v}_d, \Delta v, {}^{a}v_d, {}^{w}_{a}H)\hat{\theta}_{UV} \tag{5.27}$$

$$\dot{\hat{\theta}}_{UV}({}^{w}_{a}H, {}^{a}v_a, {}^{w}_{d}H, {}^{d}v_d, {}^{d}\dot{v}_d) = -K_\theta \mathbb{W}^{T}_{MBC}({}^{a}\dot{v}_d, \Delta v, {}^{a}v_d, {}^{w}_{a}H)(\epsilon\Delta\psi + \Delta v) \tag{5.28}$$

provide asymptotically stable trajectory-tracking in the sense of Lyapunov, i.e. $\lim_{t\to\infty} \Delta\psi(t) = \vec{0}$ and $\lim_{t\to\infty} \Delta v(t) = \vec{0}$, and parameter estimates which converge to constant values, i.e. $\lim_{t\to\infty} \dot{\hat{\theta}}(t) = 0_{241\times 1}$, if the following conditions are met:

- *the signals* $\{{}^w_d H, {}^d v_d, {}^d \dot{v}_d\} \in \{\mathrm{SE}(3), \mathbb{R}^6, \mathbb{R}^6\}$ *are continuous and bounded*
- $k_d,\ k_p \in \mathbb{R}_+$
- K_θ *is PDS*
- $\epsilon < \min\left(\frac{4k_p k_d}{2\lambda_1 k_p c + k_d^2}, \sqrt{\frac{k_p \lambda_6}{\lambda_1^2}}\right)$
- $\sqrt{\frac{\epsilon\lambda_1}{\epsilon\lambda_{12}}\|x(t_0)\|^2 + \frac{k_\theta}{\epsilon\lambda_{12}}\|\Delta\theta(t_0)\|^2} < \pi$ *for the state error vector (5.5) and parameter error vector (5.6)*

where $k_\theta = \frac{1}{\min \mathrm{eig}\, K_\theta}$, ${}_\epsilon\lambda_i$ *are the eigenvalues of* $\mathcal{M}_\epsilon$, *and* λ_i *are the eigenvalues of* M *(noting the eigenvalue conventions from Section 2.2.2).*

5.2.5.3 UV AMBC Stability Proof

The controlled plant equation takes the form

$$\begin{aligned}
M^a \dot{v}_a =& \mathrm{ad}^T_{{}^a v_a} M^a v_a + \mathcal{D}({}^a v_a) + \mathcal{G}({}^w_a H) \\
&- (k_p \hat{\mathcal{A}}^{-T}(\Delta\psi) + k_d \Delta v) + \mathbb{W}_{MBC}({}^a\dot{v}_d, \Delta v, {}^a v_d, {}^w_a H)\hat{\theta}_{UV} \\
=& \mathrm{ad}^T_{{}^a v_a} M^a v_a + \mathcal{D}({}^a v_a) + \mathcal{G}({}^w_a H) - (k_p \hat{\mathcal{A}}^{-T}(\Delta\psi) + k_d \Delta v) \\
&+ \mathbb{W}_{MBC}({}^a\dot{v}_d, \Delta v, {}^a v_d, {}^w_a H)\,(\Delta\theta_{UV} + \theta) \\
=& M^a \dot{v}_d - M\,\mathrm{ad}_{\Delta v}\,{}^a v_d - (k_p \hat{\mathcal{A}}^{-T}(\Delta\psi) + k_d \Delta v) + \mathbb{W}_{MBC}({}^a\dot{v}_d, \Delta v, {}^a v_d, {}^w_a H)\Delta\theta.
\end{aligned} \tag{5.29}$$

From equation (5.10) we have

$$M\Delta\dot{v} = -(k_p \hat{\mathcal{A}}^{-T}(\Delta\psi) + k_d \Delta v) + \mathbb{W}_{MBC}({}^a\dot{v}_d, \Delta v, {}^a v_d, {}^w_a H)\Delta\theta \tag{5.30}$$

which provides the error system

$$\dot{x} = \hat{\mathbb{A}}(\Delta\psi)x + \begin{bmatrix} 0_{6\times 1} \\ M^{-1}\mathbb{W}_{MBC}({}^a\dot{v}_d, \Delta v, {}^a v_d, {}^w_a H)\Delta\theta \end{bmatrix}. \tag{5.31}$$

Consider the following candidate Lyapunov equation

$$\begin{aligned} V_2(t) =& \frac{1}{2}x^T\mathcal{M}_\epsilon x + \frac{1}{2}\Delta\theta^T K_\theta^{-1}\Delta\theta \\ =& V_1(t) + \frac{1}{2}\Delta\theta^T K_\theta^{-1}\Delta\theta. \end{aligned} \tag{5.32}$$

Since we assume $\epsilon \leq \sqrt{\frac{k_p\lambda_6}{\lambda_1^2}}$ and K_θ is PDS; we know $V_2(t)$ is positive definite and equal to zero if and only if $x = \vec{0}$ and $\Delta\theta = \vec{0}$. The time derivative of $V_2(t)$ is

$$\begin{aligned} \dot{V}_2(t) = &\frac{1}{2}x^T\left(\hat{\mathbb{A}}^T(\Delta\psi)\mathcal{M}_\epsilon + \mathcal{M}_\epsilon\hat{\mathbb{A}}(\Delta\psi)\right)x + \Delta\theta^T K_\theta^{-1}\Delta\dot{\theta} + \\ &\Delta\theta^T\begin{bmatrix} \epsilon\mathbb{W}_{MBC}^T({}^a\dot{v}_d, \Delta v, {}^a v_d, {}^w_a H) & \mathbb{W}_{MBC}^T({}^a\dot{v}_d, \Delta v, {}^a v_d, {}^w_a H) \end{bmatrix} x. \end{aligned} \tag{5.33}$$

Using the update law (5.28) results in

$$\begin{aligned} \dot{V}_2(t) =& \frac{1}{2}x^T\left(\hat{\mathbb{A}}^T(\Delta\psi)\mathcal{M}_\epsilon + \mathcal{M}_\epsilon\hat{\mathbb{A}}(\Delta\psi)\right)x \\ =& \dot{V}_1(t). \end{aligned} \tag{5.34}$$

As with (5.24), if $\epsilon < \min\left(\frac{4k_pk_d}{2\lambda_1k_pc+k_d^2}, \sqrt{\frac{k_p\lambda_6}{\lambda_1^2}}\right)$ and $\|\Delta\psi\| < \pi$ we know $\dot{V}_2(t) < 0 \quad \forall t \geq t_0$. Therefore $\dot{V}_2$ is negative definite in x and negative semidefinite in $\Delta\theta$ assuming $\|\Delta\psi(t)\| < \pi \quad \forall t \geq t_0$ (a fact shown at the end of this Section). By Lyapunov's direct method, (5.32) and (5.34) imply that all error coordinates are bounded and stable. The structure of $\dot{V}_2(t)$ implies that $x \in \mathcal{L}_2$ or, equivalently, $\lim_{t\to\infty}\left(\int_0^t x^T x\right)^{1/2} < \infty$. We must ensure every signal in (5.31) and (5.28) is bounded and (5.27) well defined for all

time. The facts that ψ_d, $\Delta\psi$, ${}^d v_d$, Δv, ${}^d \dot{v}_d$, and $\Delta\theta$ are bounded, θ_{UV} is constant, and (5.3)-(5.6) imply that ψ_a, ${}^a v_a$, and $\hat{\theta}_{UV}$ are bounded. If $\|\Delta\psi(t)\| < \pi$ then $\hat{\mathcal{A}}^{-1}$, and therefore $\hat{\mathbb{A}}$, is bounded. Since every signal in (5.31) is bounded we know $\dot{x}$ is bounded. Note that bounded $\dot{x}$ and $x \in \mathcal{L}_2$ implies $\lim_{t\to\infty} x = \vec{0}$. Since every signal in (5.28) being bounded and $\lim_{t\to\infty} x = \vec{0}$ implies that $\lim_{t\to\infty} \dot{\hat{\theta}} = \vec{0}$. Thus local stability of the system is shown, the UV state asymptotically converges to the desired reference trajectory, and the estimated parameters converge to constant values.

Above we require $\|\Delta\psi(t)\| < \pi \quad \forall t \geq t_0$. To justify this assumption consider that the inequality

$$\begin{aligned} {}_\epsilon\lambda_{12}\|x(t)\|^2 \leq & x(t)^T \mathcal{M}_\epsilon x(t) \\ \leq & V_2(t) \\ \leq & V_2(t_0) \\ \leq_\epsilon & \lambda_1\|x(t_0)\|^2 + k_\theta\|\Delta\theta(t_0)\|^2 \end{aligned} \tag{5.35}$$

and the final condition from Theorem 5.2.2 imply that $\|x(t)\| < \pi$ for all $t \geq t_0$, guaranteeing that $\|\Delta\psi(t)\| < \pi$ for all $t \geq t_0$.

5.2.6 Two-Step AMBC

In the sequel we will find it convenient to adaptively identify subsets of plant parameters. Note that (5.12) is linear in the parameters, thus there exists a set of functions

$\mathbb{W}_{MBC_i} : \mathbb{R}^6 \times \mathbb{R}^6 \times \mathbb{R}^6 \times \mathrm{SE}(3) \to \mathbb{R}^6$ such that

$$\sum_{i=1}^{241} \mathbb{W}_{MBC_i}({}^a\dot{v}_d, \Delta v, {}^a v_d, {}^w_a H)\theta_{UV_i} = \mathbb{W}_{MBC}({}^a\dot{v}_d, \Delta v, {}^a v_d, {}^w_a H)\theta_{UV}. \tag{5.36}$$

If a subset of parameter values in θ_{UV} is known *a priori* then, based on Theorems 5.2.1 and 5.2.2, an AMBC can be developed to estimate the remaining unknown parameters. Any AMBCs of this form achieve asymptotically exact trajectory-tracking canceling the contribution to vehicle dynamics due to known parameters (as shown in Section 5.2.1) and use parameter update laws to adaptively estimate of the unknown parameters (as shown in Section 5.2.2). If K_θ is assumed to be diagonal, each AMBC of this form will be equivalent to using the AMBC from Theorem 5.2.2, with each known parameter initialized to its known value and its associated parameter gain within K_θ set to zero. A two-step AMBC algorithm presented herein independently estimates two disparate sets of parameters in two successive experimental trials.

The structure of (5.1) allows the identification of dynamic and gravitational parameters to be conducted in a two-step process. The first step is identifying g and b estimates during quasi-static motion in pitch and roll. For quasi-static motion (i.e. nearly zero velocity and acceleration) in these DOF, the following model is sufficient to describe vehicle dynamics

$$0 = \mathcal{G}({}^w_a H) + u \tag{5.37}$$

where all inertial and drag terms are assumed to be negligible because they are either quadratic in velocity or linear in acceleration. The validity of this model implies using the adaptive tracking controller from Theorem 5.2.2 to track a slow reference trajectory in

pitch and roll will identify estimates of g and b without requiring the simultaneous estimation of mass and drag parameters.

The second step AMBC algorithm estimates the inertial and drag parameters (i.e. M and D) while using the gravitational parameter values identified in step one. Using the controller from Theorem 5.2.2 with constant $\hat{b}$ and $\hat{g}$ set to their previously identified values, this controller can be used to track any reference trajectory while identifying estimates of the vehicle's mass and drag. This partitioning of the parameter identification process will be important in the sequel when we consider the effects of unmodeled thruster dynamics on AMBC.

5.3 Experimental Evaluation of UV AMBC with Unmodeled Actuator Dynamics

This Section reports a comparative experimental evaluation between UV AMBC and UV PDC for typical operational maneuvers. Although experimental implementations of UV AMBC algorithms have been reported [5, 40, 65, 71, 74, 75], to the best of our knowledge experimental evaluations of AMBC during simultaneous motion in all DOF has not previously been reported. The comparative experimental evaluation of AMBC and PDC during simultaneous 6-DOF maneuvers reported herein shows that AMBC can provide better position tracking performance than PDC.

This Section is organized as follows: Section 5.3.2 shows how direct implementation of

the AMBC from Theorem 5.2.2 exhibits unstable parameter adaptation in the presence of unmodeled thrust reversal dynamics. Section 5.3.4 presents two experiments where AMBC is used to follow a pitch-only reference trajectory. The range of motion is changed such that one pitch-only reference trajectory requires thrust reversals and the other pitch-only reference trajectory does not. A comparative analysis of these parameter adaption processes details how unmodeled dynamics arising from thrust reversals can cause unstable parameter adaptation. Finally, Section 5.3.5 reports an experimental evaluation of the two-step AMBC algorithm reported in Section 5.2.6, and an experimental comparison of two-step AMBC and PDC.

5.3.1 Experimental Setup

We employed the Johns Hopkins University Hydrodynamic Test Facility (Appendix A) to evaluate UV AMBC. To compare the trajectory-tracking performance of controllers we consider the mean normal of error vectors (MNE) for vectors such as the position error ($\Delta\psi$) and velocity error (Δv). We also report the mean absolute error (MAE) between the measured and reference values for the 12 position and velocity signals. A smaller MNE or MAE value means the controller is doing a better job tracking the reference trajectory. As with the adaptively identified UV models in Sections 4.5 and 4.6, identified UV models are evaluated by error between simulated model performance and the experimentally observed performance. MAE values between the simulated plant states and experimentally measured states are reported. Appendix A provides further details about our hydrodynamic

test facility and algorithm evaluation methods.

The fully-coupled model of UV dynamics used in (5.1) requires 241 independent parameter values. To simplify and clarify the experimental analysis of UV AMBC in the presence of unmodeled thruster dynamics, we have implemented a controller which employs an uncoupled model using 16 scalar terms: 6 hydrodynamic mass, 6 quadratic drag terms (one for each DOF which we will label as m_i and d_i respectively), and the 4 gravitational parameters g and b. For a diagonal parameter adaptation gain matrix K_θ, we can label the individual mass parameter gains as γ_{m_i}, the individual drag parameter gains as γ_{d_i}, the individual buoyancy parameter gains as γ_{b_i} and the gravitational parameter gain as γ_g. Both the AMBC control process and parameter update process where implemented as a discrete time approximation of the continuous time algorithm. Every 100ms the commanded torque and commanded force were recalculated using (5.27) as well as the most recent state measurements, reference state values, and parameter estimates. These inputs signals are therefore piecewise constant. Euler integration of (5.28) for 100ms time steps provided the time series of parameter estimates. The 100ms JHU ROV control system cycle period is one to two orders-of-magnitude smaller than the JHU ROV state variation rate of 1 second or greater observed during dynamic operation. In practice the discrete time approximations were seen to provide similar performance to the continuous time algorithm implemented in simulation.

Sinusoidal reference trajectories are used in this study. Table 5.1 lists the frequencies and amplitudes for the 6-DOF reference trajectories used.

Table 5.1: Reference Trajectory Information

		RefTraj1	RefTraj2
Reference Trajectory Purpose		Trajectory Control Evaluation	Parameter Cross-Validation
DOF world x	*Excitation*	*Trajectory-Tracking*	
	Cos Freq	0.242 rad/sec	0.185 rad/sec
	Cos Amp	0.50 m	0.50 m
DOF world y	*Excitation*	*Trajectory-Tracking*	
	Cos Freq	0.210 rad/sec	0.286 rad/sec
	Cos Amp	0.50 m	0.50 m
DOF world z	*Excitation*	*Trajectory-Tracking*	
	Cos Freq	0.185 rad/sec	0.242 rad/sec
	Cos Amp	0.30 m	0.30 m
DOF roll	*Excitation*	*Trajectory-Tracking*	*Torque Input*
	Cos Frequency	0.5 rad/sec	0.55 rad/sec
	Cos Amplitude	6.9°	35 N m
DOF pitch	*Excitation*	*Trajectory-Tracking*	*Torque Input*
	Cos Freq	0.6 rad/sec	0.65 rad/sec
	Cos Amp	8.6°	30 N m
DOF heading	*Excitation*	*Trajectory-Tracking*	
	Cos Freq	0.210 rad/sec	0.0824 rad/sec
	Cos Amp	135°	135°

5.3.2 UV AMBC Instability During 6-DOF Motion

This Section reports an experimental evaluation of AMBC during simultaneous motion in all DOF which results in unstable parameter adaptation. In the experiment the mass, drag, and gravitational terms were initialized to parameters previously identified to model vehicle performance (tabulated in Tables 5.4 and 5.5). The reference trajectory specified was RefTraj1 from Table 5.1. The gains used were $k_p = 300$, $k_d = 100$ $\gamma_{m_i} = 1000$, $\gamma_{d_i} = 5000$, $\gamma_g = \gamma_{b_1} = \gamma_{b_2} = 0.5$ and $\gamma_{b_3} = 10.0$.

Tables 5.2 and 5.3 tabulate the initial and final parameters identified. Over this two-hour duration experiment most parameter values oscillated near their previously identified values, however $\hat{b}_3(t)$, $\hat{m}_4(t)$, and $\hat{m}_5(t)$ adapted away from their previously identified values. As seen in Figure 5.1, these mass estimates adapt to physically unrealistic negative values and show no signs of asymptotic behavior. The instability observed in this experiment motivated us to examine the role of unmodeled thruster dynamics in the $\hat{m}_4(t)$ and $\hat{m}_5(t)$ adaptation process.

Table 5.2: Gravitational Parameters Identified During Unstable Parameter Adaptation

	g	b_1	b_2	b_3
	N	*N m*	*N m*	*N m*
Init	3.63	1.017	3.02	300
Final	-5.71	2.6	3.53	261

Table 5.3: Mass and Drag Parameters Identified During Unstable Parameter Adaptation

	$m_i(t_o)$	$m_i(t_f)$	$d_i(t_o)$	$d_i(t_f)$
Trans X DOF	583 kg	583 kg	-1245 $\frac{N\,s^2}{m^2}$	-1005 $\frac{N\,s^2}{m^2}$
Trans Y DOF	873 kg	769 kg	-1426 $\frac{N\,s^2}{m^2}$	-1400 $\frac{N\,s^2}{m^2}$
Trans Z DOF	1021 kg	1031 kg	-3060 $\frac{N\,s^2}{m^2}$	-3039 $\frac{N\,s^2}{m^2}$
Angular X DOF	103.5 $kg\,m^2$	-1.348 $kg\,m^2$	-728.4 $N\,s^2$	-761.5 $N\,s^2$
Angular Y DOF	137.1 $kg\,m^2$	42.5 $kg\,m^2$	-769.1 $N\,s^2$	-681.4 $N\,s^2$
Angular Z DOF	106.4 $kg\,m^2$	41 $kg\,m^2$	-376.2 $N\,s^2$	-393.3 $N\,s^2$

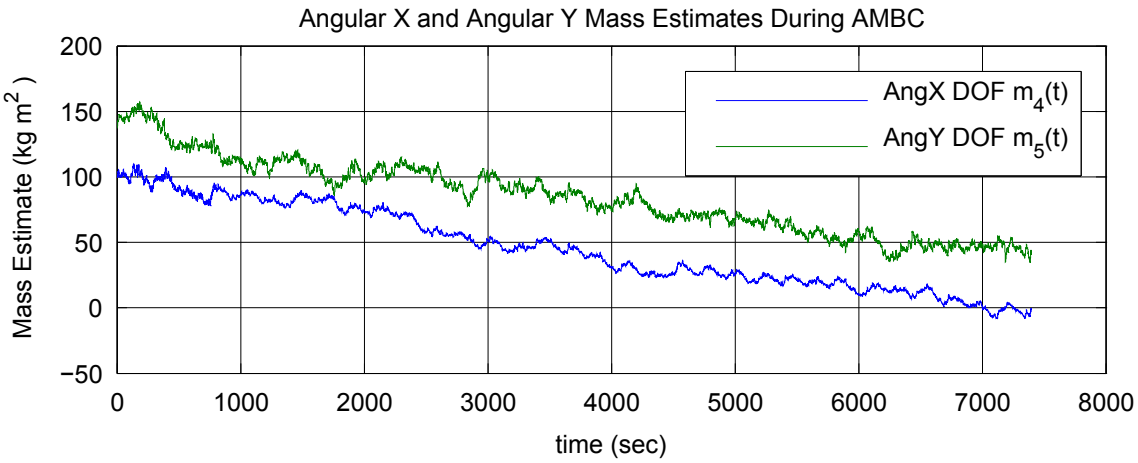

Figure 5.1: The time evolution of Angular X DOF and Angular Y DOF mass estimates from AMBC during 6-DOF dynamic maneuvers. These mass estimates adapt to physically unrealistic negative values and show no signs of asymptotic behavior.

5.3.3 Unmodeled Thruster Dynamics within the UV Control Process

The JHU ROV control system uses the common assumption of *steady-state* thruster operation when calculating the actuator commands (see Appendix A.1). In *steady-state* operation at zero advance velocity the axial thrust of a bladed-propeller marine thruster is linearly proportional to the applied shaft torque, and is also linearly proportional to the signed-square of the shaft angular-velocity [68]. The parameters of these steady-state thruster models cannot be determined analytically, but are easily estimated with simple steady-state experiments. Research has shown that the *transient* performance of marine thrusters can be accurately approximated by a finite-dimensional second-order plant model of propeller-fluid interaction. The plant parameters of these dynamic thruster models cannot be determined analytically, and are difficult to estimate experimentally because such identification requires highly instrumented measurements of the thruster thrust, prop angular velocity, and fluid flow velocity in unsteady operation [8, 22, 33, 70].

Because unsteady thruster model parameters are difficult to obtain experimentally, in the design of marine vehicle control systems it is common practice to employ easily-obtained steady-state thruster models. This approach works extremely well for steady-state or slowly time-varying vehicle motion, but results in the presence of unmodeled thruster dynamics during highly dynamic vehicle maneuvering. In 1984, Rohrs et al. famously showed that stable adaptive controllers for linear time-invariant plants can be destabilized

by the presence of unmodeled plant dynamics [58]. To the best of our knowledge, this is the first observation of unmodeled thruster dynamics resulting in the destabilization of AMBC.

5.3.4 Comparative Experimental Evaluation of AMBC During Pitch-Only Motion in the Presence of Unmodeled Thruster Dynamics

This Section reports two experiments using AMBC to control the JHU ROV. In the first experiment parameter adaptation is unstable; in the second experiment parameter adaptation is stable. In both experiments the vehicle follows a pitch-only reference trajectory; the mass, drag, and gravitational terms were initialized to parameters previously identified to model vehicle performance (tabulated in Tables 5.4 and 5.5); and the gains used were $k_p = 300$, $k_d = 100$ $\gamma_{m_i} = 1000$, $\gamma_{d_i} = 5000$, $\gamma_g = \gamma_{b_1} = \gamma_{b_2} = 0.5$ and $\gamma_{b_3} = 10.0$. In the first experiment, the pitch-only reference trajectory oscillates about zero pitch. In the second experiment, pitch-only reference trajectory oscillates about a mean pitch of 5° with an amplitude of 3°. The first experiment requires thrust reversals to follow the specified reference trajectory, and the second experiment does not require thrust reversals.

Figure 5.2 plots the pitch, angular velocity, thrust commands, and mass estimate derivative for the experiment with thrust reversals. In the thrust subplots the four lines are plotted, the commanded and estimated thrusts are shown for the two thrusters actuating vehicle

pitch. Note that the thrust is estimated using a thruster's measured angular velocity as detailed in Appendix A.1. Note that for both thrusters as the commanded thrust crosses zero, the measured output remains zero until the commanded thrust reaches 5 Newtons. The buoyancy torque's influence causes the pitch and y angular velocity to significantly deviate from their respective reference trajectories. From the perspective of the AMBC algorithm, these deviations from the position and velocity reference trajectories are indistinguishable from the deviations which would occur if the estimated pitch inertia were too large, thus the parameter estimate update for this term, $\dot{\hat{m}}_5$, has a large negative spike after each thrust reversal. Over a multi-hour experiment this systematic error causes pitch and roll mass estimates to adapt to physically unrealistic negative values.

Figure 5.3 plots the pitch, angular velocity, thrust commands, and mass estimate derivative for the experiment without thrust reversals. Without thrust reversals, the chain of events leading to a large negative spike in the pitch mass update law are not present. The balanced parameter adaptation seen in this third experiment leads to pitch mass convergence to a physically realistic value.

5.3.5 Experimental Evaluation of Two-Step Method

In this Section we report an experimental evaluation of the two-step algorithm reported in Section 5.2.6.

The first step is identifying the gravitational and buoyancy parameters for the UV using

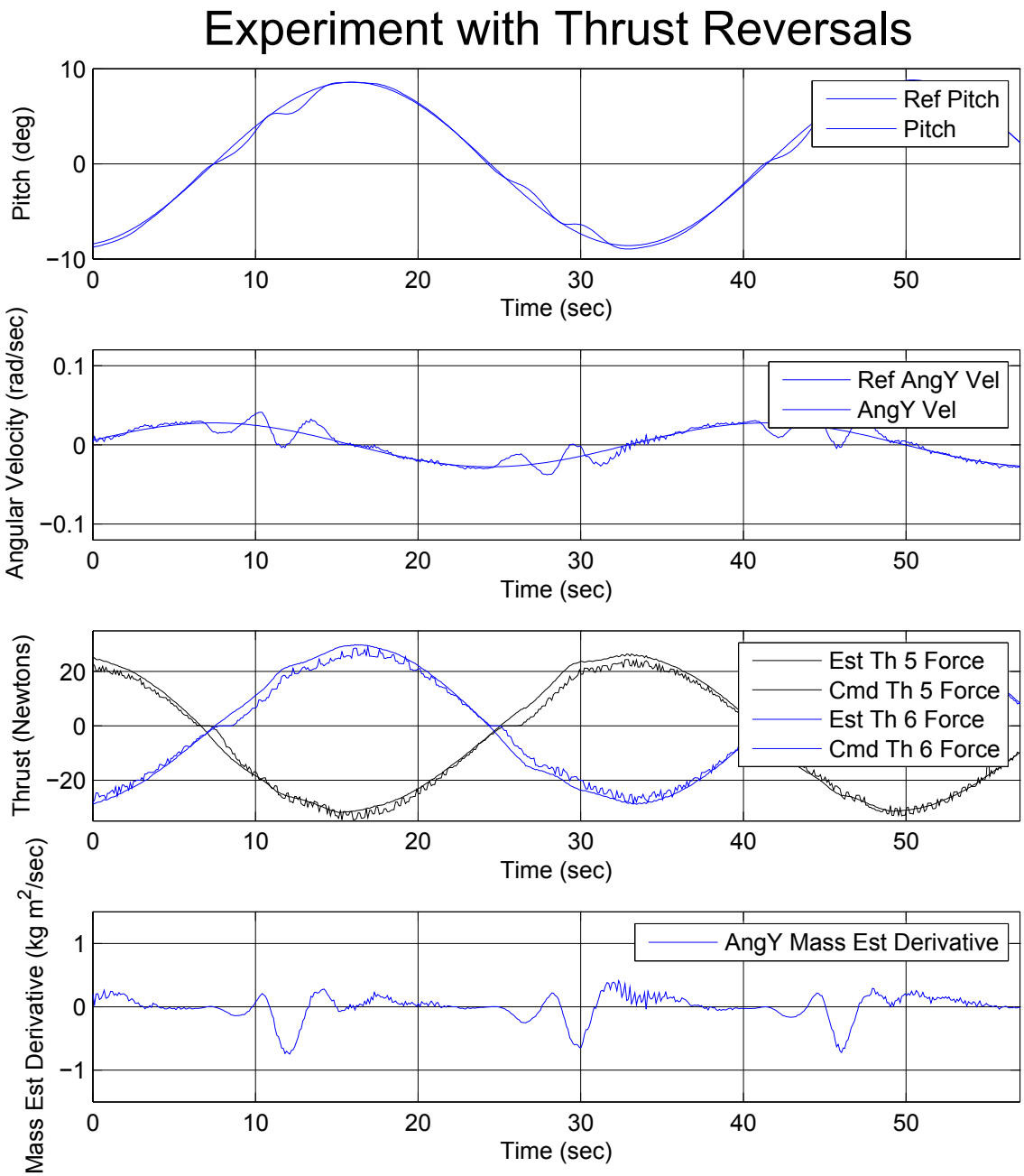

Figure 5.2: Fifty five seconds of data from a experiment where AMBC was used to follow a single DOF reference trajectory in pitch. Following the reference trajectory required thrust reversals. Thruster force was estimated using measured propeller angular velocity. In the commanded/estimated thruster subplot, a short period of thruster stiction is seen at each thrust reversal. The effects of thruster stiction are seen in both the pitch and angular velocity plots as deviations from each state's respective reference trajectory. In the pitch mass estimate derivative, the parameter update law is seen to have a large negative spike after each thrust reversal.

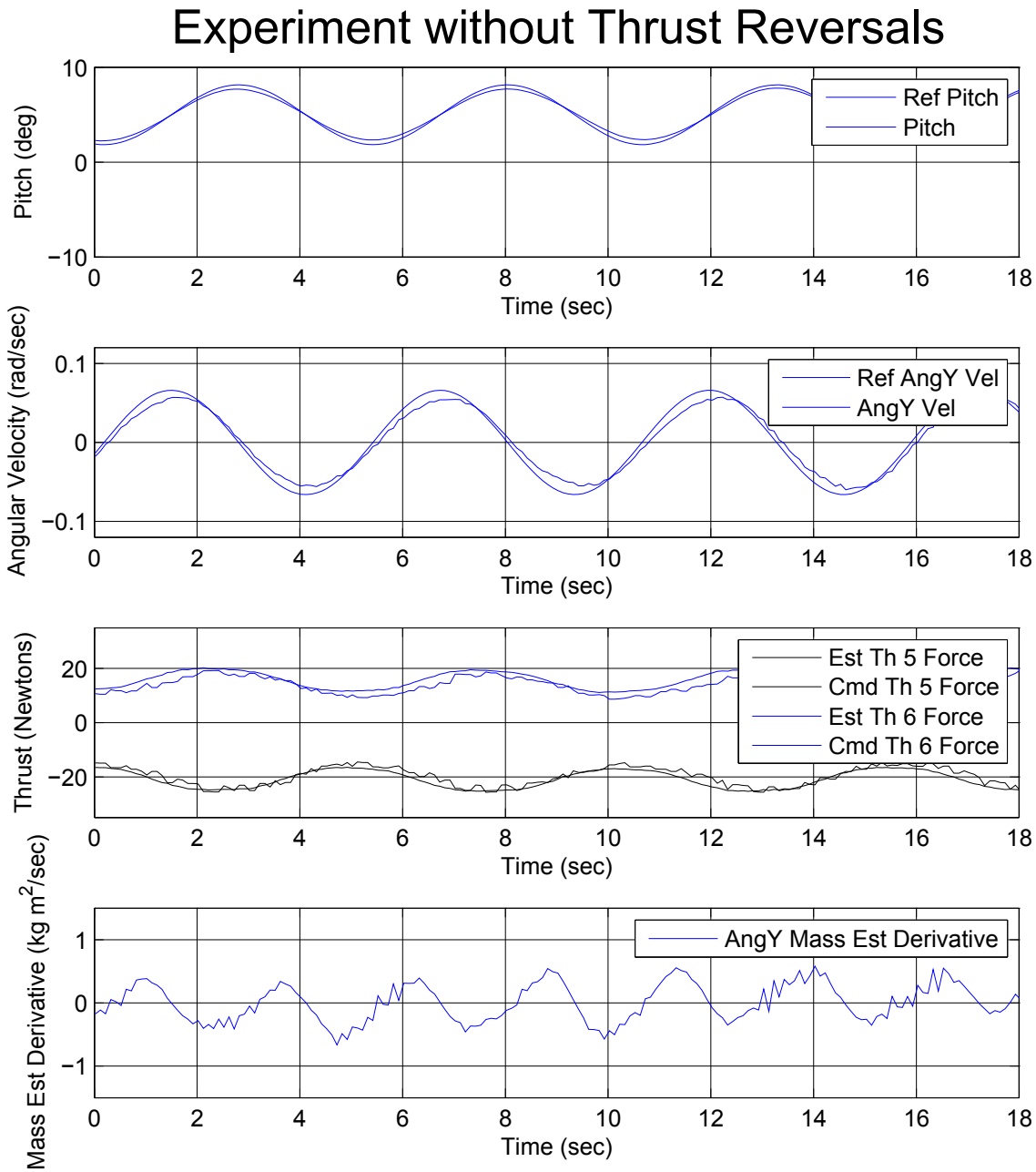

Figure 5.3: Eighteen seconds of data from a experiment where AMBC was used to follow a single DOF reference trajectory in pitch. Following the reference trajectory did not require thrust reversals. Thruster force was estimated using measured propeller angular velocity. In the commanded/estimated thruster subplot thruster stiction is not observed. The chain of events leading to a large negative spike in the pitch mass update law are not present in this experiment.

the adaptive tracking controller for plant model (5.37). The reference trajectory was constant in translational position and heading, with slow changes in pitch and roll to provide quasi-static motion. For this experiment we used a sinusoidal pitch reference trajectory with a magnitude of 0.2 rad and frequency of 34 Hz and a sinusoidal roll reference trajectory with a magnitude of 0.15 rad and frequency of 42 Hz. The gains used were $k_p = 300$, $k_d = 100$, $\gamma_g = \gamma_{b_1} = \gamma_{b_2} = 0.5$, and $\gamma_{b_3} = 10.0$. Over a 90 minute experiment the gravitational and buoyancy parameters were stable and converged to the physically realistic values shown in Table 5.4.

Table 5.4: Gravitational Parameters Identified During Quasi-Static Motion

	g	b_1	b_2	b_3
	N	$N\,m$	$N\,m$	$N\,m$
Final	3.59	1.696	3.09	300

The second step uses the identified parameters from Table 5.4 in a AMBC which estimates the mass and drag parameters, as described in Section 5.2.6. In the second step of the two-step AMBC algorithm the reference trajectory specified was RefTraj1 from Table 5.1; the mass and drag parameters were initialized to zero; and the gains used were $k_p = 300$, $k_d = 1000$, $\gamma_{m_i} = 1000$, and $\gamma_{d_i} = 5000$. Over a four and a half hour experiment all 12 mass and drag parameters were observed to be stable and converge to physically realistic values. Table 5.5 records the initial and final states for each dynamic parameter estimate.

Table 5.5: Parameters Identified with two-step AMBC during Dynamic Motion Trajectory-Tracking

	$m_i(t_o)$	$m_i(t_f)$	$d_i(t_o)$	$d_i(t_f)$
Trans X DOF	0.0 *kg*	628 *kg*	0.0 $\frac{N\,s^2}{m^2}$	-1259 $\frac{N\,s^2}{m^2}$
Trans Y DOF	0.0 *kg*	791 *kg*	0.0 $\frac{N\,s^2}{m^2}$	-1429 $\frac{N\,s^2}{m^2}$
Trans Z DOF	0.0 *kg*	1043 *kg*	0.0 $\frac{N\,s^2}{m^2}$	-3083 $\frac{N\,s^2}{m^2}$
Angular X DOF	0.0 *kg* m^2	95.7 *kg* m^2	0.0 $N\,s^2$	-727.1 $N\,s^2$
Angular Y DOF	0.0 *kg* m^2	145.3 *kg* m^2	0.0 $N\,s^2$	-783.4 $N\,s^2$
Angular Z DOF	0.0 *kg* m^2	110.2 *kg* m^2	0.0 $N\,s^2$	-465.6 $N\,s^2$

5.3.5.1 Two-Step AMBC Trajectory Tracking Performance

Figure 5.4 compares the performance of the second step of the two-step AMBC to a PDC with comparable gains. These two plots contain the exponential position and velocity MNE for the PDC and two-step AMBC experimental run. Both controllers were following the reference trajectory RefTraj1 from Table 5.1 as well as using $k_p = 300$ and $k_d = 100$. The PDC MNEs values were calculated using 10 minutes of data. The two-step AMBC MNEs values were calculated for consecutive 15 minutes windows. Note that after parameter convergence the two-step AMBC provides 30% better position tracking and 8% worse velocity tracking than PDC with similar gains.

Table 5.6 reports the trajectory tracking MAE values of individual DOF for both the PDC and two-step AMBC experiments. The PDC MAEs values were calculated using 10 minutes of data. The two-step AMBC MAEs values were calculated for consecutive 15 minutes windows. For each of the position DOF, two-step AMBC MAE values were smaller than PDC values. With the exception of heading, two-step AMBC position trajectory tracking improved in each DOF as the parameter adaptation process progressed. Of

the velocity DOF, two-step AMBC only outperformed PDC in the x and y angular velocity DOF. With the exception of y angular velocity, two-step AMBC velocity trajectory-tracking performance degraded slightly as the parameter adaptation process occurred. For the DOF in which trajectory-tracking is not improving, this could be an effect of unmodeled thruster dynamics or other dynamics which are not included in the uncoupled lumped-parameter model of UV dynamics used in our AMBC algorithm. However, taken as a whole, this experimental evaluation indicates that AMBC can provide increased trajectory-tracking performance in the presence of unmodeled thruster dynamics.

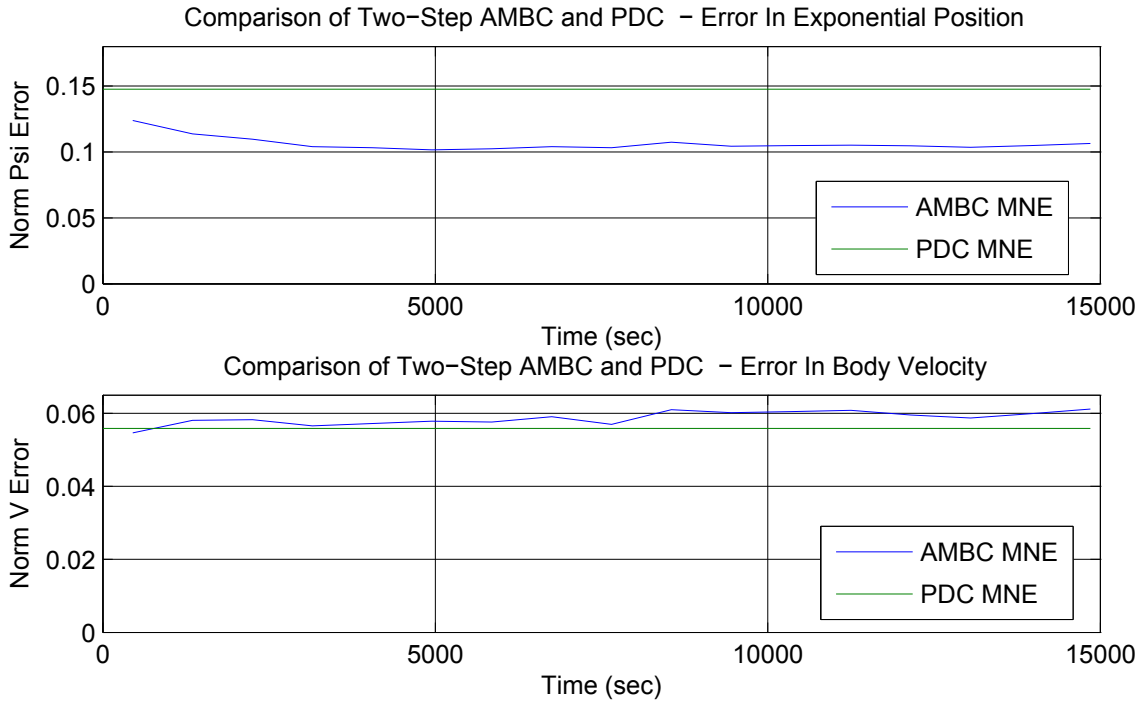

Figure 5.4: Exponential position and velocity MNE values for the experimental evaluations of two controllers, PDC and two-step AMBC. Both controllers were following the same reference trajectory (RefTraj1 from Table 5.1) as well as using the gains $k_p = 300$ and $k_d = 100$. The PDC MNE values were calculated using 10 minutes of data, this single value is plotted in green across the entire figure. The two-step AMBC MNE values were calculated for consecutive 15 minute windows and plotted in blue.

Table 5.6: mean absolute error (MAE) values for both the PDC and two-step AMBC experiments. The MAE for each DOF is shown. 10 minutes of experimental data were used to calculate the PDC MAEs. AMBC MAEs were calculated for consecutive 15 minute windows spread over the 3 hour experiment.

Parameter Set -	Time Block *min*	PosX *m*	PosY *m*	PosZ *m*	Hea *rad*	Pit *rad*	Rol *rad*	BodVelX *m/sec*	BodVelY *m/sec*	BodVelZ *m/sec*	AngVelX *rad/sec*	AngVelY *rad/sec*	AngVelZ *rad/sec*
PDC Exp	-	0.076	0.061	0.058	0.028	0.047	0.04	0.0172	0.021	0.0156	0.021	0.028	0.0078
AMBC Exp	0-14	0.059	0.051	0.064	0.021	0.023	0.0181	0.022	0.023	0.0194	0.0136	0.017	0.0134
AMBC Exp	15-29	0.051	0.045	0.063	0.022	0.0196	0.0184	0.024	0.023	0.02	0.0137	0.0157	0.0162
AMBC Exp	30-44	0.047	0.046	0.057	0.021	0.0196	0.0171	0.023	0.025	0.02	0.013	0.0169	0.0153
AMBC Exp	45-59	0.046	0.045	0.054	0.0192	0.018	0.0165	0.023	0.025	0.0196	0.0136	0.0157	0.0149
AMBC Exp	60-74	0.046	0.043	0.052	0.021	0.0174	0.0162	0.024	0.025	0.019	0.0136	0.0162	0.0161
AMBC Exp	75-89	0.047	0.047	0.046	0.0198	0.0174	0.0156	0.023	0.027	0.0179	0.0138	0.0168	0.0152
AMBC Exp	90-104	0.047	0.045	0.05	0.021	0.0168	0.0155	0.024	0.024	0.0192	0.0143	0.0164	0.0155
AMBC Exp	105-119	0.046	0.046	0.052	0.022	0.0174	0.0155	0.024	0.026	0.0198	0.014	0.0165	0.0162
AMBC Exp	120-134	0.048	0.044	0.05	0.022	0.0162	0.0153	0.021	0.025	0.021	0.0133	0.0159	0.0151
AMBC Exp	135-149	0.049	0.048	0.054	0.021	0.0182	0.015	0.023	0.027	0.023	0.0145	0.0169	0.016
AMBC Exp	150-164	0.049	0.045	0.05	0.022	0.0177	0.0145	0.025	0.026	0.021	0.0145	0.0172	0.0165
AMBC Exp	165-179	0.05	0.046	0.049	0.021	0.0166	0.0155	0.024	0.026	0.021	0.0143	0.0161	0.0167
AMBC Exp	180-194	0.049	0.046	0.052	0.021	0.0168	0.0151	0.024	0.026	0.022	0.0145	0.0167	0.0153
AMBC Exp	195-209	0.048	0.047	0.05	0.021	0.017	0.0149	0.024	0.024	0.021	0.0141	0.0165	0.016
AMBC Exp	210-224	0.05	0.045	0.049	0.022	0.0169	0.0149	0.023	0.026	0.02	0.0139	0.0163	0.0161
AMBC Exp	225-239	0.05	0.046	0.049	0.021	0.0174	0.0147	0.024	0.027	0.021	0.0142	0.0166	0.0148
AMBC Exp	240-255	0.047	0.046	0.054	0.022	0.0172	0.0147	0.025	0.026	0.023	0.0145	0.0164	0.0169

5.3.5.2 Two-Step AMBC Parameter Cross-Validation

In addition to providing trajectory-tracking, AMBC has also been proposed to identify UV models. Two questions arise:

- "How good is the identified model at reproducing vehicle performance?"

- "Considering the time series of parameter estimates, do the resulting plant models get better at matching JHU ROV performance as the parameter adaptation process progresses?"

To address these questions we preformed a cross-validation experiment (Appendix A.2) by driving the JHU ROV to follow RefTraj2 from Table 5.1. Figures 5.5 to 5.7 show the ability of the identified model to match vehicle performance in forward simulation increases during parameter adaptation. Each Figure shows experimentally measured states verses the states from numerical simulations; each numerical simulation uses a model identified by the two-step AMBC after a set amount of time. Each JHU ROV simulation used the thrust inputs recorded and initial JHU ROV states to create a forward simulation. All eight open-loop-stable states are plotted. In both the plots and listed MAE values, the capacity of the identified parameters to model vehicle performance in every DOF increases as time progresses. The fact that the parameter estimates are progressively improving suggests that the parameter adaptation process is working despite the presence of unmodeled thruster dynamics.

As was seen with adaptive identification (AID) and least squares identification (LS) in Sections 4.5 and 4.6, the models identified using two-step AMBC were not able to reproduce the highest frequency fluctuation's observed experimentally (such as those seen in the x angular velocity subplots of Figure 5.6). However, the states shown from simulating a model using the "5000 sec" parameter set (the final parameter set included in this analysis) indicate that AMBC can produce parameter estimates which result in accurate plant models.

5.3.6 The Effects of Unmodeled Thruster Dynamics on AMBC

The experiment reported in Section 5.3.2 shows, curiously, a clear differentiation in parameter adaptation performance; unstable parameter adaption occurred only in the parameter estimates associated with pitch and roll dynamics. To further explore this effect, in Section 5.3.4 we investigated parameter adaptation during pitch-only reference trajectory excitation. These data show thrust reversals cause parameter instability. Further, the thruster angular velocity data indicate a difference between the actual and commanded torques applied to the vehicle. Based on our knowledge of the JHU ROV control system and thruster design, the data from these pitch-only experiments suggest that unmodeled thruster dynamics are present during thrust reversals. Without further experimental analysis we can not specify if the specific mechanism causing unstable parameter adaptation

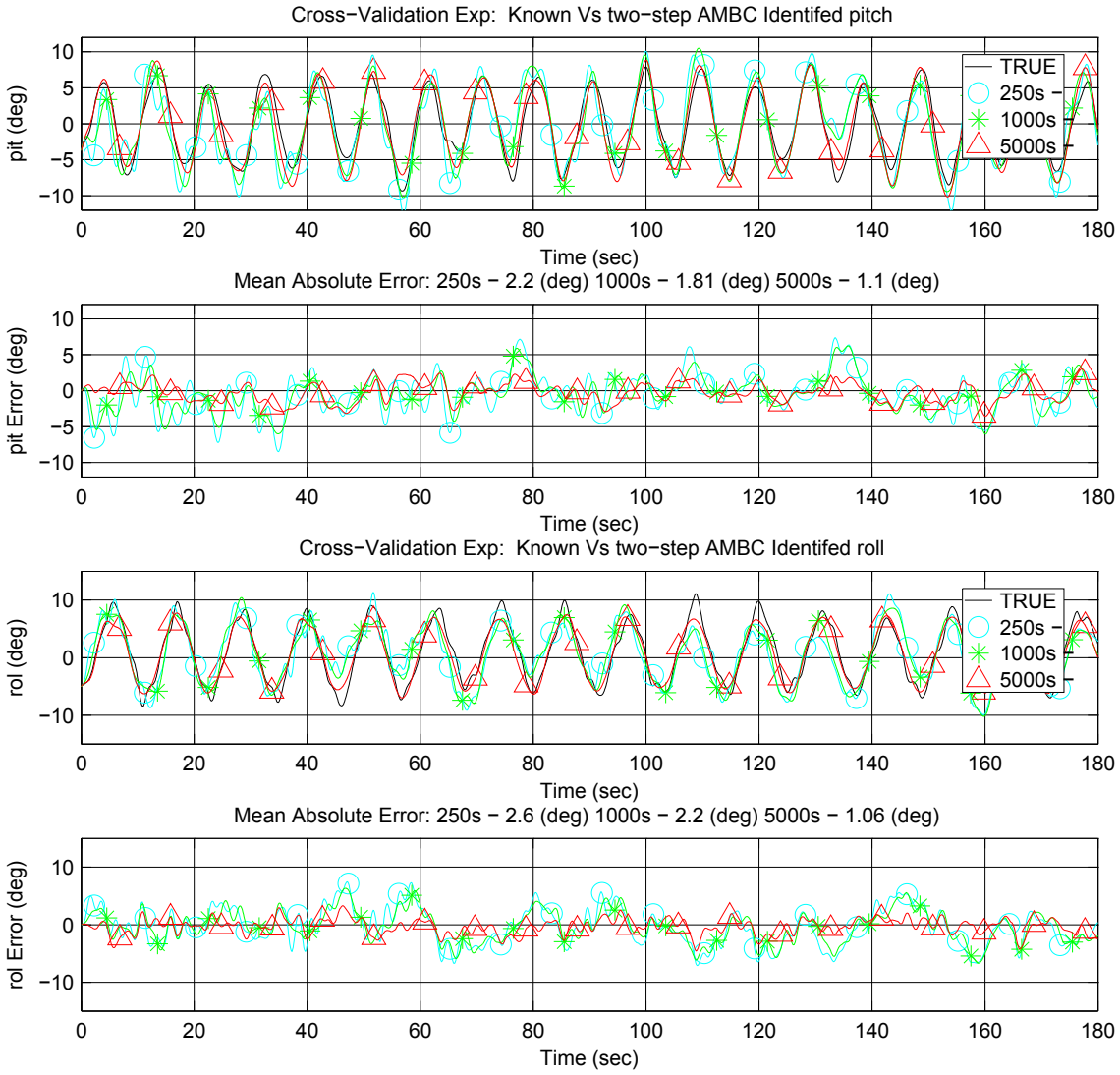

Figure 5.5: Representative data of experimental and simulated JHU ROV states during 6-DOF dynamic operation. In the roll and pitch plots the measured state is plotted together with the position estimates from three JHU ROV simulations. The three parameter sets were taken from the time history of parameter adaptation recorded during the two-step AMBC experiment. The '250s' forward simulation (plotted in blue and marked with circles) models JHU ROV performance using parameters identified after 250 seconds of parameter adaptation. Similarly the '1000s' forward simulation (plotted in green and marked with stars) and '5000s' forward simulation (plotted in red and marked with triangles) use parameters identified after 1000 and 5000 seconds of parameter adaptation respectively. For each DOF, the error between the measured positions and their estimates is shown.

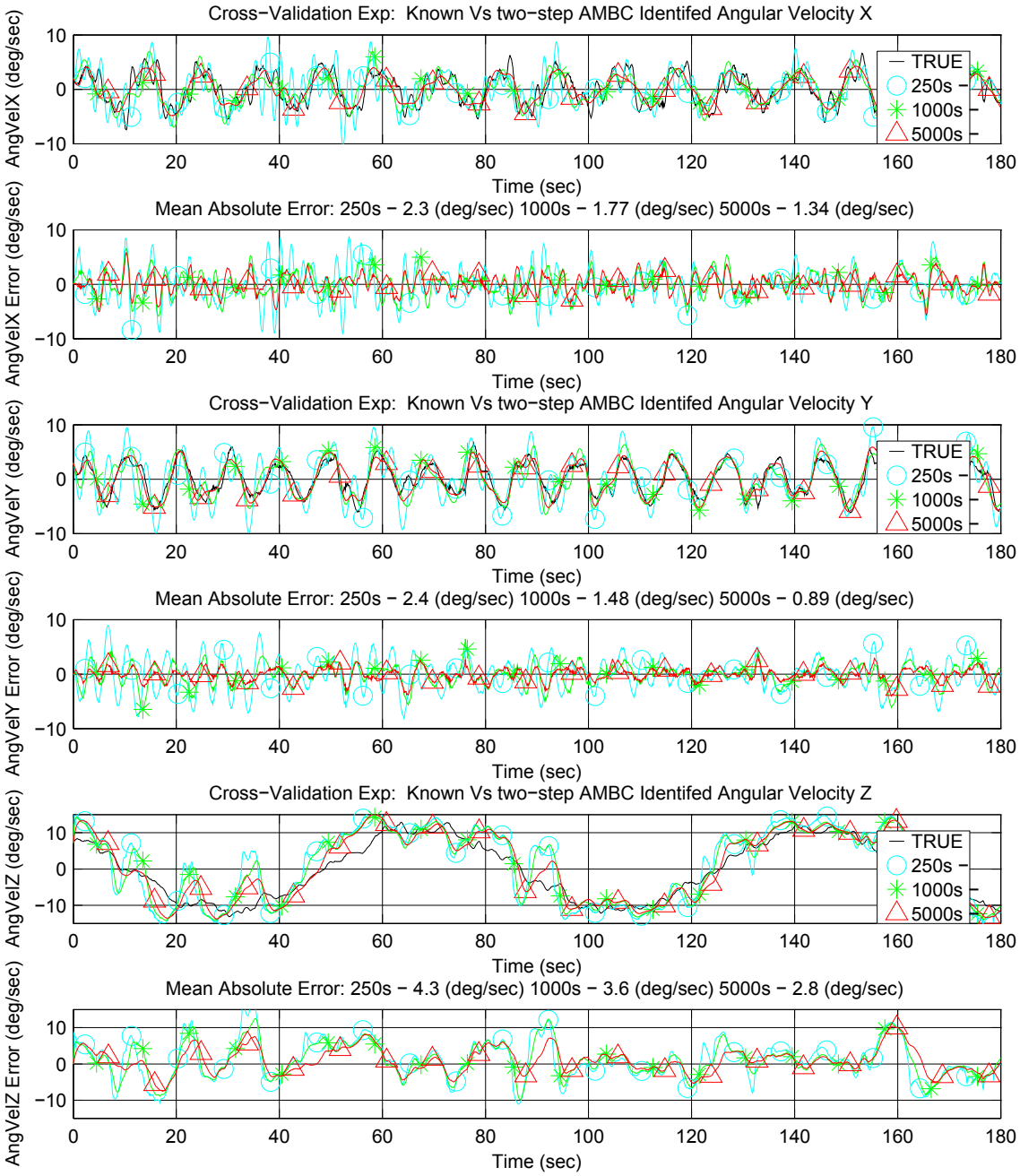

Figure 5.6: Representative data of experimental and simulated JHU ROV states during 6-DOF dynamic operation. In the three angular velocity plots, the measured state is plotted together with the velocity estimates from three JHU ROV simulations. The three parameter sets were taken from the time history of parameter adaptation recorded during the two-step AMBC experiment. See Figure 5.5 caption for further information on each parameter set. For each DOF, the error between the measured positions and their estimates is shown.

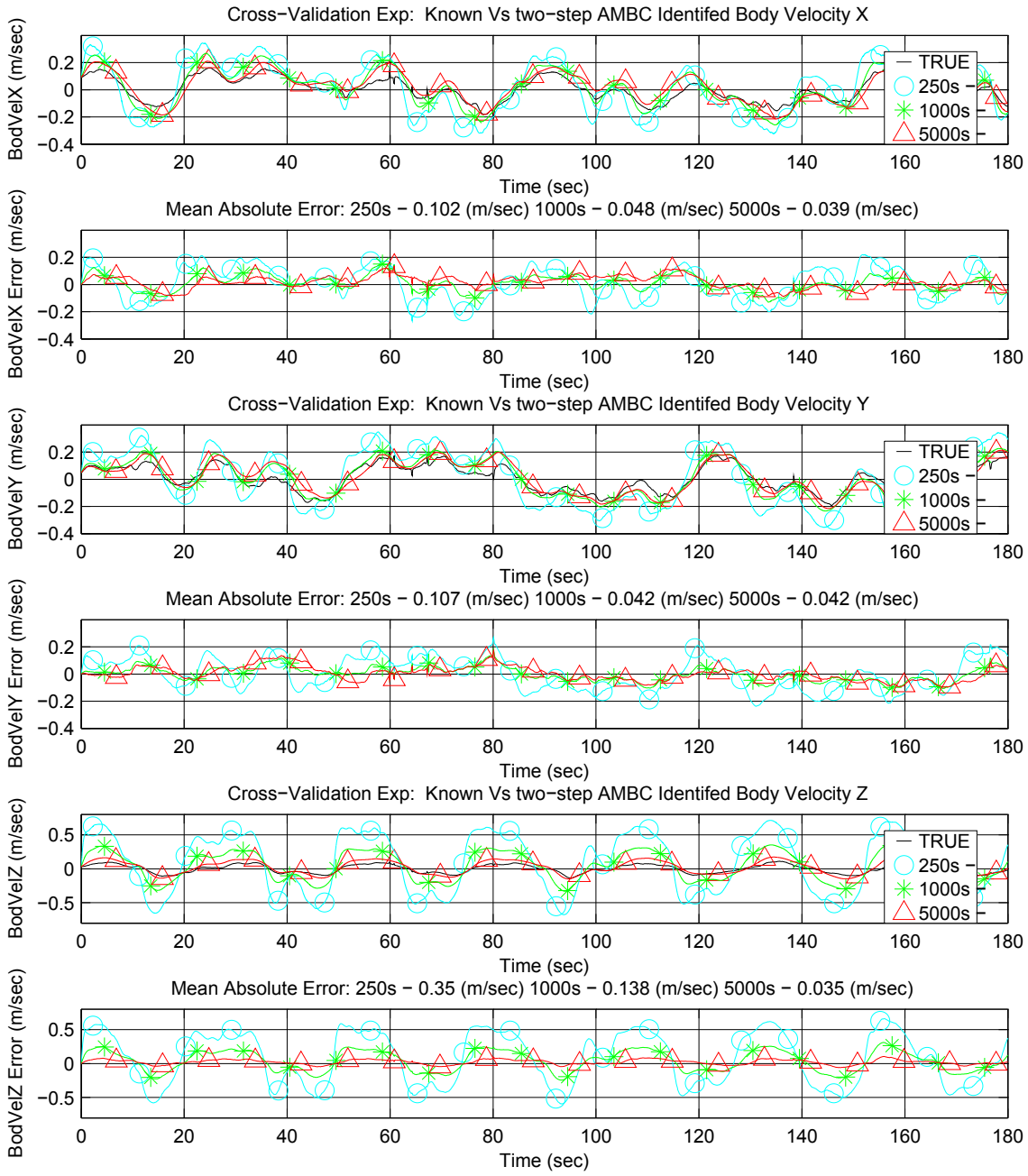

Figure 5.7: Representative data of experimental and simulated JHU ROV states during 6-DOF dynamic operation. In the three body velocity plots, the measured state is plotted together with the velocity estimates from three JHU ROV simulations. The three parameter sets were taken from the time history of parameter adaptation recorded during the two-step AMBC experiment. See Figure 5.5 caption for further information on each parameter set. For each DOF, the error between the measured positions and their estimates is shown.

is unmodeled thruster mechanical dynamics, fluid dynamics, mechanical friction during thrust reversals, or some combination of these mechanisms. Regardless of the underlying source of modeling error, these experiments suggest that unstable parameter adaptation will occur in parameters associated with a given DOF if the following three conditions are met:

- mass and gravitational parameter estimates are adapting,
- there exists of a single attractive stability point for that DOF, and
- unmodeled thruster dynamics are present.

The success of two-step parameter adaptation supports this hypothesis. Implementing the parameter estimation process in two steps removed the need for simultaneous adaptation of the mass and buoyancy terms. By separating parameter adaptation in this way, an ambiguity in the adaptation process was removed. Note the three factors listed imply that both the buoyancy and mass parameter estimates will be affected in the same way by unmodeled thruster dynamics during thrust reversals. From the perspective of the AMBC algorithm, the deviations from the position and velocity reference trajectories caused by unmodeled thruster dynamics are indistinguishable from the deviations which would occur if either of these parameter estimates (the buoyancy torque estimate or the inertia estimate) were too large. The effects of the inertia tensor and buoyancy torque parameters on vehicle position and velocity are also coupled. For instance there will be similarities between the dynamics of a UV with a large mass and large buoyancy torque and a UV with a small mass and small buoyancy torque for a proper scaling of these properties. During each period of

unmodeled thruster dynamics, the simultaneous unstable adaptation of the inertia and buoyancy estimates was difficult for the AMBC algorithm to overcome because the estimate of vehicle dynamics was only slightly degraded by the physically unrealistic changes in these parameter estimates. Setting the buoyancy torque estimate to a fixed value during dynamic maneuvers removes the possibility of simultaneous adaptation to physically unrealistic values.

5.4 Conclusion

This Chapter presents both theoretical and experimental results concerning UV AMBC. Section 5.2 reports MBC and AMBC algorithms, along with a local proofs of stability. Section 5.3 reports an experimental investigation of a previously unreported UV AMBC failure mode where unmodeled thruster dynamics during thrust reversals cause unstable parameter adaptation. The Section also reports a novel two-step AMBC algorithm which is shown experimentally to provide stable trajectory tracking and parameter adaptation in the presence of the unmodeled thruster dynamics of our system. Finally, it reports a comparative experimental analysis of the two-step AMBC algorithm with PDC. This experimental evaluation shows that two-step AMBC provides 30% better position tracking performance and 8% worse velocity tracking performance over PDC.

Chapter 6

Conclusion

6.1 Thesis Summary

This Thesis reports algorithms for state estimation, adaptive parameter identification, and model-based control principally for underwater vehicle (UV) applications. An analytical proof of stability is included for every reported algorithm. Chapter 3 reports an angular velocity observer for rotating rigid-bodies, an adaptive identification (AID) algorithm for rotating rigid-bodies, and an AID algorithm for open kinematic chains (OKCs). Numerical simulations of the AID algorithm for rotating rigid-bodies corroborate the analytical stability analysis and investigate parameter convergence with varying initial conditions, adaptation gains, and input torques. Chapter 3 also reports a comparative analysis of three nonlinear angular velocity observer for rotating rigid-bodies; in numeric simulations the novel angular velocity observer (Theorem 3.2.1) is shown to provide performance similar

to that of the two previously reported observers.

Chapter 4 reports two AID algorithms for the dynamic estimation of UV plant parameters. Chapter 4 also reports two comparative experimental evaluations of adaptive identification and least squares identification. Both the adaptively identified plant models (AIDPMs) and the least squares identified plant models (LSPMs) are shown to match closely the experimentally observed UV input-output behavior. Adaptive identification algorithms do not require simultaneous reference trajectory-tracking control, nor do they require instrumentation of linear acceleration or angular acceleration. Together, these facts make adaptive identification applicable to a wider class of UVs than previously reported methods. Chapter 5 reports an UV model-based control (MBC) algorithm and UV adaptive model-based control (AMBC) algorithm. Chapter 5 also reports an experimental evaluation of the destabilizing effects of unmodeled thruster dynamics on AMBC and a two-step AMBC algorithm which is shown experimentally to be robust in the presence of unmodeled thruster dynamics. A comparative experimental analysis of the two-step AMBC and proportional derivative control (PDC) is reported; it showed that AMBC provides 30% better position tracking performance and marginally worse (8%) velocity tracking performance over PDC.

6.2 Future Work

In addition to the straightforward applications of UV AID and UV AMBC discussed in Chapter 1, these algorithms could also enable complex, multifaceted UV missions by using AID for fault detection and AMBC for fault compensation.

As shown in Chapter 4, UV AID dynamically estimates parameters assumed to be constant. When applying UV AID for fault detection, parameter adaptation is monitored for changes indicative of UV component failures. Different parameters can be monitored for different types of failures. For example, drag parameters could be used to detect entanglement, mass parameters could be used to detect flooded housings or detached components, and a general force/torque vector could be used to detect unanticipated UV collisions.

As shown in Chapter 5, AMBC uses plant parameter estimates for model-based trajectory-tracking and these plant parameter estimates are iteratively improved in a process similar to AID. Since AMBC algorithms evolve parameter estimates in a process similar to AID, they are naturally robust to UV component failures. Designing a suite of AMBC algorithms which compensate for particular component failures and using a collection of AID algorithms to switch between these AMBC algorithms could allow fast, effective fault compensation.

Current UV control systems rely on engineers to detect remotely and compensate for vehicle component failures. As UV mission complexity has increased, this component failure detection and compensation method has become a barrier limiting future deployments. Using AID and AMBC to automate failure detection and failure compensation has the po-

tential to *i*) lower the amount of time lost due to mission aborts, *ii*) limit the possibility of losing a vehicle, and *iii*) enable new missions which are currently impossible due to vehicle safety concerns. Missions benefiting could include:

- *Long Duration Unsupervised Deployments:* Some UVs are capable of deployments lasting from days to weeks [10, 28]. The capacity to detect and compensate for UV component failures increases the likelihood of successful unsupervised deployments.

- *Semi-Autonomous UV Operations:* Semi-autonomous missions use human direction and data interpretation to accomplish actions too complex to automate. Automated failure detection will allow engineers to understand the vehicle's current state and predict its future capabilities.

- *Under Ice Operations:* The Polar Remotely Operated Vehicle (PROV) is currently being developed for under ice operation [11, 26], where surfacing in the event of a failure is not an option. PROV's thruster redundancy will allow continued operation with multiple thruster failures. However, utilizing this redundancy requires detecting the failures.

In short, this Thesis reports adaptive algorithms which enable better utilization of current UVs. These results are also the starting point for algorithms which enable complex, multifaceted missions of both the current generation of UVs and those to come.

Appendix A

UV Experimental Facility and Algorithm Evaluation Methods

A.1 JHU Hydrodynamic Test Facility

The Johns Hopkins Hydrodynamic Test Facility [34] contains an indoor fresh water tank measuring $7.75\ \mathrm{m}$ in diameter and $4.25\ \mathrm{m}$ deep, as shown in Figure A.1. The facility is equipped with the JHU ROV, a fully instrumented underwater vehicle (UV) designed for navigation and control research. The JHU ROV displaces $150\ \mathrm{kg}$ and is actuated by six $1.5\ \mathrm{kWh}$ DC brushless electric direct drive thrusters providing full control authority for 6-degree-of-freedom (DOF) maneuvers. Each thruster is controlled with a current-mode amplifier. The JHU ROV control system generates the command current for each

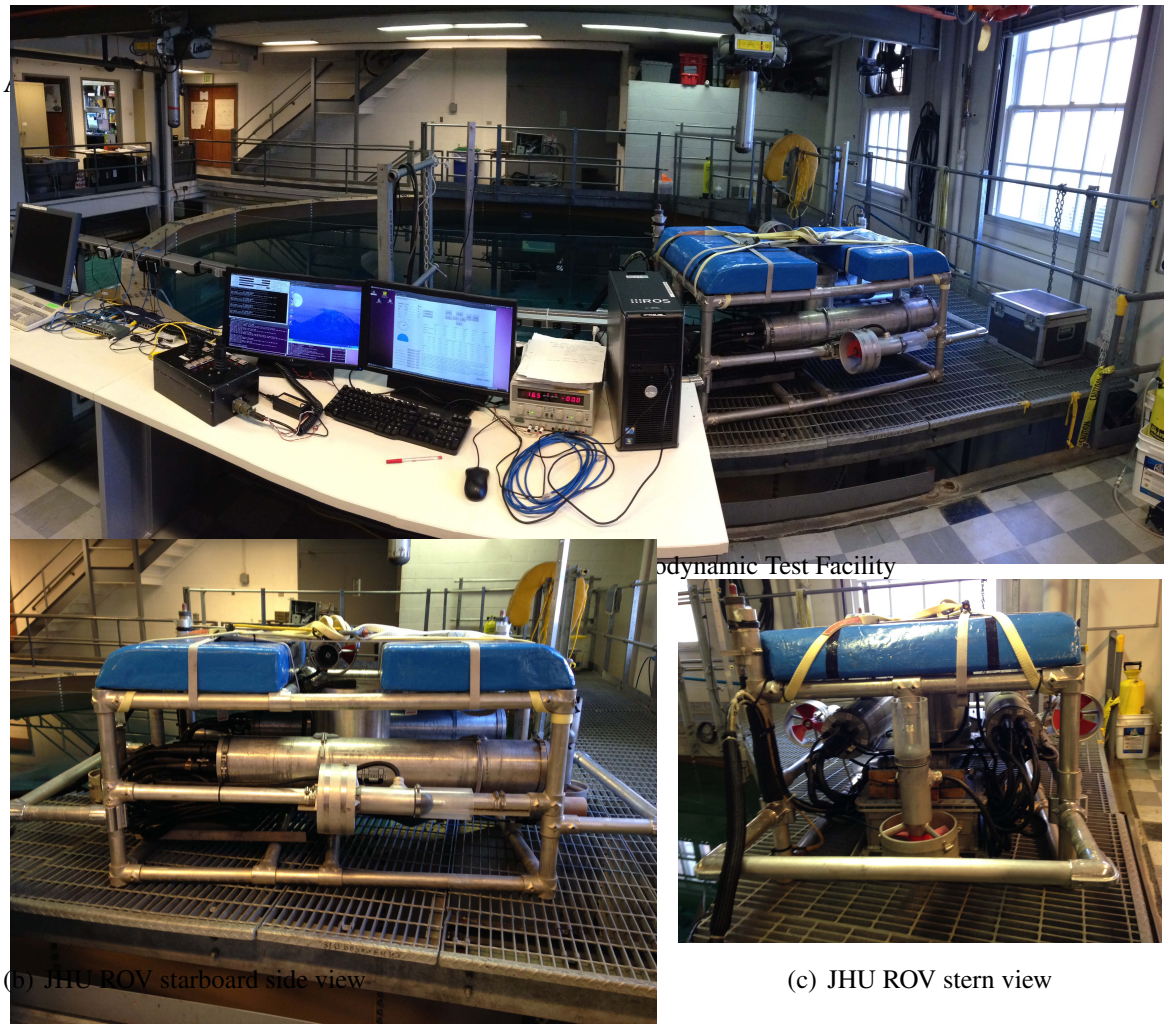

odynamic Test Facility

(b) JHU ROV starboard side view

(c) JHU ROV stern view

Figure A.1: Johns Hopkins University Hydrodynamic Test Facility and Johns Hopkins University Remotely Controlled Vehicle (JHU ROV).

thruster using data from *a-priori steady-state* thruster calibration experiments; no feedback is used in generating the commanded current. The angular velocity of each thruster is instrumented. This measured thruster angular velocity (ω_{th}) can be used to estimate the thruster force (f_{th}) using the empirically validated steady state relation $f_{th} = k_{th}\omega_{th}|\omega_{th}|$, where k_{th} is an empirically identified constant [68]. The vehicle's control system is capable of actively controlling 6-DOF vehicle motion. During an experiment, each of the 6 JHU ROV DOF were independently actuated using either closed-loop control or open-loop sinusoidal commanded torques. For the DOFs using closed-loop control, a sinusoidal reference

trajectory was specified to the JHU ROV control system.

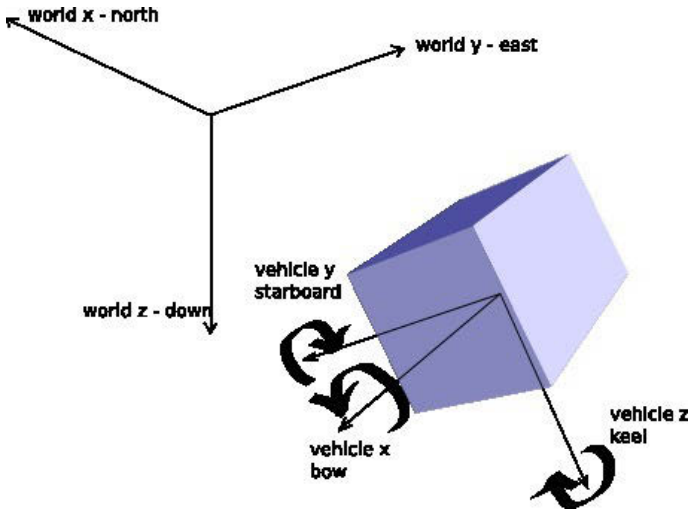

Figure A.2: The world-frame's orthonormal x, y, and z basis vectors point from the frame's origin towards in the directions north, east, and down respectively. The body-frame's orthonormal x, y, and z basis vectors point from the vehicles origin to the vehicle's bow side, starboard side and keel location respectively. Note the arrows showing positive rotation about each body axis.

The coordinate frames employed herein are depicted in Figure A.2. The world-frame's orthonormal x, y, and z basis vectors point from the frame's origin towards the direction north, east, and down respectively. Employing standard navel architecture conventions, the body-frame's orthonormal x, y, and z basis vectors point, respectively, from the vehicle's origin to the vehicle's bow, starboard side and keel. The Euler angles heading, pitch, and roll express the relationship between the world-frame and body-frame as follows: rotating the world-frame about its +z-axis through an angle heading, then rotating the resulting frame about its +y-axis through an angle pitch, then rotating the resulting-frame around its +x-axis through an angle roll provides the body-frame.

Table A.1: JHU ROV state measurement sources, resolutions, and accuracies

State	Source	Update Rate	Measurement Precision/Std Dev (Standard Deviation)
XY Translational Position	DVLNAV	10 Hz	Resolution >0.5% of Translational Distance Traveled
Z Translational Position	Digiquartz	7 Hz	Resolution >0.75% as calculated
Heading	PHINS III	10 Hz	0.13° Std Dev
Pitch, Roll	PHINS III	10 Hz	0.01° Std Dev
Translational Velocity	1200 kHz DVL	6 Hz	>0.003 m/s Std Dev
Angular Velocity	PHINS III	10 Hz	0.01°/s Std Dev

The sensors used in all experimental evaluations are recorded in Table A.1. The JHU ROV is instrumented by a PHINS III inertial navigation system (INS) (IXSEA SAS, Marly-le-Roi, France), 1200 kHz bottom-lock Doppler sonar (RD Instruments, San Diego, CA), and 8CDP010-1 Digiquartz Depth Sensor (Paroscientific Inc., Redmond, WA). The PHINS III INS includes a three-axis north-seeking fiber-optic gyrocompass, and inertial grade accelerometers whose data is used to estimate angular velocity, pitch, roll, and heading states at a rate of 10 Hz. For our PHINS configuration, the measurement error standard deviations are 0.01°/s for angular velocity estimates, 0.13° for heading estimates, and 0.01° for pitch and roll estimates [25]. The Doppler sonar measures the three dimensional linear velocity in the instrument's frame with a standard deviation of less than 0.003 m/s, an update rate of 6 Hz, and zero bias [1]. The Digiquartz has a maximum depth of 10 m and, as currently configured, has an update rate of 7 Hz, and provides pressure measurements at a resolution of 2 parts-per-million. Translational position estimates are provided by the DVLNAV

control software which integrates the the sensor signals reported above to provide dead reckoning XY translational position estimates better than 0.5% of distance traveled.

A.2 Parameter Identification Evaluation

To evaluate the performance of the identified plant models we employ an approach that we refer to as *cross-validation*. We use the plant model experimentally identified from one vehicle experimental trial to predict, in a numerical simulation, the performance of the plant in a different experimental trial whose trajectories differ from the identification trial. The class of plants given by (2.40) and (2.44) are open-loop-stable in their velocity signals as a consequence of hydrodynamic damping. In the presence of significant buoyancy torque due to center-of-buoyancy (COB) to center-of-gravity (COG) separation, both classes of plants are also open-loop-stable in roll and pitch. Because these open-loop signals are stable, we can employ these signals to compare a model plant's predicted performance to the actual plant's experimentally observed performance. The error between the predicted model performance and the experimentally observed performance is reported as the mean absolute error (MAE) between the simulated plant roll, pitch, and velocity and the actual experimental plant roll, pitch, and velocity.

Appendix B

SE(3) Velocity Jacobian

This Section derives several facts about the inverse SE(3) velocity Jacobian. This matrix valued function, $\hat{\mathcal{A}}^{-1} : \mathbb{R}^6 \to \mathbb{R}^{6\times 6}$, relates the body-frame velocity and time derivative of exponential coordinate pose by the equality

$$\dot{\psi} = \hat{\mathcal{A}}^{-1}(\psi)v. \tag{B.1}$$

In [13] the authors derive the following closed form equation for this matrix valued function

$$\hat{\mathcal{A}}^{-1}\left(\begin{bmatrix}\xi\\ q\end{bmatrix}\right) = I_{6\times 6} + \frac{1}{2}\operatorname{ad}\left(\begin{bmatrix}\xi\\ q\end{bmatrix}\right) + \mathcal{B}_1\left(\|q\|\right)\operatorname{ad}^2\left(\begin{bmatrix}\xi\\ q\end{bmatrix}\right) + \mathcal{B}_2\left(\|q\|\right)\operatorname{ad}^4\left(\begin{bmatrix}\xi\\ q\end{bmatrix}\right) \tag{B.2}$$

where

$$y^2\mathcal{B}_1\left(y\right) = 2\left(1-\alpha(y)\right) + \frac{1}{2}\left(\alpha(y)-\beta(y)\right) \tag{B.3}$$

$$y^4\mathcal{B}_2\left(y\right) = \left(1-\alpha(y)\right) + \frac{1}{2}\left(\alpha(y)-\beta(y)\right) \tag{B.4}$$

with $\alpha(y) = \frac{y}{2}\cot\left(\frac{y}{2}\right)$ and $\beta(y) = \left(\frac{y}{2}\right)^2 \frac{1}{\sin\left(\frac{y}{2}\right)^2}$. Using the fact that $\mathcal{J}(q)^3 = -\|q\|^2\mathcal{J}(q)$, (B.2) can be shown to be equivalent to

$$\hat{\mathcal{A}}^{-1}\left(\begin{bmatrix}\xi\\ q\end{bmatrix}\right) = \begin{bmatrix}\mathcal{A}^{-1}(q) & \frac{1}{2}\mathcal{J}(\xi) + \frac{1-\alpha(\|q\|)}{\|q\|^2}\mathcal{B}_4(\xi,q) + \mathcal{B}_2(\|q\|)\mathcal{B}_3(\xi,q)\\ 0_{3\times 3} & \mathcal{A}^{-1}(q)\end{bmatrix} \tag{B.5}$$

where $\mathcal{B}_4 : \mathbb{R}^3 \times \mathbb{R}^3 \to \mathbb{R}^{3\times 3}$ is defined by $\mathcal{B}_4(\xi, q) = \mathcal{J}(\xi)\mathcal{J}(q) + \mathcal{J}(q)\mathcal{J}(\xi)$ and $\mathcal{B}_3 : \mathbb{R}^3 \times \mathbb{R}^3 \to \mathbb{R}^{3\times 3}$ is defined by $\mathcal{B}_3(\xi, q) = \mathcal{J}(q)\mathcal{J}(\xi)\mathcal{J}(q)^2 + \mathcal{J}(q)^2\mathcal{J}(\xi)\mathcal{J}(q)$. To the best of the author's knowledge a closed form expression for the SE(3) velocity Jacobian, $\hat{\mathcal{A}}(\psi)$, has not been reported.

B.1 SE(3) Velocity Jacobian Bilinear se(3) Pose Multiplication Simplification

In this Section we prove

$$\psi^T\left(\hat{\mathcal{A}}^{-T}(\psi) + \hat{\mathcal{A}}^{-1}(\psi)\right)\psi = \psi^T\psi. \tag{B.6}$$

Consider inserting (B.5) into the left side of (B.6). Note that the definition of $\mathcal{A}^{-1}$ in (2.28) and $\mathcal{J}(q)\,q = \vec{0}$ imply the following facts:

- $\mathcal{A}^{-1}(q)q = q$,
- $\frac{1-\alpha(\|q\|)}{\|q\|^2}\mathcal{J}(\xi)\mathcal{J}(q)\,q = \vec{0}$, and
- $\mathcal{B}_2(\|q\|)\mathcal{B}_3(\xi, q)\,q = \vec{0}$.

These facts imply

$$\psi^T \left(\hat{\mathcal{A}}^{-1}(\psi)\right) \psi = \psi^T \begin{bmatrix} \mathcal{A}^{-1}(q) & \frac{1-\alpha(\|q\|)}{\|q\|^2} \mathcal{J}(q) \mathcal{J}(\xi) \\ 0_{3\times 3} & 0_{3\times 3} \end{bmatrix} \psi. \tag{B.7}$$

From which we can see

$$\begin{aligned} \frac{1}{2}\psi^T \left(\hat{\mathcal{A}}^{-1}(\psi) + \hat{\mathcal{A}}^{-T}(\psi)\right) \psi =& \frac{1}{2}\xi^T \left(\mathcal{A}^{-1}(q) + \mathcal{A}^{-T}(q)\right) \xi + \\ & \frac{1-\alpha(\|q\|)}{2\|q\|^2} \left(\xi^T \mathcal{J}(q) \mathcal{J}(\xi) q + q^T \mathcal{J}(\xi) \mathcal{J}(q) \xi\right) + q^T q \\ =& \xi^T \xi + q^T q + \\ & \frac{1-\alpha(\|q\|)}{2\|q\|^2} \left(2\xi^T \mathcal{J}(q)^2 \xi - 2\xi^T \mathcal{J}(q) \mathcal{J}(q) \xi\right) \\ =& \psi^T \psi \end{aligned}$$

B.2 Bounding $\|\hat{\mathcal{A}}^{-1}(\psi)x\|$

In this Section we show there $\exists c \in \mathbb{R}_+$ such that $\forall \psi, x \in \mathbb{R}^6$ for which $\|\psi\| < \pi$ we have $\|\hat{\mathcal{A}}^{-1}(\psi)x\| < c\|x\|$. Specifically, we prove $c = 6 + \frac{5\pi}{2} + \frac{\pi^2}{8}$ satisfies this inequality. Let $\xi,\ q,\ x_1\ x_2 \in \mathbb{R}^3$ such that $\psi = [\xi^T \quad q^T]^T$ and $x = [x_1^T \quad x_2^T]^T$, then

$$\begin{aligned} \|\hat{\mathcal{A}}^{-1}(\psi)x\| \leq& \|\mathcal{A}^{-1}(q)x_1\| + \|\mathcal{A}^{-1}(q)x_2\| \\ & + \| \left(\frac{1}{2}\mathcal{J}(\xi) + \frac{1-\alpha(\|q\|)}{\|q\|^2}\mathcal{B}_4(\xi, q) + \mathcal{B}_2(\|q\|)\mathcal{B}_3(\xi, q)\right) x_2\|. \end{aligned} \tag{B.8}$$

Note that $\|x_1\| \leq \|x\|$, $\|x_2\| \leq \|x\|$, $\|\xi\| \leq \|\psi\| < \pi$, and $\|q\| \leq \|\psi\| < \pi$. Consider

$$\begin{aligned} \|\mathcal{A}^{-1}(q)x_i\| \leq& \|x_i\| + \|\mathcal{J}(q)x_i\| + \| \left(1 - \alpha(\|q\|)\right) \frac{\mathcal{J}(q)^2}{\|q\|^2} x_i\| \\ \leq& \|x_i\| + \|q\|\|x_i\| + |\left(1 - \alpha(\|q\|)\right)| \, \|x_i\|. \end{aligned} \tag{B.9}$$

For q such that $\|q\| < \pi$ consider the value of $|(1-\alpha(\|q\|)|$. Note that for $y = \frac{\pi}{2}$ we know $1 - y\cot(y) = 1$; by l'Hospital's rule we know $\lim_{y\to 0^+} y\cot(y) = \lim_{y\to 0^+} \frac{\cos(y) - y\sin(y)}{\cos(y)} = 1$; and for $y \in \left(0,\ \frac{\pi}{2}\right)$ we know $\frac{d}{dy}\left(1 - y\cot(y)\right) > 0$. These imply $\forall y \in \left[0,\ \frac{\pi}{2}\right) \quad |1 - y\cot(y)| \leq 1$ and therefore $\|\mathcal{A}^{-1}(q)x_i\| < (2+\pi)\|x_i\|$.

A similar analysis can be used to bound other terms in (B.8). Using l'Hospital's rule and differiation it can be shown $\lim_{y\to 0^+} \frac{1-\alpha(y)}{y} = 0$, $\frac{1-\alpha(\pi)}{\pi} = \frac{1}{\pi}$, and the function $\frac{1-\alpha(y)}{y}$ is strictly increasing for $y \in (0, \pi)$; these facts and previous definitions are used to show

$$\begin{aligned}
\|\frac{1-\alpha(\|q\|)}{\|q\|^2}\mathcal{B}_4\left(\xi, q\right)x_2\| =& \|\frac{1-\alpha(\|q\|)}{\|q\|}\mathcal{B}_4\left(\xi, \frac{q}{\|q\|}\right)x_2\| \\
\leq& |\frac{1-\alpha(\|q\|)}{\|q\|}|\ \|\xi\|\|x_2\| \\
<& \|x_2\|.
\end{aligned}$$

Using l'Hospital's rule and differiation it can be shown $\lim_{y\to 0^+} \frac{\alpha(y)-\beta(y)}{2y} = 0$, $\frac{\alpha(\pi)-\beta(\pi)}{2\pi} = \frac{-\pi}{8}$, and the function $\frac{\alpha(y)-\beta(y)}{2y}$ is strictly decreasing for $y \in (0, \pi)$; these facts and previous definitions are used to show

$$\begin{aligned}
\|\mathcal{B}_2(\|q\|)\mathcal{B}_3\left(\xi, q\right)x_2\| =& \|\frac{(1-\alpha(\|q\|)) + \frac{1}{2}(\alpha(\|q\|) - \beta(\|q\|))}{\|q\|}\mathcal{B}_3\left(\xi, \frac{q}{\|q\|}\right)x_2\| \\
\leq& \left(|\frac{1-\alpha(\|q\|)}{\|q\|}| + |\frac{\alpha(\|q\|) - \beta(\|q\|)}{2\|q\|}|\right)\ \|\xi\|\|x_2\| \\
<& \left(1 + \frac{\pi^2}{8}\right)\|x_2\|. \qquad \text{(B.10)}
\end{aligned}$$

Therefore, using the bounds above, from (B.8) we have

$$\begin{aligned}
\|\hat{\mathcal{A}}^{-1}(\psi)x\| <& (2+\pi)\|x_1\| + \frac{1}{2}\|\xi\|\|x_2\| + \|x_2\| + \left(1 + \frac{\pi^2}{8}\right)\|x_2\| + (2+\pi)\|x_2\| \\
<& \left(6 + \frac{5\pi}{2} + \frac{\pi^2}{8}\right)\|x\| \qquad \text{(B.11)}
\end{aligned}$$

Bibliography

[1] "Workhorse navigator datasheet," Teledyne RD Instruments, http://www.rdinstruments.com/navigator.aspx.

[2] N. Aghannan and P. Rouchon, "An intrinsic observer for a class of Lagrangian systems," *IEEE Transactions on Automatic Control*, vol. 48, no. 6, pp. 936–945, 2003.

[3] A. Alessandri, M. Caccia, G. Indiveri, and G. Veruggio, "Application of LS and EKF techniques to the identification of underwater vehicles," in *Proceedings of the IEEE International Conference on Control Applications*, Trieste, Italy, 1998, pp. 1084–1088.

[4] C. H. An, C. G. Atkeson, and J. M. Hollerbach, *Model-Based Control of a Robot Manipulator*. Cambridge, MA, USA: MIT Press, 1988.

[5] G. Antonelli, S. Chiaverini, N. Sarkar, and M. West, "Adaptive control of an autonomous underwater vehicle: Experimental results on ODIN," *IEEE Transactions on Control Systems Technology*, vol. 9, no. 5, pp. 756–65, September 2001.

[6] K. J. Astrom, *Adaptive Control*. Addison-Wesley, 1989.

[7] J. Avila, J. Adamowski, N. Maruyama, F. Takase, and M. Saito, "Modeling and identification of an open-frame underwater vehicle: The yaw motion dynamics," *Journal of Intelligent & Robotic Systems*, vol. 66, no. 1, pp. 37–56, 2012.

[8] R. Bachmayer, L. L. Whitcomb, and M. Grosenbaugh, "An accurate finite-dimensional dynamical model for the unsteady dynamics of marine thrusters," *IEEE Journal of Oceanic Engineering*, vol. 25, no. 1, pp. 146–159, January 2000.

[9] G. Baldwin, R. Mahony, and J. Trumpf, "A nonlinear observer for 6 DOF pose estimation from inertial and bearing measurements," in *Proceedings of the IEEE International Conference on Robotics and Automation*, 2009, pp. 2237–2242.

[10] J. Bellingham, Y. Zhang, J. Kerwin, J. Erikson, B. Hobson, B. Kieft, M. Godin, R. McEwen, T. Hoover, J. Paul, A. Hamilton, J. Franklin, and A. Banka, "Efficient propulsion for the Tethys long-range autonomous underwater vehicle," in *Autonomous Underwater Vehicles (AUV), 2010 IEEE/OES*, sept. 2010, pp. 1 –7.

[11] A. Bowen, M. Jakuba, D. Yoerger, C. German, J. Kinsey, L. Whitcomb, and L. Mayer, "Lightly tethered unmanned underwater vehicle for under-ice exploration," in *2012 IEEE Aerospace Conference*, march 2012, pp. 1 –12.

[12] F. Bullo and A. D. Lewis, *Geometric Control of Mechanical Systems*. New York, NY: Springer, 2004.

[13] F. Bullo and R. M. Murray, "Proportional derivative (PD) control on the Euclidean group," California Institute of Technology, Tech. Rep., 08 1995.

[14] M. Caccia, G. Indiveri, and G. Veruggio, "Modeling and identification of open-frame variable configuration underwater vehicles," *IEEE Journal of Oceanic Engineering*, vol. 25, no. 2, pp. 227–240, April 2000.

[15] N. Chaturvedi, D. Bernstein, J. Ahmed, F. Bacconi, and N. McClamroch, "Globally convergent adaptive tracking of angular velocity and inertia identification for a 3-DOF rigid body," *IEEE Transactions on Control Systems Technology*, vol. 14, no. 5, pp. 841 –853, Sept. 2006.

[16] G. S. Chirikjian and A. B. Kyatkin, *Engineering Applications of Noncommutative Harmonic Analysis*. Boca Raton, FL: CRC Press, 2000.

[17] J. J. Craig, P. Hsu, and S. Sastry, "Adaptive control of mechanical manipulators," *The International Journal of Robotics Research*, vol. 6, no. 2, pp. 16–28, Summer 1987.

[18] T. I. Fossen, *Guidance and Control of Ocean Vehicles*. New York: John Wiley and Sons, 1994.

[19] T. Fossen and S. Sagatun, "Adaptive control of nonlinear underwater robotic systems," in *Proceedings of the IEEE International Conference on Robotics and Automation*, apr 1991, pp. 1687 –1694 vol.2.

[20] E. Freund, "Fast nonlinear control with arbitrary pole placement for industrial robots and manipulators," *The International Journal of Robotics Research*, vol. 1, no. 1, pp. 65–78, 1983.

[21] A. Graham, *Kronecker Products and Matrix Calculus With Applications*. New York: Halsted Press, John Wiley and Sons, 1981.

[22] A. J. Healey, S. M. Rock, S. Cody, D. Miles, and J. P. Brown, "Toward an improved understanding of thruster dyamics for underwater vehicles," *IEEE Journal of Oceanic Engineering*, vol. 20, no. 4, pp. 354–61, October 1995.

[23] R. A. Horn and C. R. Johnson, *Matrix Analysis*. Cambridge University Press, 2006.

[24] P. Hsu, M. Bodson, S. Sastry, and B. Paden, "Adaptive indentification and control for manipulators without using joint accelerations," in *Proceedings of the IEEE International Conference on Robotics and Automation*, Raleigh, NC, USA, 1987, pp. 1210–1215.

[25] IXSEA, *PHINS III User Guide*, 5th ed., IXSEA, July 2008.

[26] M. Jakuba, L. Whitcomb, D. Yoerger, and A. Bowen, "Toward under-ice operations with hybrid underwater robotic vehicles," in *Autonomous Underwater Vehicles, 2008. AUV 2008. IEEE/OES*, oct. 2008, pp. 1 –9.

[27] M. Jordan and J. Bustamante, "A speed-gradient adaptive control with state/disturbance observer for autonomous subaquatic vehicles," in *Proceedings of the IEEE Conference on Decision and Control*, Dec. 2006, pp. 2008 –2013.

[28] C. Kaminski, T. Crees, J. Ferguson, A. Forrest, J. Williams, D. Hopkin, and G. Heard, "12 days under ice - an historic AUV deployment in the canadian high arctic," in *Autonomous Underwater Vehicles (AUV), 2010 IEEE/OES*, sept. 2010, pp. 1 –11.

[29] J. Keim, A. Behcet Acikmese, and J. Shields, "Spacecraft inertia estimation via constrained least squares," in *2014 IEEE Aerospace Conference*, 0-0 2006, p. 6 pp.

[30] W. Khalil and E. Dombre, *Modeling, Identification & Control of Robots*. New York, NY: Taylor & Francis, 2002.

[31] W. Khalil, M. Gautier, and P. Lemoine, "Identification of the payload inertial parameters of industrial manipulators," in *Proceedings of the IEEE International Conference on Robotics and Automation*, 2007, pp. 4943–4948.

[32] P. K. Khosla and T. Kanade, "Parameter identification of robot dynamics," in *IEEE Conference on Decision and Control*, vol. 24, dec. 1985, pp. 1754 –1760.

[33] J. Kim and W. K. Chung, "Accurate and practical thruster modeling for underwater vehicles," *Ocean Engineering*, vol. 33, no. 5, pp. 566–586, 2006.

[34] J. Kinsey, D. Smallwood, and L. Whitcomb, "A new hydrodynamics test facility for uuv dynamics and control research," in *Proceedings of MTS/IEEE Oceans*, vol. 1, 2003, pp. 356–361 Vol.1.

[35] D. E. Koditschek, "Application of a new Lyapunov function to global adaptive attitude tracking," in *Proceedings of the IEEE Conference on Decision and Control*, 1988, pp. 63–68.

[36] ——, "Adaptive strategies for the control of natural motion," in *IEEE Proceedings 24th Conference on Decision and Control*, Fort Lauderdale, Dec 1985, pp. 1405–1409.

[37] K.-Y. Lian, L.-S. Wang, and L.-C. Fu, "Globally valid adaptive controllers of mechanical systems," *IEEE Transactions on Automatic Control*, vol. 42, no. 8, pp. 1149 –1154, aug 1997.

[38] F. Lizarralde and J. T. Wen, "Attitude control without angular velocity measurement: a passivity approach," *IEEE Transactions on Automatic Control*, vol. 41, no. 3, pp. 468–472, 1996.

[39] J. Y. S. Luh, M. W. Walker, and R. P. C. Paul, "Resolved acceleration control of mechanical manipulators," *IEEE Transactions on Automatic Control*, vol. AC-25, pp. 468–474, 1980.

[40] D. Maalouf, I. Tamanaja, E. Campos, A. Chemori, V. Creuze, J. Torres, L. Rogelio *et al.*, "From PD to nonlinear adaptive depth-control of a tethered autonomous underwater vehicle," in *IFAC Joint conference 2013*, 2013.

[41] R. Mahony, T. Hamel, and J.-M. Pflimlin, "Complementary filter design on the special orthogonal group SO(3)," in *Proceedings of the 2005 IEEE Conference on Decision and Control and 2005 European Control Conference (2005 CDC-ECC)*, 2005, pp. 1477–1484.

[42] ——, "Nonlinear complementary filters on the special orthogonal group," *IEEE Transactions on Automatic Control*, vol. 53, no. 5, pp. 1203–1218, 2008.

[43] D. H. S. Maithripala, J. M. Berg, and W. P. Dayawansa, "An intrinsic observer for a class of simple mechanical systems on a Lie group," in *Proceedings of the American Control Conference*, vol. 2, 2004, pp. 1546–1551.

[44] S. C. Martin, "Advances in six-degree-of-freedom dynamics and control of underwater vehicles," Ph.D. dissertation, The Johns Hopkins University, Baltimore, MD USA, September 2008.

[45] S. C. Martin and L. L. Whitcomb, "Preliminary experiments in comparative experimental identification of six degree-of-freedom coupled dynamic plant models for underwater robot vehicles," in *Proceedings of the IEEE International Conference on Robotics and Automation*, Karlsruhe, Germany, May 2013.

[46] ——, "Preliminary experiments in fully actuated model based control with six degree-of-freedom coupled dynamical plant models for underwater vehicles," in *Proceedings of the IEEE International Conference on Robotics and Automation*, Karlsruhe, Germany, May 2013.

[47] C. J. McFarland and L. L. Whitcomb, "A new adaptive identifier for second-order rotational plants with applications to underwater vehicles," in *Proceedings of MTS/IEEE Oceans*, Hampton Roads, VA, October 2012, pp. 1–9.

[48] ——, "Comparative experimental evaluation of a new adaptive identifier for underwater vehicles," in *Proceedings of the IEEE International Conference on Robotics and Automation*, Karlsruhe, Germany, May 2013.

[49] ——, "Experimental evaluation of adaptive model-based control for underwater vehicles in the presence of unmodeled actuator dynamics," in *Proceedings of the IEEE International Conference on Robotics and Automation*, May 2014, submitted for review.

[50] R. M. Murray, Z. Li, and S. S. Sastry, *A Mathematical Introduction to Robotic Manipulation*. Boca Raton: CRC Press, 1994.

[51] K. Narendra and A. Annaswamy, *Stable Adaptive Systems*. NY: Prentice-Hall, 1988.

[52] N. Nguyen and A. Ishihara, "Robust adaptive optimal control modification with large adaptive gain," in *American Control Conference, 2009. ACC '09.*, june 2009, pp. 2581 –2586.

[53] G. Niemeyer and J.-J. E. Slotine, "Performance in adaptive manipulator control," *The International Journal of Robotics Research*, vol. 10, no. 2, pp. 149–161, April 1991.

[54] M. C. Norman, M. A. Peck, and D. J. O'Shaughnessy, "In-orbit estimation of inertia and momentum-actuator alignment parameters," in *AAS 11-164, AAS/AIAA Space Flight Mechanics Meeting*, Feb 2011.

[55] F. Park, "The optimal kinematic design of mechanisms," Ph.D. dissertation, Harvard University, Cambridge, MA, 1991.

[56] A. G. Rawlings, *A Short Introduction to the Applications of Quaternions*.

[57] P. Ridao, A. Tiano, A. El-Fakdi, M. Carreras, and A. Zirilli, "On the identification of non-linear models of unmanned underwater vehicles," *Control Engineering Practice*, vol. 12, no. 12, pp. 1483–1499, 2004.

[58] C. Rohrs, L. Valavani, M. Athans, and G. Stein, "Robustness of continuous-time adaptive control algorithms in the presence of unmodeled dynamics," *IEEE Transactions on Automatic Control*, vol. 30, no. 9, pp. 881–889, 1985.

[59] N. Sadegh and R. Horowitz, "Stability and robustness analysis of a class of adaptive controllers for robotic manipulators," *The International Journal of Robotics Research*, vol. 9, no. 3, pp. 74–92, June 1990.

[60] S. Salcudean, "A globally convergent angular velocity observer for rigid body motion," *IEEE Transactions on Automatic Control*, vol. 36, no. 12, pp. 1493–1497, 1991.

[61] S. Sastry and M. Bodson, *Adaptive Control: Stability, Convergence, and Robustness*. Prentice-Hall, 1989.

[62] J.-E. Slotine and M. Di Benedetto, "Hamiltonian adaptive control of spacecraft," *IEEE Transactions on Automatic Control*, vol. 35, no. 7, pp. 848 –852, jul 1990.

[63] J.-J. E. Slotine and W. Li, "On the adaptive control of robot manipulators," *The International Journal of Robotics Research*, vol. 6, no. 3, pp. 49–59, Fall 1987.

[64] D. A. Smallwood and L. L. Whitcomb, "Adaptive identification of dynamically positioned underwater robotic vehicles," *IEEE Transactions on Control Systems Technology*, vol. 11, no. 4, pp. 505–515, 2003.

[65] ——, "Model-based dynamic positioning of underwater robotic vehicles: theory and experiment," *IEEE Journal of Oceanic Engineering*, vol. 29, no. 1, pp. 169–186, 2004.

[66] M. Takegaki and S. Arimoto, "A new feedback method for dynamic control of manipulators," *ASME Journal of Dynamic Systems, Measurement, and Control*, vol. 103, p. 119, 1981.

[67] J. Taylor, *Classical Mechanics*. Univ Science Books, 2005.

[68] J. D. Van Manen and P. Van Ossanen, *Principles of Naval Architecture, Second Revision, Volume II: Resistance, Propulsion, and Vibration*. Jersey City, New Jersey USA: Society of Naval Architects and Marine Engineers, 1988, e. V. Lewis, Editor.

[69] L. L. Whitcomb, A. Rizzi, and D. E. Koditschek, "Comparative experiments with a new adaptive controller for robot arms," *IEEE Transactions on Robotics and Automation*, vol. 9, no. 1, pp. 59–70, February 1993.

[70] D. R. Yoerger, J. G. Cooke, and J. E. Slotine, "The influence of thruster dynamics on underwater vehicle behavior and their incorporation into control system design," *IEEE Journal of Oceanic Engineering*, vol. 15, no. 3, pp. 167–178, June 1990.

[71] D. R. Yoerger and J. E. Slotine, "Adaptive sliding control of an experimental underwater vehicle," in *Proceedings of the IEEE International Conference on Robotics and Automation*, Sacremento, CA, USA, April 1991, pp. 2746–2751.

[72] D. R. Yoerger and J.-J. E. Slotine, "Robust trajectory control of underwater vehicles," *IEEE Journal of Oceanic Engineering*, vol. OE-10, no. 4, pp. 462–70, October 1985.

[73] J. Yuh, "Modeling and control of underwater robotic vehicles," *IEEE Transactions on Systems, Man, and Cybernetics*, vol. 20, no. 6, pp. 1475 –1483, nov/dec 1990.

[74] J. Yuh, J. Nie, and C. S. G. Lee, "Experimental study on adaptive control of underwater robots," in *Proceedings of the IEEE International Conference on Robotics and Automation*, vol. 1, 1999, pp. 393–398 vol.1.

[75] S. Zhao and J. Yuh, "Experimental study on advanced underwater robot control," *IEEE Transactions on Robotics*, vol. 21, no. 4, pp. 695–703, 2005.

Vita

Christopher J. McFarland was born in Tulsa, Oklahoma in 1983. From 2002 to 2007 he participated in the Dual-Degree program between the University of Puget Sound in Tacoma, Washington and Washington University in St. Louis, Missouri. Christopher attended both institutions, receiving both a B. A. in Physics with a minor in Math from the University of Puget Sound and a B. S. in Mechanical Engineering from Washington University in May 2007. In August 2007 he enrolled in the Mechanical Engineering Ph.D. program at Johns Hopkins University.

Christopher has been recognized with several distinctions including Eagle Scout by the Boy Scouts of America in 2000; a Brown Fellowship for Dual-Degree Engineering Students from 2005-2007; NSF Graduate Research Fellowship honorable mention in 2007 and 2008; Johns Hopkins University Mechanical Engineering Department Fellowship 2007-2008; National Defense Science and Engineering Graduate Fellowship 2008-2011; Link Foundation Doctoral Research Fellowship in Ocean Engineering and Instrumentation 2012-2013; and Achievement Rewards for College Scientists Fellowship 2012-2013.